MICROSTRUCTURAL EVOLUTION OF NICKEL DURING SPARK PLASMA SINTERING

by

Matthew Thomas Luke

A thesis

submitted in partial fulfillment

of the requirements of the degree of

Master of Science in Materials Science and Engineering

Boise State University

May 2010

BOISE STATE UNIVERSITY GRADUATE COLLEGE

DEFENSE COMMITTEE AND FINAL READING APPROVALS

of the thesis submitted by

Matthew Thomas Luke

Thesis Title: Microstructural Evolution of Nickel During Spark Plasma Sintering

Date of Final Oral Examination: 04 December 2009

The following individuals read and discussed the thesis submitted by student Matthew Thomas Luke, and they also evaluated his presentation and response to questions during the final oral examination. They found that the student passed the final oral examination, and that the thesis was satisfactory for a master's degree and ready for any final modifications that they explicitly required.

Megan E. Frary, Ph.D.	Chair, Supervisory Committee
Darryl P. Butt, Ph.D.	Member, Supervisory Committee
Indrajit Charit, Ph.D.	Member, Supervisory Committee

The final reading approval of the thesis was granted by Megan E. Frary, Ph.D., Chair of the Supervisory Committee. The thesis was approved for the Graduate College by John R. Pelton, Ph.D., Dean of the Graduate College.

ACKNOWLEDGEMENTS

This investigation was conducted as part of the requirements for the degree of Master of Science in Materials Science and Engineering from Boise State University. The equipment and materials used in this investigation were provided or made available by the Department of Materials Science and Engineering at Boise State University, by Dr. William Windes and Dr. Mark Carroll at Idaho National Laboratory, and Todd Gansauge at Idaho State University and the Center for Advanced Energy Studies. This research was funded in part by an Idaho National Laboratory LDRD under the supervision of Dr. Megan Frary and Dr. Darryl Butt of Boise State University, and Dr. William Windes and Dr. Mark Carroll of Idaho National Laboratory. Funding was also provided by the Boise State University Graduate College through a fellowship from the Nuclear Regulatory Commission. Dr. Megan Frary is gratefully acknowledged for the guidance and direction she provided to this study. In addition, the support and direction provided by Dr. Darryl Butt of Boise State and Dr. Indrajit Charit of the University of Idaho are sincerely appreciated. Finally, the members of both the Frary and Butt Research Groups deserve acknowledgement for their help in producing and analyzing specimens, and for other support and assistance provided to this project.

ABSTRACT

Spark plasma sintering (SPS) is reported to produce materials with properties superior to those that result from conventional processing techniques. Spark plasma sintering is also reported to process materials at lower temperatures and in a shorter time than other processes, which may facilitate the synthesis of materials that are traditionally difficult to process. While the properties of materials that result from SPS processing have been studied, there is not a thorough understanding of the evolution of the microstructure in response to SPS process parameters. A comparison of the microstructure of nickel produced by SPS at varying ramp rate, temperature, dwell time, and applied pressure, and nickel produced at varying time and temperature by conventional sintering (CS) techniques is made. Material properties that are compared include: density, hardness, porosity, average grain size, and grain boundary character. Evaluations of the activation energy of sintering, plastic flow, and modeling using a hot-press equation of SPS nickel are also performed to elucidate the mechanism of sintering. The results from this study are expected to give insight into more complex material systems processed with SPS.

The specimens processed by SPS reach higher density at lower temperatures than those processed by CS techniques. The hardness of SPS nickel is linearly related to the density, consistent with results from foams. The hardness and porosity results also indicate that radial temperature gradients do exist during SPS processing of nickel. The

average grain sizes do not change significantly with SPS process conditions except at high temperatures or for long dwell times. Approximations of the grain growth rate of SPS nickel are higher than for CS nickel. The grain boundary character is stable during both SPS and CS processing, with significant increases in the Σ3 and special fractions only occurring at the longest times and highest temperatures. The activation energy of sintering indicates that SPS nickel densifies by diffusional processes. A hot-press model is also used to help identify the sintering mechanism, but the model is insufficient to explain the SPS process. The microstructural evolution of nickel is different during processing with SPS and with CS techniques.

TABLE OF CONTENTS

LIST OF TABLES

LIST OF FIGURES

LIST OF ABBREVIATIONS

CS - Conventional sintering

CSL - Coincident -site lattice

DC - Direct current

EBSD - Electron backscatter diffraction

FAST - Field-assisted sintering technique

P^2C - Plasma pressure compaction

PAS - Plasma-assisted sintering

PECS - Pulsed electric current sintering

SEM - Scanning electron microscope

SPS - Spark plasma sintering

LIST OF SYMBOLS

A	-	Materials constant for activation energy calculation
b	-	Burgers vector
B	-	Collection of material constants for initial-stage sintering
B_1	-	Thermally activated parameter for initial-stage sintering
B_2	-	Thermally activated parameter for intermediate-stage sintering
C	-	Material constant for power-law creep deformation
γ	-	Surface energy
d	-	Particle diameter
d_m	-	Mean diagonal length of Vickers indentation
d_p	-	Pore radius
D_o	-	Diffusivity pre-exponential
D	-	Diffusivity
D_b	-	Grain boundary diffusion coefficient
D_s	-	Surface diffusion coefficient
D_v	-	Volume diffusion coefficient
δ	-	Grain boundary width
F	-	Force
g	-	Grain growth exponent
G_o	-	Initial grain size

G - Grain size

H - Collection of material constants related to the hot-pressing mechanism

k - Boltzmann's constant

K_o - Rate constant for activation energy calculation

K - Thermally activated parameter for grain growth

L_o - Initial distance between particle centers

ΔL - Change in distance between particle centers

m - Material constant exponent for initial-stage sintering

M - Molecular weight

μ - Shear modulus

n - Material constant exponent for initial-stage sintering

η - Viscosity

P - Vapor pressure

P_A - Applied pressure

P_E - Effective pressure

P_g - Gas pressure in a pore

q - Pressure exponent

Q - Activation energy

R - Gas constant

R_1, R_2 - Radii of curvature

ρ - Theoretical density

ρ_g - Green-body density

ρ_i - Density at the beginning of intermediate-stage sintering

ρ_s - Fractional density

σ - Stress, specifically the sintering stress associated with a curved surface

σ_Y - Yield strength

Σ - Coincident-site lattice index

t - Time

t_i - Time at the onset of intermediate-stage sintering

T - Temperature

u - Geometric term for densification during intermediate-stage sintering

ϕ - Stress intensification factor

X - Neck diameter

Ω - Atomic volume

CHAPTER 1: INTRODUCTION

1.1: Motivation for Research

The properties, processing, and microstructure of any material are interrelated [1]. Different process techniques produce different microstructures, and certain microstructures may result in superior material properties [1]. A study of spark plasma sintering (SPS), a process which has been reported to improve the properties of a wide variety of materials [2-40], is presented here. This study was performed with commercially-pure nickel powder sintered both using conventional sintering (CS) and SPS, under a variety of conditions, to determine how the microstructure evolved as a function of process conditions. This study also provided some insight into the mechanisms that are active during SPS and some understanding of the kinetics of sintering and grain growth during SPS. Microstructural characterization using electron backscatter diffraction (EBSD) allowed for observation of grain growth inside polycrystalline nickel powder, as well as growth and densification of the powder particles. This study on a simple, pure metal system aids understanding of the microstructural evolution, sintering mechanisms, and kinetics of more complex material systems.

Nickel was selected due to its well characterized behavior during sintering and annealing [41-55]. The use of a straightforward, well understood system allows for comparisons to be easily made between properties that result from conditions unique to

SPS and those that result from conventional processing. Under CS conditions, nickel will undergo surface diffusion at temperatures below 600°C, and will not densify at temperatures below that point [41, 42, 55]. Above that temperature, densification will progress due to volume diffusion [41, 42, 55]. Grain growth during sintering of nickel has a $t^{1/3}$ dependence [56, 57], and during annealing has a $t^{1/2}$ dependence [45, 47, 49, 50, 53, 54], where *t* is time. Another important microstructural characteristic is the grain boundary character distribution. The grain boundary energy in nickel can be significantly reduced by the formation of twin boundaries, and high fractions of twin boundaries are found in annealed nickel [49, 54, 58]. The twin boundary fraction in sintered nickel is strongly temperature dependent and increases with increasing temperature [43]. Results from this comparative study of CS and SPS nickel are expected to correlate with nickel-based alloys and other systems processed with SPS.

1.2: Research Objectives

The primary objective of this research was to characterize the effects of SPS process conditions on the microstructure of nickel in comparison to conventional sintering of nickel. A comparison of the process techniques gives insight into sintering mechanisms that are unique to the SPS process and the kinetics of sintering and grain growth during SPS. An understanding of the microstructural evolution during SPS is essential for understanding the processing-properties relationship that is extensively discussed in SPS literature.

Processing with SPS allows for different temperatures, heating rates, dwell times, and pressures. Nickel was processed with SPS equipment owned by Boise State

University and located at the Center for Advanced Energy Studies at a variety of all these conditions to determine how each individually affects the microstructure. For comparison, nickel was also conventionally sintered at different temperatures and for different dwell times. Characterization of the density, hardness, and porosity was performed to understand the densification and to give an insight into the mechanical properties. Microstructural characterization was performed using scanning electron microscopy (SEM) and analysis using EBSD. This analysis resulted in the effect of SPS and CS process conditions on grain size and grain boundary character. Characterization using EBSD was central to this study as it allowed for a thorough analysis of the microstructure and how it changed according to process conditions which, in turn, shows how the properties of materials processed by SPS are affected.

CHAPTER 2: BACKGROUND INFORMATION

2.1: Overview of Sintering Processes

2.1.1: Traditional Sintering

Sintering is the consolidation of powders into solid parts [56, 57, 59]. Sintering techniques have been used for thousands of years to make pottery, jewelry, bricks, and other materials [56, 57, 59]. Little consideration was given to the science of sintering until the early 20th century, beginning with the work of Coolidge on tungsten powders for light bulb filaments [59]. Sintering has since been extensively studied and the theoretical models first developed by Kuczynski, Coble, Kingery, Berg, Johnson, and others provide the basis for sintering theory today [60-66]. Several textbooks are available on the theory and science of sintering [56, 57, 67]. The summary provided in this section is taken from German [56, 57].

Sintering is the bonding of particles by diffusion of atoms to reduce surface area. Conventional sintering is typically performed by pressing powders into a compact and heating the compact to a point, below the melting temperature, where the atoms can diffuse. Diffusion is a thermally activated process, requiring a minimum energy to begin. The activation energy for thermal diffusion is described by the Arrhenius relation:

$$D = D_o \exp\left(-\frac{Q}{RT}\right) \qquad (2.1)$$

where D is diffusivity, D_o is the diffusivity pre-exponential, Q is the activation energy for self-diffusion (approximately equal to 0.145 T_{melt} in Kelvin), R is the gas constant and T

is the temperature. As atoms diffuse, some will move into positions that reduce the total surface area and thus reduce the surface energy. The driving force for atoms to move to positions that reduce the surface energy is associated with the stress at the particle surface. The Laplace equation gives the stress of a curved surface, σ, by:

$$\sigma = \gamma\left(\frac{1}{R_1} + \frac{1}{R_2}\right) \qquad (2.2)$$

where γ is the surface energy, and R_1 and R_2 are the radii of curvature of the surface. Particles with small radii of curvature have high associated stresses. Also, the surface energy of a particle is inversely related to its diameter; smaller particles have higher surface energies per unit volume. Thus, when two particles are touching, there is a driving force to reduce the stress and surface area by increasing the radii of curvature at the contact point. As atoms diffuse to the contact region, a neck, or the initial bond, forms between the particles. After initial neck formation, atoms continue to diffuse to the neck region, which increases the radius of curvature and, in turn, slows the sintering process as the driving force is reduced. In the intermediate sintering stage, pore volume is decreased and the idealized pore structure changes from being irregular and angular to an interconnected cylindrical structure along the grain boundaries. As pore volume continues to decrease, the structure becomes unstable (the breakdown is where the ratio of pore length to radius becomes larger than 2π) and at the final stage of sintering, the pore structure collapses into isolated spherical isolated pores. The isolated pores do not inhibit grain growth as much as the interconnected structure does which leads to increased grain growth during late stage sintering. Grain growth and isolated pores at late stage sintering can slow the rate of densification, especially if the pores contain trapped gas.

The sintering process can include plastic deformation or particle rearrangement, but at all stages involves the diffusion of atoms. Generally, diffusion processes fall into two main categories: surface and bulk transport, illustrated in Figure 2.1. Surface transport (Figure 2.1a) involves the rearrangement of particles to form a neck without any shrinkage or densification. Surfaces of crystals consist of various types of defects, such as surface vacancies, adsorbed atoms, ledges and kinks, many of which can participate in diffusion. Surface diffusion involves the breaking away of an atom, usually from the site of a surface defect, random motion of that atom across the surface, and finally reattachment at a different site, possibly another defect. In neck formation in surface diffusion, atoms fill sites at the interface between particles that reduce the curvature and thereby reduce the surface energy. Surface diffusion is the dominating mechanism at low temperatures in most metals, including nickel [41, 56]; metals with high vapor pressure also undergo evaporation-condensation surface transport. Evaporation occurs on a particle surface and atoms move across the pore space to be deposited on a different surface.

Bulk transport processes involve the movement of mass from the interior of the particle to the neck region and cause shrinkage (Figure 2.1b). Bulk transport includes volume diffusion, grain boundary diffusion, plastic flow, and viscous flow. Plastic flow is the glide and climb of dislocations due to stress at the neck and absorption of vacancies during pore size reduction. Plastic flow is important during the heating stage (especially for compacted powders with high dislocation density) but decreases as dislocations are annealed out of the particles. Viscous flow, where materials with decreased viscosity at elevated temperatures flow under applied stress, is typically more important during liquid

phase sintering, or when liquid is present at grain boundaries. Grain boundary diffusion is important in most polycrystalline metals as it is more energetically favorable than diffusion through the lattice.

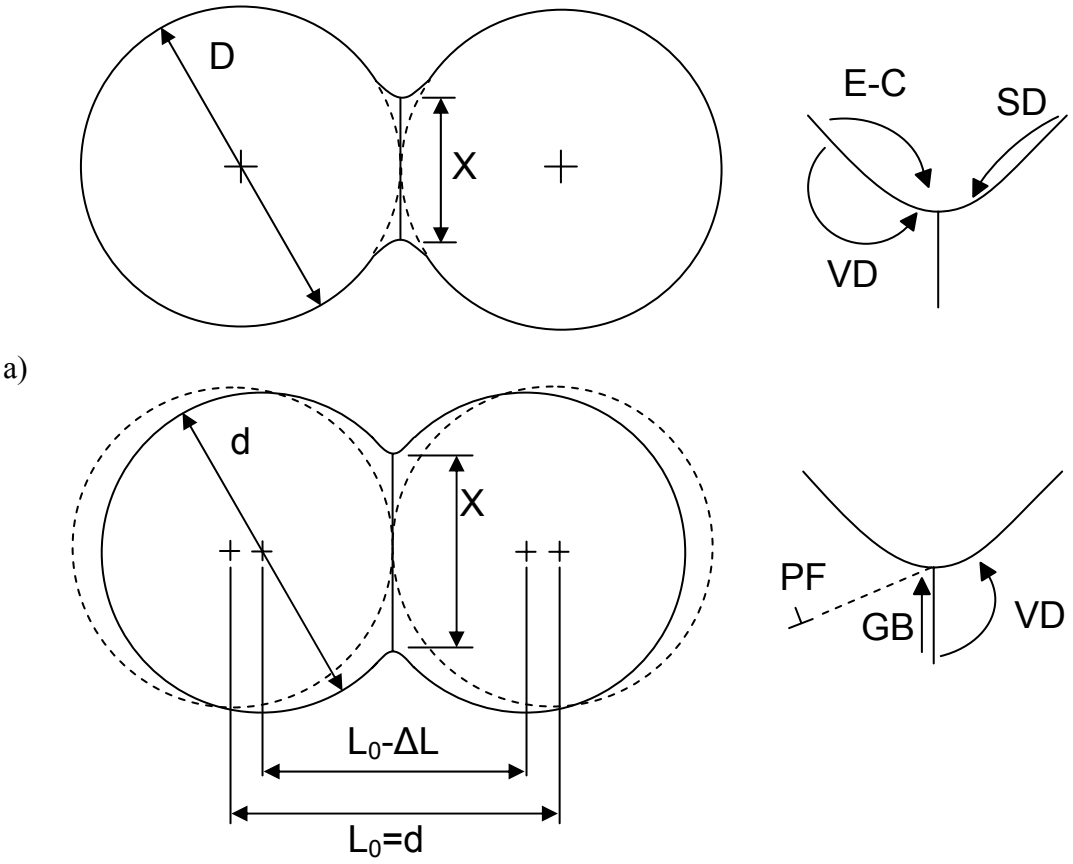

Figure 2.1. Idealized two sphere sintering model. The surface transport mechanisms (a), evaporation-condensation (E-C), volume diffusion of atoms from the surface to the surface (VD), and surface diffusion (SD) lead to neck formation, but not to a change in the particle centers. The bulk transport mechanisms (b), plastic flow (PF), grain boundary diffusion (GB), and volume diffusion (VD) are responsible for changes in the particle centers (densification). Adapted from German [56, 57].

During initial stage sintering, two processes occur: neck growth and shrinkage. The equation for isothermal neck growth in initial stage sintering is given by:

$$\left(\frac{X}{d}\right)^n = \frac{Bt}{d^m} \qquad (2.3)$$

where X is the neck diameter, d is the particle diameter, t is time, and B, m, and n are a collection of material and geometric constants. The values of B, m, and n depend on the sintering mechanism and are given in Table 2.1.

Table 2.1: Initial stage sintering mechanisms for Equation 2.3.

Mechanism	n	m	B
Viscous flow	2	1	$3\gamma/\eta$
Plastic flow	2	1	$9\pi\gamma b D_v/kT$
Evaporation-condensation	3	2	$(3P\gamma/\rho^2)(\pi/2)^{1/2}(M/kT)^{3/2}$
Volume diffusion	5	3	$80D_v\gamma\Omega/kT$
Grain boundary diffusion	6	4	$20\delta D_b\gamma\Omega/kT$
Surface diffusion	7	4	$56D_s\gamma\Omega^{4/3}/kT$

γ = surface energy
η = viscosity
b = Burgers vector
k = Boltxzmann's constant
T = absolute temperature
ρ = theoretical density
δ = grain boundary width
D_v = volume diffusivity
D_s = surface diffusivity
D_b = grain boundary diffusivity
P = vapor pressure
M = molecular weight
Ω = atomic volume

Several characteristics of sintering can be inferred from the equations in Table 2.3. For example, there is a strong dependence on inverse particle size, meaning that smaller particles sinter more rapidly. Also, surface diffusion and grain boundary diffusion are more important for smaller particles. There is an exponential dependence on temperature which can be inferred from the neck growth equations. The equations

contain diffusivity terms, and diffusivity was defined in Equation 2.1 to be exponentially dependent on temperature. Therefore small changes in temperature are expected to have large effects. Neck growth is proportional to time, and therefore time is expected to have a smaller contribution than does temperature.

The equation for shrinkage during sintering is given by:

$$\left(\frac{\Delta L}{L_o}\right)^{\frac{n}{2}} = \frac{B_1 t}{2^n d^m} \tag{2.4}$$

where ΔL is the change in the distance between particle centers (see Figure 2.1b), L_o is the starting distance between particle centers (the diameter of one particle), and B_1 is exponentially dependent on temperature and defined by:

$$B_1 = B \exp\left(\frac{-Q}{RT}\right) \tag{2.5}$$

where B is the same as defined in Equation 2.3 and Table 2.1. The shrinkage equation is only valid for bulk transport mechanisms and does not require measuring the neck diameters between particles.

The densification during initial stage sintering is small. Intermediate stage sintering is the most important for densification and for determining the final properties of the specimen, but is the most complex and least understood. During intermediate stage sintering, pore rounding, densification, and grain growth occur simultaneously. There are no good fundamental models for intermediate stage sintering, but empirical models have been developed. Densification during intermediate stage sintering is given by:

$$\rho_S = \rho_i + B_2 \ln\left(\frac{t}{t_i}\right) \tag{2.6}$$

where ρ_s is the fractional density, ρ_i is the density at the beginning of the intermediate stage, B_2 is a thermally activated parameter similar to B_1 which was given by Equation 2.5, and t_i is the time corresponding to the onset of intermediate stage sintering. Curvature gradients at the pores have been largely eliminated at this stage and the driving force becomes the elimination of remaining surface energy. The bulk diffusion mechanisms reduce pore volume by the creation of a vacancy at the pore surface and the diffusion of the vacancy to a grain boundary. The rate of densification by volume diffusion, $d\rho_s/dt$, is given by:

$$\frac{d\rho_S}{dt} = \frac{u\gamma\Omega D_V}{kTG^3} \tag{2.7}$$

where u is a geometric term (usually near 5) and G is the grain size. Grain boundaries have a strong effect on sintering; limited grain growth promotes densification. The mean grain size is a function of time:

$$G^g = G_o^g + Kt \tag{2.8}$$

where G_o is the initial grain size and K is a thermally activated parameter, similar to B_1 and B_2, and g is the grain growth exponent. Grain growth increases as the pores either coalesce or as porosity is eliminated.

As stated previously, the pore structure collapses from an interconnected network into a set of isolated pores during final stage sintering. Grain growth becomes more active as the isolated pores have less of a pinning effect. Normally pores begin to close at 15% porosity and are all closed at 5% porosity. Final stage sintering is a slow process where grain growth and densification are in competition. The densification during final stage sintering is given by:

$$\frac{d\rho_S}{dt} = \frac{12 D_V \Omega}{kTG^3}\left(\frac{4\gamma}{d_P} - P_g\right) \tag{2.9}$$

where d_P is the pore radius and P_g is the gas pressure in the pore. Like the intermediate sintering equation, densification is inversely proportional to the cube of grain size. Densification occurs only as the pore volume decreases by the diffusion of vacancies, by bulk transport mechanisms, from the pore surface to grain boundaries. Densification is slowed and can be stopped by trapped gas in the pores when the surface energy of the pore is equal to the gas pressure:

$$4\gamma = P_g d_P \tag{2.10}$$

Differences in pore curvature can cause smaller pores to be absorbed into larger pores in order to reduce the surface energy. Usually, achieving full density requires a vacuum or another sintering technique such as hot-pressing.

2.1.2: Pressure-Assisted Sintering

The application of stress during sintering may be required in order to attain desirable densification and to eliminate porosity. An applied pressure will supplement the inherent sintering stress and increase the densification process, especially at high temperatures where the yield strength is decreased. Temperature plays the same role in pressure-assisted sintering as in traditional sintering, by increasing mass motion as well as decreasing the yield strength of the material which allows for increased response to applied stress. Pressure-assisted sintering techniques include hot pressing, hot isostatic pressing, forging, spark plasma sintering and others. Each technique applies pressure in a different manner creating stress states specific to the technique used. Unless otherwise

stated, references from this section come from textbooks by German and Rahaman [56, 57, 67].

Pressure-assisted sintering techniques have several advantages over conventional sintering, such as an increased densification rate, reduced porosity, and increased uniformity of microstructure when performed properly. Pressure-assisted sintering can also be used to produce materials that cannot be processed by pressure-less techniques. However, pressure-assisted sintering techniques also have inherent drawbacks. Contamination at particle contacts is very common with pressure-assisted sintering techniques, which typically require less time than traditional sintering. Surface oxide films may remain in the compact and decorate the grain boundaries, decreasing the fracture resistance where the time required to process by traditional sintering may be sufficient to break down the oxide layer. The application of pressure also commonly results in distortions of the powder compact and anisotropic shrinkages. Grain growth is also accelerated by high pressures as applied pressure increases the packing coordination number, bringing particles into close contact sooner in the sintering process. Thus, grain growth begins sooner than in traditional sintering where grain growth is slowed by porosity. Pressure-assisted sintering is typically performed at lower temperature than conventional sintering to avoid excessive grain growth.

Accelerated grain growth in pressure-assisted sintering promotes earlier pore closure than with traditional sintering. The pores become stable once they reach equilibrium between grain boundary energy and surface energy. If the grains are smaller than the pores, a decrease in pore volume would decrease the surface energy in exchange for a large increase in grain boundary energy. Closing pores around larger grains does

not significantly affect the grain boundary energy. Pores in a powder compact can also be forced close by pressure, but a subsequent heat treatment may induce porosity again.

Depending on the microstructure, the effective pressure can be much higher than the applied pressure during pressure-assisted sintering. The applied load is not distributed evenly across the entire area of the rams or punches, but rather across the particle contact surfaces. Since stress is force over area, smaller contact points have greater stresses, and as the contact points grow, the stress diminishes. Stress amplification at particle contacts enhances sintering by even low applied stresses. Since applied stress is generally constant, the effective pressure, or pressure at the contacts, decreases with densification. The applied pressure is generally constant, but the effective pressure changes as the particle contacts change size, and it is the effective pressure that affects the densification rate. Various models for the relationship between applied and effective stress have been proposed, all of which are functions of the fractional density. The models also assume the stress is uniform for all contacts and is uniform across each contact, neither of which is true in reality. The high pressure at particle contacts leads to localized deformation which improves the bond quality between particles. Also, high strain rate processes (e.g., forging and extrusion) produce stronger materials whereas low strain rate processes that work by diffusional creep (e.g., hot isostatic pressing) result in annealed microstructures that are dense, but have decreased strength. In the extreme, the capillary stress between particles (sintering stress) will exceed the yield stress and cause rapid densification.

At all stages of densification, the densification rate is dependent on stress and grain size. The exact dependence is determined by the controlling mechanism. Three

primary deformation mechanisms exist during pressure-assisted sintering: viscous flow, plastic flow, and creep. Viscous flow occurs in materials where a glass or liquid is the deformable phase and is not expected to be applicable in this study.

Plastic flow is the deformation of the compact at stresses above the yield strength of the material. Yield strength decreases with increased temperature and, at extreme pressures, it is possible to achieve 100% density at high temperatures. Typically, stress concentration at particle contacts initially exceeds the yield strength and deformation occurs by plastic flow. The final density attainable by plastic flow is estimated by:

$$\rho_s = \left[\frac{(1-\rho_g)P_A}{1.3\sigma_Y} + \rho_g{}^3 \right]^{1/3} \tag{2.11}$$

where ρ_g is the green density, P_A is the applied pressure, and σ_Y is the yield strength. This equation is valid for final densities below 90% and at higher final densities, the density attainable by plastic flow is given by:

$$\rho_s = 1 - \exp\left(\frac{P_A}{\sigma_Y}\right) \tag{2.12}$$

As particle contacts grow, the effective pressure decreases, but deformation will continue by diffusional flow. Initial densification is due to particle rearrangement from the shear stress and plastic flow. Grain boundary and volume diffusion become dominant as densification continues. Diffusion controlled processes have a small dependence on stress and strong dependence on temperature. The opposite is true for dislocation controlled densification.

Diffusional flow and stress combine to form a creep densification process. Depending on the temperature, pressure, and grain size, creep occurs by different diffusional processes. Nabarro-Herring creep (volume diffusion controlled creep) occurs

by vacancy diffusion in response to the stress gradient between grain boundaries in tension and those in compression. The shrinkage rate for volume diffusion controlled creep is given by:

$$\frac{d(\Delta L / L_0)}{dt} = \frac{13.3 D_V \Omega P_E}{kTG^2} \tag{2.13}$$

where $\Delta L/L_0$ is the linear shrinkage, D_V is the volume diffusion coefficient, Ω is the atomic volume, and P_E is the effective pressure. Coble creep is accommodated by diffusion along grain boundaries. The shrinkage rate depends on atom removal from the grain boundary and deposition at the neck. The Coble creep shrinkage rate is estimated by:

$$\frac{d(\Delta L / L_0)}{dt} = \frac{47.5 \delta D_B \Omega P_E}{kTG^2} \tag{2.14}$$

where D_B is the grain boundary diffusion coefficient and δ is the grain boundary width. Smaller particles increase the number of grain boundaries for diffusion and promote densification. The third creep model, power law creep, occurs at both high temperature and pressure, and depends on the rate of dislocation climb. The empirical equation for shrinkage rate for power law creep is given by:

$$\frac{d(\Delta L / L_0)}{dt} = \frac{Cb\mu D_V}{kT}\left(\frac{P_E}{\mu}\right)^q \tag{2.15}$$

where C is a material constant, b is the Burgers vector, q is the pressure exponent, and μ is the shear modulus. Each of the creep modes is benefitted by small grain size.

The pressure-assisted technique that is most similar to spark plasma sintering is hot-pressing. In hot-pressing and spark plasma sintering, the applied load is uniaxial, but radial stresses also result from the force against the die wall. The radial stress is a

function of the axial stress and the ratio of the two is nearly constant. The radial and axial pressure differential creates a shear effect that improves bonding, the collapse of large flaws, and can disrupt the surface contamination of powders [2, 56, 57, 68]. In hot pressing, graphite die are typically used, which can contaminate the powder compact. The initial densification during hot pressing occurs by particle rearrangement and plastic flow at the particle contacts. As the particle contacts grow, thus decreasing the effective stress to the point where it falls below the yield strength, densification depends on grain boundary and volume diffusion. A generalized equation for densification during hot-pressing is given by:

$$\frac{1}{\rho}\frac{d\rho_s}{dt} = \frac{HD\phi^q}{G^g kT} P_A{}^q \qquad (2.16)$$

where H is a collection of material constants and parameters related to the deformation mechanism, D is the diffusivity coefficient, ϕ is the stress intensification factor, G is the grain size, k is Boltzmann's constant, T is temperature, P_A is the applied pressure, and the pressure exponent q and grain size exponent g are determined by the densification mechanism. Determining the exponents can give insight into the mechanism of hot pressing. The values of the exponents q and g are given in Table 2.2.

Table 2.2. Values of the exponents q and g for equation 2.16.

Mechanism	Grain Size Exponent g	Pressure Exponent q
Volume Diffusion	2	1
Grain Boundary Diffusior	3	1
Plastic Deformation	0	$\geq$3
Viscous Flow	0	1

2.1.3: Spark Plasma Sintering

Spark plasma sintering (SPS) is a rapid, commercial sintering process developed over the past several decades [15]. As early as 1933, patents were issued for machines that heated and sintered powders by passing electric current through them [69-71]. In 1967 in Japan, Inoue patented a machine for rapidly sintering powders by a spark discharge between the particles [72]. The short processing time interested Lockheed Missile and Space Company who licensed and then acquired the "spark sintering" technology to produce beryllium parts for Poseidon missiles [4]. Work in Japan and America continued through the 1970s and commercial machines ultimately became available under a variety of names [9, 28, 73]. Several alternative terms have been used to describe spark plasma sintering including plasma pressure compaction (P^2C) [35] and plasma-assisted sintering (PAS) [25]. The use of the word plasma implies spark generation (plasma) between particles, while other names like field assisted sintering technique (FAST) [2] and pulsed electric current sintering (PECS) [34] pointedly avoid the words spark and plasma. Despite the disagreement on the creation of a spark or plasma [74], SPS remains one of the most common names and is also part of the model name of the machine used in this study. The name SPS will be used in this thesis.

Spark plasma sintering uses high amperage, low voltage, pulsed DC current and uniaxial pressure to consolidate powders [15, 75]. A schematic of the SPS process is given in Figure 2.2. Processing is performed in a vacuum chamber with controllable atmosphere. During processing, the chamber is usually at negative pressure. Powder is held in a conductive die (usually high strength graphite) between two punches. The die

and punches are placed between the rams which must maintain a minimum pressure for good electrical contact. The rams also act as electrodes for the current.

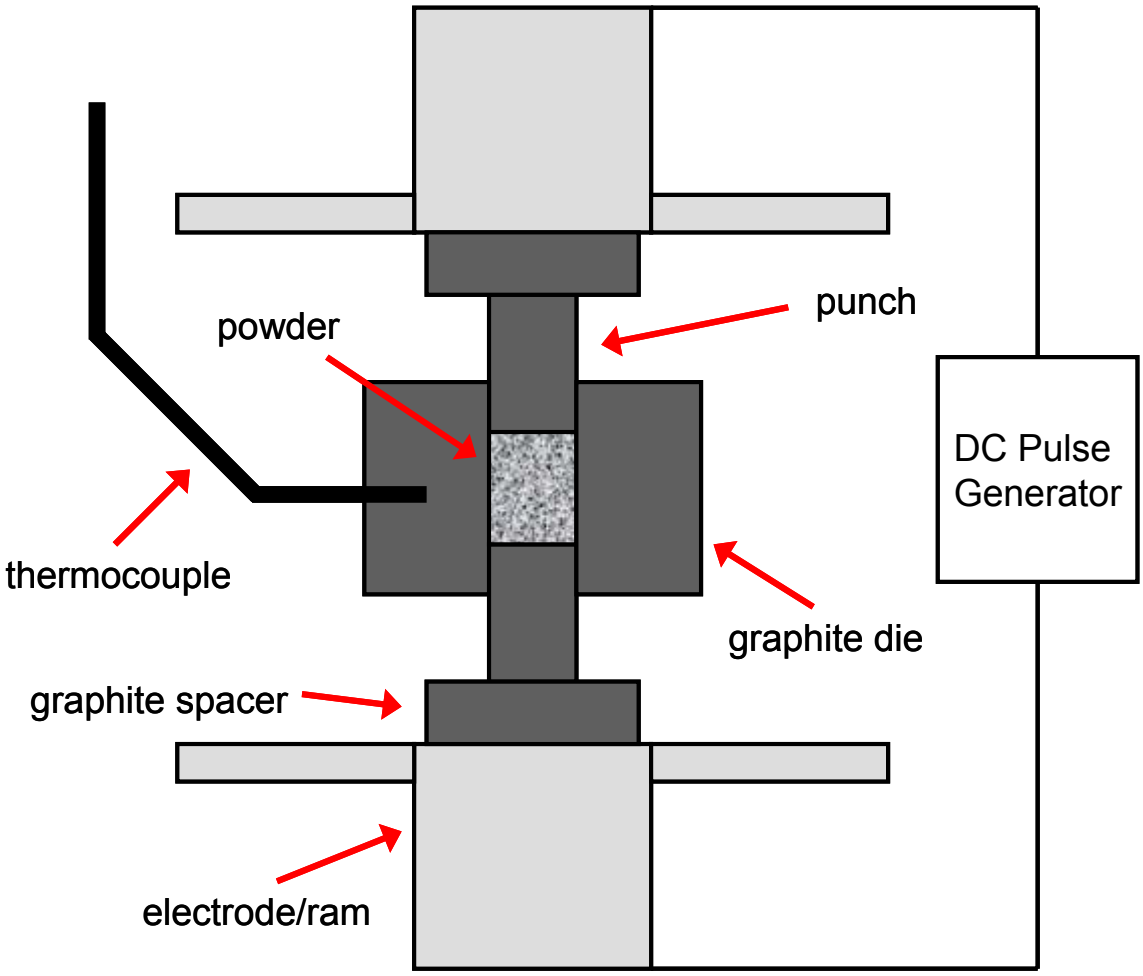

Figure 2.2 Schematic of the SPS process. Powder is held in a conductive die, and heated directly using pulsed DC current in the presence of an electric field and under applied pressure. Temperature is measured at the die wall by a thermocouple or by optical pyrometry.

The sample is heated by a pulsed DC current which passes through the electrodes and die in the presence of a low-voltage electric field. Heat is produced from the dissipation of energy by the punches, die, and powder. This is known as resistive or Joule heating [15, 75]. However, voltage and current cannot be controlled directly. Instead, a temperature profile is programmed by the user and the current is adjusted by the SPS unit accordingly. Temperature is measured either by means of a thermocouple inserted into the die wall or by an optical pyrometer focused on a blackbody cavity in the die wall.

During sintering, the current is passed from the electrodes into the punches which are in contact with both the powder and the die. From there, the current pathway is different for non-conductive powders than for conductive powders [30, 76-80]. For non-conductive powder, the current must pass through the die and heat the powder indirectly, while for conductive powder, the current can pass through the powder and heat it directly [30, 76-80]. If the current pathway is isolated by coating the die and punch walls with boron nitride, conductive powders will sinter but non-conductive powders will not as no sufficiently conductive pathway exists for the current to create heat and sinter the powder [77]. Current flow through the sample is dependent on the conductivity of the powder as well as the sample diameter [30, 76, 78, 79]. All of the current can flow through conductive samples with large diameter, but for smaller samples some of the current will flow through the die, regardless of sample conductivity [76].

The different current pathways for conductive and non-conductive powders lead to different temperature distributions in the samples [76, 78, 80]. A combination of current flow through the sample and radiative heat loss on the die wall gives rise to a

radial temperature distribution in conductive samples [21, 76, 78, 80, 81]. Non-conductive samples have a more uniform temperature distribution; the current passes around the sample and the powder is more evenly heated from the die [21, 76, 78, 80, 81]. Temperature gradients can lead to sample inhomogeneity [76, 79]. For example, zirconia processed with SPS showed a color gradient from oxygen non-stoichiometry [76], and ZrO_2-TiN composites had higher hardness at the center of the sample than at the edge due to increased porosity at the edge [79].

The accuracy of the temperature measurements made on the outside of the die depends on several factors. Generally, the die wall temperature, which is used to control the electrical current, is much lower than the actual sample temperature [30, 76, 78-80, 82, 83]. The difference between the sample temperature and die temperature increases with increasing temperature [76, 79, 80]. During heating of conductive samples, the die wall temperature lags behind the sample temperature, but for non-conductive samples the opposite is true [81]. During the dwell stage, the sample-die temperature difference is less for samples with high thermal conductivity than for samples with low thermal conductivity [79, 81]. Further, the temperature difference increases with increasing die wall thickness and sample diameter [21, 79]. Insulating the die wall reduces the discrepancy between die and sample temperature, but the most accurate method of measuring the actual sample temperature is to record the temperature of the upper punch, where the current density is the highest and the temperature is closest to that of the sample [21, 76, 79-81].

Despite the inherent difficulty of measuring temperature, SPS has been reported to process materials at lower temperatures, with shorter processing times, and produce

materials with superior properties than those processed with comparable techniques [2-40]. It has been proposed that the actual temperature of the samples in SPS is not different than that required to produce identical results with hot-pressing [82]. However, several studies have shown that local temperature distributions exist within a powder compact and that these distributions give rise to the processing advantages observed in SPS [27, 84, 85]. The resistance is higher at the particle contact points where the cross-sectional area is smaller, and so the energy dissipation, and therefore temperature, is greater at the particle contacts than at the center of the powder particle [27]. During processing, the contact points will have a higher temperature than the bulk material and will allow necks to form much faster than in a system with a homogenous temperature [27, 84, 85]. Song *et al.* and Olevsky *et al.* calculate that the temperature at the particle contacts during initial processing can be high enough to melt or even vaporize the material while the temperature of the entire compact rises only slightly [27, 84, 85].

Many, especially early researchers, attributed advantages of processing with SPS to the creation of a current arc between the powders facilitating neck formation or the formation of a plasma around the powders during processing [2, 28, 34, 68, 72]. For example, aluminum is difficult to sinter by traditional methods due to the coherent oxide layer which forms around the powder [34, 68]. However, aluminum does sinter well with SPS, which researchers have attributed to the presence of plasma which removes, or at least disrupts, the oxide layer and allows diffusion to proceed [34, 68]. While some earlier techniques may have indeed produced sparks due to high potentials, the conductive pathway through the die and low voltages make the formation of a current arc or plasma unlikely [15, 27, 74]. An extensive study which used atomic emission

spectroscopy, direct observation, and high-speed voltage measurements failed to find any evidence of plasma in spark plasma sintering [74]. The authors suggest that the low potentials employed during SPS are insufficient to produce an arc [74].

The increased densification during SPS can include both thermal and electrical contributions [84-88]. In addition to temperature gradients that facilitate diffusion, the high heating rates possible in SPS can bypass the surface diffusion processes which smooth the pore structure and slow grain boundary diffusion [84, 85]. Localized high temperature regions can also increase the rate of power-law creep [84, 85, 89]. According to creep deformation mechanism maps of metals, temperature and pressure conditions during processing with SPS are typically in or near the region of power-law creep [84, 85, 89]. As creep processes are important to densification during hot-pressing, they are expected to be important in SPS as well [84, 85]. However, beyond purely thermal effects, the contributions to densification by electrical conditions inherent to SPS may also be significant [8, 14, 15, 22, 36, 86-88]. Atoms can move in response to an applied electric field and due to an applied current [88, 90]. Unfortunately, as the temperature is a result of the applied current, it is difficult to clearly separate the effects of temperature, current, and electric field [15]. Electron-wind force, the term used to describe the motion of atoms in the direction of applied DC current due to momentum transfer from electrons to atoms [90], is considered to be negligible during SPS [15, 88]. It is theorized that the applied electric field and current increase either the mobility or the concentration of defects at grain boundaries as calculated activation energies do not imply that electromigration—diffusion in response to an electric field—is the dominant mechanism [8, 15, 84, 85, 88]. However, modeling studies have shown that diffusion of

atoms by electromigration can have a significant contribution for systems with little porosity, or for fine powders [88]. The pattern of DC pulses in SPS has not been shown to have any effect on material properties [15, 87].

2.2: Densification and Microstructural Evolution in Pure Metals by SPS

The majority of SPS studies focus on the unique properties that result from complicated material systems when processed by SPS [15, 19]. However, many studies have been performed that investigate densification of pure metals by SPS [3, 7, 9, 12, 13, 23, 27, 31, 37-40, 68, 83, 91-94]. It has been found that temperature contributes more to the final density of metals processed by SPS than any other SPS process parameter [7, 12, 23, 31, 37-40, 83, 93, 94]. In iron, copper, and molybdenum, the density increases linearly with temperature until the density reaches approximately 95% theoretical, at which point the effect of temperature on density is diminished, similar to traditional sintering [7, 23, 31, 37, 40, 94]. Other SPS process parameters do not show as significant of an effect as the temperature [7, 23, 31, 37, 40, 94]. Dwell times of up to 15 min do not significantly increase final density in SPS copper [37, 39]. When density is plotted as a function of time, it increases linearly during the heating phase, and once the peak temperature is reached, the densification rate decreases to an equilibrium rate much smaller than that seen during heating [7, 23, 37]. The effect of pressure on the density of metals during SPS is more significant than time, but less than temperature [23, 37]. The pressure effect on density in molybdenum was only seen up to pressures of 50 MPa, at which point increasing pressure did not increase density [23]. Heating rates of 50 – 150°C/min were not shown to have a significant effect on the density of copper [39].

Many SPS studies have shown that near theoretical density can be achieved in a wide variety of material systems with little or no grain growth [2, 3, 5, 12, 17, 18, 23, 29, 35, 37-40, 82, 93, 94]. Alumina, yttria, and other ceramics have been processed to full density by SPS from nano-sized powders, where the grain size increased by less than a factor of 2, remaining in the nano-scale range [18]. In pure metals, the same trend is seen [3, 12, 23, 35, 38-40, 93, 94]. For example, in SPS processed tantalum, the density increased from 84 to 93% theoretical as the temperature was increased from 1500 to 1700°C, but the average crystallite size did not change [3]. Densification occurs first during SPS of pure metals, and significant grain growth occurs after densification is nearly complete, just as in final stage conventional sintering [39, 94]. Optical micrographs of SPS copper and molybdenum show that with increasing temperature, particles first bond and then consolidate, reducing porosity without significant changes to the grain size [39, 94]. Densities of up to 97% can be achieved in copper without a significant increase in grain size [37, 39]. However, above a certain temperature the grain size will show a sharp increase [3, 37, 39]. The grain size in copper increased from approximately 2.5 to 6.5 μm above 750°C for otherwise identical process parameters [37, 39]. In tantalum, the average crystallite size increased by more than a factor of 4, from 22 to 113 nm, with an increase in temperature of 1700 to 1900°C [3]. In nano-sized copper, grain growth was also found to increase exponentially with increasing temperature [37]. Increasing dwell time and applied pressure also increase the grain size in SPS molybdenum and copper, but, similar to the effect on density, not as significantly as temperature [23, 39]. Limited information is available on the grain orientation that results during SPS, however no preferred orientation has been observed in either

aluminum or tantalum processed by SPS [3, 13], while fiber texture in SPS tantalum is reduced compared to that in hot-pressed tantalum [3].

2.3: Powder Metallurgy Studies of Nickel

Pure nickel was used for this study. A summary on studies of nickel that relate to the experiments performed in this thesis are presented here. Studies on the sintering and deformation of nickel are presented first, followed by grain growth and grain boundary character in nickel, and finally a summary of SPS studies of nickel.

2.3.1: Conventional Nickel Processing

The sintering of nickel has been extensively studied, and Ni was frequently used in early sintering studies to understand sintering in general [42, 44, 48, 51, 65]. Before densification occurs in nickel powders, the NiO layer on the powder surfaces is broken down by thermal dissociation or reduction by a process gas such as hydrogen [12, 41, 95]. After the removal of the NiO layer on the powder surfaces, densification proceeds by diffusion processes [41, 56, 57]. The activation energies for the different diffusion mechanisms in nickel are given in Table 2.3 [41, 42, 55-57]. The identification of the sintering mechansism in nickel has undergone some refinement [51], but current textbooks state that nickel densifies by volume diffusion [41, 56, 57]. Significant densification by volume diffusion begins around 600°C, below which densification does not occur as surface diffusion is dominant [41].

Table 2.3. Reported activation energies for nickel diffusion. References are from German and Ashby [42, 55-57].

	Q (kJ/mol) German	Q (kJ/mol) Ashby
Surface Diffusion	164	199
Grain Boundary Diffusion	108	115
Volume Diffusion	298	271

The densification mechanism during sintering of nickel has been found to change with particle size [12, 51, 95]. As nickel powder decreases from 10 μm down to 0.1 μm, grain boundary and surface diffusion combined become prevalent over volume diffusion [12, 51, 95]. During initial sintering, line defects (e.g., dislocations) promote densification in larger nickel powders [95], but for smaller powders, as much as 80% of initial stage densification may be due to interparticle gliding [12]. Further, the activation energy for sintering of nickel has been shown to change with particle size [96]. The activation energy of sintering for nickel nanopowder was found to be 66.2±3 kJ [96].

In relating the mechanisms of conventional sintering to SPS, a deformation mechanism map may provide insight [88, 89]. Deformation mechanism maps show regions where diffusion, creep, and plastic deformation processes are expected to be dominant as functions of stress and temperature [89]. The mechanism of deformation in nickel also depends on grain size [89, 97], and two deformation mechansism maps for grain sizes found in this study are presented for nickel in Figure 2.3 [89]. For nickel with grains that are 1 mm (larger than presented here), the deformation mechanism map shows a large power law creep area and separate grain boundary and lattice diffusion areas [89]. Decreasing grain size increases the diffusional creep rates at a given stress and

temperature [89, 97]. At grain sizes of 1 μm, diffusional flow, where grain boundary creep is the dominant mechanism, is the primary creep mechanism over nearly the full temperature range used in this study [89].

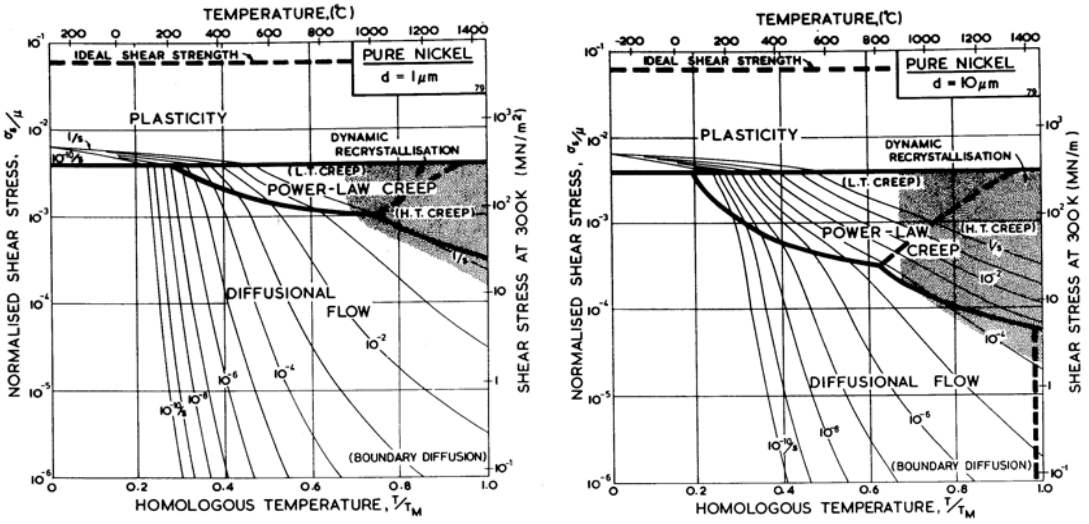

Figure 2.3. Deformation mechanism maps for nickel with grain sizes of 1 and 10 μm [89]. Images taken from the online version of the Frost and Ashby text, available at: http://engineering.dartmouth.edu/defmech/.

2.3.2: SPS of Nickel

Several studies have been performed on nickel powder using SPS processes [12, 19, 83, 91, 92]. The first studies focused on creating powder compacts using electrocompaction [91, 92]. The electrocompaction process is not the same as the current spark plasma sintering process, but rather is accomplished by discharging capacitors across powder compacts at kilovolt potentials in microseconds [91, 92]. Electrocompaction studies on nickel powder found that the energy dissipation at the particle contacts was sufficient to melt and partially vaporize the nickel and potentially

melt the nickel oxide on the powder surface as well [92]. Further, the volumetric expansion of the heated powder would have produced a pressure sufficient to break the oxide layer [92]. Nearly all the oxide was removed from nickel powder processed by electrocompaction, and the remaining oxide was broken down to oxygen and nickel which diffused into the powder matrix [92].

A study was done in 2000 by Kim *et al.* which sintered nickel using the now standard SPS process [83]. Nickel powder was processed in a 30 mm diameter die (15 mm inner diameter) at 40 MPa with no dwell time, a heating rate of 2.4°C/min, and the temperature was measured using a thermocouple on the die surface [83]. A heating rate of 2.4°C/min is much lower than the rate used in this study. At die temperatures of 400, 500, and 800°C, the actual sample temperatures (measured using a second thermocouple and a solid nickel blank) were approximately 440, 560, and 930°C respectively [83]. It was also determined that the actual temperature of a powder compact would be higher than the temperature measured on a solid nickel blank given the same SPS parameters due to differences in conductivity [83]. Nickel processed to 400°C showed almost no particle bonding, but at 500°C necks formed and plastic deformation was observed [83]. At 800°C, the nickel compact reached 98% theoretical density [83]. Nickel processed at varying ramp rates showed that the maximum densification rate is observed at approximately 500°C (extrapolated actual sample temperature) [83]. Dwell times of up to 3 minutes had very little influence on densification [83]. Likewise, varying ramp rates from 0.8 to 3 °C/min had essentially no effect on the final density when processed to 800°C [83].

Another nickel SPS study used nickel nanopowder [12]. Nickel nanopowder begins to densify at around 230°C and the densification is complete at 520°C when using a heating rate of 90°C/min [12]. Grain growth in nickel nanopowder was limited at low temperatures; the initial powder was 50-80 nm, and at process temperatures of 520 and 700°C, the final average grain sizes were 100 and 250 nm [12]. At a process temperature of 1000°C, the grains grew significantly to 2 μm in size [12]. By viewing the fracture surfaces it was observed that small grains can melt with high heating rates [12]. The authors created a densification map for SPS of nickel nanopowder from which it was determined that the sintering mechanism was grain boundary diffusion driven by the high surface energy of the starting powder [12]. With SPS, particle rearrangement can occur due to the applied pressure, and particle bonding (rapid neck formation) may prevent particle gliding [12]. This could lead to low densification rates at the beginning of SPS, but at higher temperatures the diffusion mechanisms become active and local creep at particle contacts becomes more intense [12]. Enhanced mass transport during SPS leads to densification during heating, rather than just during isothermal holding time as is typical of conventional sintering [12].

2.4: Grain Growth and Grain Boundary Character in Nickel

Grain size has well known effects on sintering and deformation mechanisms and kinetics [56, 57, 67, 89, 97]. A grain growth relationship was given in Equation 2.8, where the exponent shows the dependence of grain size on time [56, 57]. During sintering, densification and grain growth occur simultaneously and the grain growth exponent is typically 3 [56, 57]. However, during regular grain growth, the exponent is 2

suggesting that grain growth is more rapid because more of the diffusion contributes to grain growth [45-47, 49, 53, 54, 98]. During annealing of nickel, ideal grain growth kinetics are only achieved in high-purity nickel, as impurities pin the grain boundaries and slow grain growth [47, 49, 53, 54]. Also, in nanocrystalline nickel the grain growth exponents have been found to be 3 or higher, indicating slower grain growth [50]. Grain growth is also a thermally activated process and the kinetics change according to temperature [53, 54, 56, 57]. During annealing of pure nickel, no significant grain growth is observed below 850°C, normal grain growth ($g = 2$) is observed from 850 to 1025°C, and above 1025°C the grain size remains constant [54].

During grain growth in pure nickel, the grain boundary character has been found to change in such a manner as to lower the total grain boundary energy [43, 46, 47, 49, 53, 54, 58]. It is important to first introduce grain boundary classification notation before describing this phenomenon. Grain boundaries are most commonly described by their misorientation [58, 99]. The misorientation between two grains is given by the rotation of one grain about a particular axis to make its lattice match with the second grain [58, 99]. Most misorientations have no particular significance, but certain misorientations have been shown to result in grain boundaries with lower energies or particular properties [58, 99-101]. Many lower energy boundaries are associated with the coincident-site lattice (CSL), where the CSL is used to describe the periodicity of overlapping lattices [58, 99-101]. For particular misorientations, the overlapping lattices result in periodic points where the lattice points of both lattices coincide [58, 99, 101]. CSL boundaries are classified by the sigma (Σ) notation, where Σ is the ratio of the volume of the CSL unit cell to the original unit cell, or the number of coincident sites out of the number of sites

for each repeating CSL unit [58, 99, 101]. The CSL boundaries, taken together, are commonly called the special boundaries [58, 99, 100].

In nickel, the formation of Σ3 (twin) boundaries has been shown to lower the total grain boundary energy, and the fraction of Σ3 boundaries in nickel is typically high [43, 45-47, 49, 53, 54, 58]. The other Σ boundaries in nickel do not have significantly lower grain boundary energy and do not appear with greater frequency that would be expected from a set of random misorientations [58]. Twin formation is usually associated with grain growth, where the twins are formed behind a moving boundary [46]; however, twin formation in nickel may actually be independent of grain growth and the relationship between grain growth and twin formation may be only coincidentally related by temperature [54]. The fraction of Σ3 boundaries formed during annealing of nickel appear to be dependent on temperature and the purity of the nickel [47, 49, 54]. In very high purity nickel (99.999%), the fraction of Σ3 boundaries remained constant during annealing, but in less-pure nickel (99.5%) the fraction of Σ3 boundaries increased with increasing temperature [49]. In a different annealing study, it was found that annealing temperatures below 900°C did not result in a significant increase of Σ3 boundaries, but at 950°C, the Σ3 fraction increased from the initial length fraction of 29% to 40% [54]. Above 950°C, the fraction of Σ3 boundaries decreased slightly from the peak of 40% [54]. The sharp increase of Σ3 boundaries was independent of the grain size [54].

The sintering temperature has also been shown to have a strong effect on the fraction of special boundaries in sintered nickel [43]. Bhattacharjee *et al.* sintered nickel pellets, pressed at 500 MPa, for 1 hour at 900, 1100, and 1300°C in hydrogen at a ramp rate of 5°C/min [43]. Samples were in the furnace during heating and cooling [43]. The

average grain sizes were 6, 11, and 35 μm after sintering at 900, 1100, and 1300°C respectively [43]. The fractions of special boundaries was dependent on the sintering temperature with nearly all the special boundaries being Σ3 boundaries and only small fractions of the other CSL boundaries [43]. The fraction of Σ3 boundaries increased with increasing sintering temperature from about 15% at 900°C, about 25% at 1100°C and about 43% at 1300°C [43]. No significant change was found in the fraction of other CSL boundaries or of low-angle boundaries [43].

CHAPTER 3: EXPERIMENTAL METHODS

The objective of this research was to study the effects of spark plasma sintering (SPS) process parameters on the microstructure of nickel and to learn more about the kinetics of sintering with SPS. Nickel powder was consolidated at a variety of times, temperatures, and pressures using SPS and conventional sintering (CS) techniques. The density and hardness of the resulting specimens were measured and then the microstructure was characterized. The microstructure was analyzed using SEM and EBSD to elucidate how the powder particles consolidate during SPS, to determine grain size, and to determine the grain boundary character distribution. The details of the processing and characterization procedures are presented in this chapter.

3.1: Nickel Powder

The nickel powder (99.9% pure) used was from Vale Inco (Sudbury, Ontario, Canada). It was made by carbonyl thermal reduction, and the reported particle size was 8-15 μm. The size and morphology of the particles were investigated using a Leo 1430VP SEM. The particle size distribution was analyzed using a Horiba LA-950 Laser Scattering Particle Size Distribution Analyzer. The nickel powder was suspended in water, poured into the analyzer, and three measurements were taken while the reservoir was stirred and agitated ultrasonically. Nickel powder was further analyzed using EBSD to determine the grain size and grain boundary character of the powder. The powder was

mounted in acrylic, very briefly ground with 600 and 1200 grit SiC paper, polished using 1 and 0.3 μm alumina slurries for 2 min each, and then polished on a Buehler Vibromet 2 vibratory polisher with 0.05 μm alumina slurry for 12 h. The powder was analyzed using EBSD at a step size of 0.3 μm and a scan area of approximately 75×150 μm.

3.2: Processing with SPS

Spark plasma sintered samples were produced in a Dr. Sinter Lab SPS-515S (SPS Syntex Inc., Kanagawa, Japan) spark plasma sintering machine owned by Boise State University, shown in Figure 3.1. The SPS machine is located at the Center for Advanced Energy Studies in Idaho Falls, ID. The SPS process chamber consists of a water-cooled vacuum chamber, two water-cooled steel ram/electrodes, a quartz view window, a quartz window for the optical pyrometer, and three other ports which can accommodate thermocouples or other measurement tools. For each SPS sample, 5.0 g of nickel powder was measured on an open, top-loading balance inside of a fume hood. The powder was poured into a conductive die made of high strength graphite and held between two graphite punches. Each die was machined from Poco Graphite Inc. AXF-5Q 1-¾ inch diameter (44.5 mm) graphite rod. Each die had an inner diameter of 12 mm, an outer diameter of 44.5 mm, and was 30 mm tall. A 1.6 mm diameter hole was drilled 11 mm into the outside of the die for temperature measurements. Punches were cut to 20 mm lengths from 12 mm diameter rod of the same grade graphite as the die. The die and punches were placed with 13 mm thick graphite spacers between the punches and the electrode plates. The graphite spacers were used to align the die with the view window and cushion the punches. A schematic of the die, punches, and spacers is shown in Figure

3.2. The chamber and rams open to 200 mm but the maximum stack height (die, punches, and spacers) is 150 mm. The specified maximum die diameter is 100 mm. A thermocouple (K-type, Omega Engineering Inc.) was inserted into the side of the die, the chamber was closed, and the minimum load was then applied (4.7 kN which is 41.6 MPa for a 12 mm die). The SPS machine maintains the minimum load at all times once the die is loaded.

Figure 3.1. Dr. Sinter Lab SPS-515S (SPS Syntex Inc., Kanagawa, Japan) spark plasma sintering machine owned by Boise State University. The process chamber is on the left, the machine controls are on the center unit, and the analysis unit is on the right.

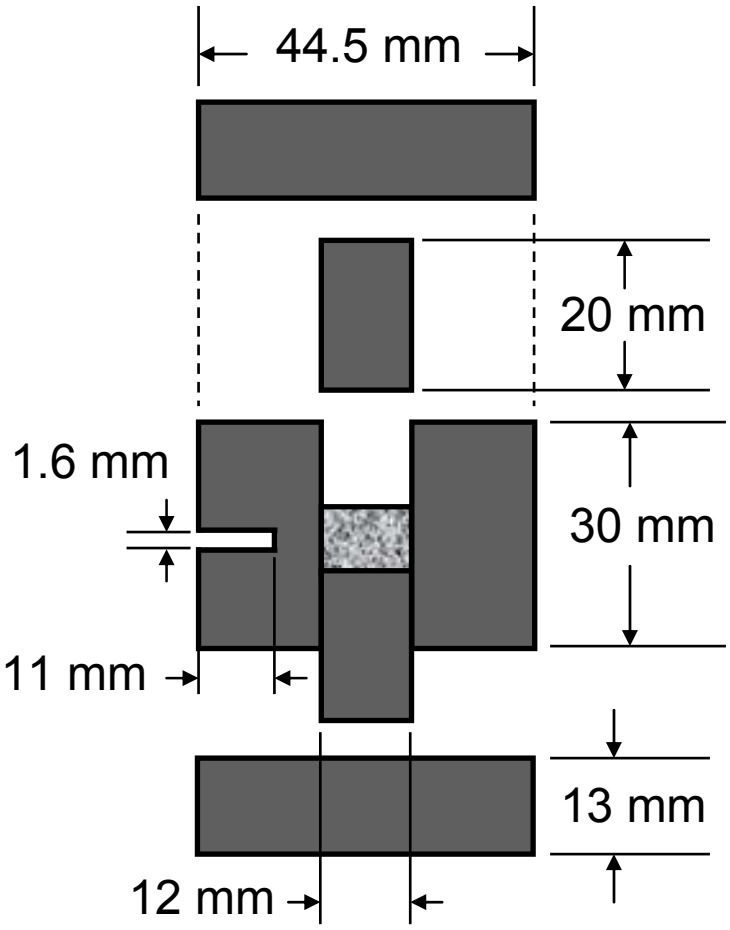

Figure 3.2. Schematic of the die, punches, and spacers that were used to process nickel with SPS. The drawing is to scale, and the dimensions of each piece are given. The nickel powder is represented by the gray object inside the die.

Chino KP1000 programmable controllers (Chino Works America Inc., Los Angeles, CA) allow the user to set load and temperature profiles independently up to the maximum capacity of 50 kN and 2000°C. Voltage and current cannot be controlled directly. A temperature profile is programmed by the user and the current and voltage are adjusted by the SPS unit accordingly, up to a maximum output of 1500 A and 20 V. The DC pulse pattern is programmed as the number of pulses on and the number of pulses off.

The pulse width is 3 ms [12, 15, 27, 83]. The pattern of pulsed DC current was not varied for these experiments; rather the default pulse cycle of 36 ms on and 9 ms off (or approximately 22 Hz) was used. The atmosphere inside the vacuum chamber can be evacuated or be replaced by an appropriate gas. Gas flow through the system is not controllable; the valves to the vacuum pumps are either open or closed. The chamber atmosphere was purged by alternately pumping down the chamber using a roughing pump to 10^{-3} Pa and then flowing argon gas into the chamber. Three purge cycles were performed before starting the sintering process. A chamber pressure of 10^{-3} Pa was maintained during sintering. The time, temperature, voltage, current, and displacement data were collected using LabView version 8.2 software on the attached analysis unit.

Three different sample sets were produced by SPS. The first was produced to investigate how the microstructure changed with temperature, pressure, and dwell time. For each sample, the temperature was ramped at a steady rate to a peak temperature of 500, 650, or 800°C, the temperature was held for 0 to 10 min, and then the current and voltage were shut off. The pressure on the samples was varied between 41.6 and 79.6 MPa. The ramp rate was 100°C/min for the 500 and 800°C samples and 92.9°C/min for the 650°C samples due to machine limitations. To achieve the specified temperature, the SPS machine used voltages of 2-4 V and currents of 200-700 A. For the samples processed at pressures above 41.6 MPa, a pressure profile was run concurrently with the temperature profile. When the experiments at 61.9 and 79.6 MPa began, the pressure was increased from the minimum of 41.6 MPa to the desired value over 1 minute. The peak pressure was maintained throughout the heating and dwell stages then ramped back down to the minimum pressure over 1 min. Figure 3.3 shows an example of temperature and

pressure profiles. With the exception of two samples with controlled cooling rates (discussed below), samples cooled by radiative heat loss and by the water-cooled electrodes. The die were allowed to cool below 250°C before the chamber was purged with air. The die were kept in the machine until they were cool enough to remove by hand, at which point the chamber was opened and the minimum load was released. The cooling rate was dependent on the process temperature and changed with time. Immediately after the voltage and current were shut off, the samples processed at or above 800°C cooled at rates near 100°C/min. The cooling rate slowed to roughly 50°C/min near 500°C and to roughly 25°C near 250°C. The entire process from the beginning of the profile to removing a sample took between 20-35 minutes depending on peak temperature.

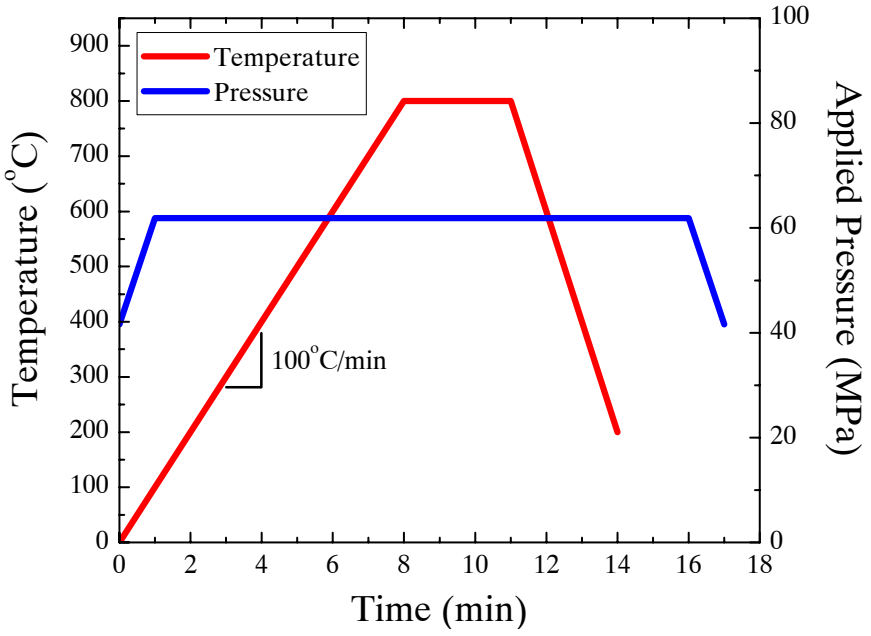

Figure 3.3. Temperature and pressure profile used to sinter nickel by SPS. Plot shows a profile for a sample to be processed at 800°C for 3 min at 61.9 MPa.

The second set of SPS samples was produced to investigate the effect of heating and cooling rates during SPS. Each sample was heated to a peak temperature of 800°C and held for 5 minutes with an applied pressure of 61.9 MPa. Samples were made using different heating rates: 400°C/min, 200°C/min, 100°C/min, 50°C/min, and 25°C/min. Two more samples were heated and cooled at 50°C/min and 25°C/min. The final sample set was produced to investigate neck growth and sintering progression during SPS processing. Seven samples were produced from 400 to 1000°C at a ramp rate of 100°C/min at 61.9 MPa with no dwell at the peak temperature. The process parameter matrix is given in Table 3.1. For some processing conditions, multiple specimens were produced to determine the repeatability of the process.

Table 3.1. Table of the processing conditions used for spark plasma sintering. The number for each process condition is the number of specimens produced to determine the repeatability of the process.

Ramp Rate (°C/min)	Pressure (MPa)	Temp (°C)	0 min dwell	1 min dwell	2 min dwell	3 min dwell	5 min dwell	10 min dwell
400	61.9	800					1	
200	61.9	800					1	
100	41.6	500		3	3	3		
	41.6	800		2	2	2		
	61.9	400	1					
	61.9	500	2	4	3	4		1
	61.9	600	1					
	61.9	700	1					
	61.9	800	2	3	4	3	1	1
	61.9	900	1					
	61.9	1000	1					
	79.6	500		2	2	2		
	79.6	800		2	2	2		
92.9	41.6	650		3	3	3		
	61.9	650	1	3	4	10		1
	79.6	650		2	2	2		
50	61.9	800					1	
25	61.9	800					1	
50-50	61.9	800					1	
25-25	61.9	800					1	

3.3: Conventional Sintering of Nickel

Conventionally sintered (CS) nickel samples were processed with the same powder used in the SPS studies. Five grams of nickel powder were measured in an analytical balance and then poured into a 13 mm diameter circular steel die. The powder was pressed in the die at 500 MPa for two minutes using a Carver 4350 manual press. The green-body pellets were then sintered in an alumina boat covered with niobium foil. The niobium was used to prevent oxidation of the nickel. The CS nickel was sintered in a

CM 1730-12 HT tube furnace in an argon atmosphere. Oxygen was gettered from the system using a Restek 21468 furnace, and an NTron OA-1 oxygen analyzer measured oxygen levels below 1 ppb (beyond the resolution of the analyzer) during sintering. Nine total samples were produced at 900, 1100, and 1300°C with hold times of 0, 1, and 2 hours at each temperature. The heating rate and cooling rates were 5°C/min for all CS specimens.

3.4: Density, Hardness, and Porosity Measurements

A dark gray carbide layer formed on each SPS sample during processing. Therefore, all sample surfaces, including the rounded edges, were ground with 240 grit SiC paper to remove the carbide layer before analysis. Surfaces were ground until no evidence of the carbide layer could be seen visually. The density of each specimen was measured using the Archimedes method on the entire specimen. A Mettler Toledo AB54-S/FACT analytical balance with a density measurement kit package from Mettler Toledo was used for the density measurements. The thermometer packaged with the kit was a Hediger AG Ch-8706 alcohol thermometer with 0.2°C gradations. Each specimen was weighed in air, in water, and then dried with compressed air before then next measurement. The average of three measurements on each specimen is reported.

Using an Allied diamond wafering saw, samples were then sectioned and mounted in Beuhler Probemet conductive mounting compound. Figure 3.3 shows the regions of each sample that were analyzed. The samples produced at 61.9 MPa for 2 min at 500, 650, and 800°C were analyzed on both the cross-sectional and midplane faces shown in Figure 3.4. The analysis on those three samples revealed no differences

between the cross-sectional face and the midplane face using any of the characterization techniques. All of the remaining samples were prepared for analysis on only the cross section.

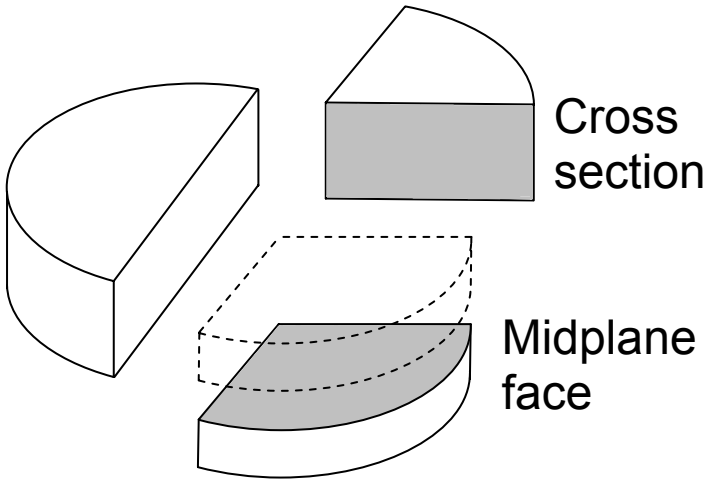

Figure 3.4. Diagram of SPS nickel sample sectioning. Samples were cut along their diameter and then one half was cut again. In order to expose the mid-plane one quarter of the sample was ground half-way through its thickness. The shaded faces were analyzed.

To investigate neck growth, the samples processed from 400 to 1000°C with no dwell were fractured. Half of each sample was mounted to expose the cross section for analysis and the other half was held in a vice and struck with a hammer and punch. The fracture surface of each sample was imaged using a Leo 1430VP SEM.

Vicker's hardness testing requires a sufficiently reflective surface to make optical measurements. Mounted samples were polished with successively finer SiC paper from 240 to 800 grit. A polish to 800 grit was found to be adequate for nickel hardness measurements. Hardness measurements were taken using a Leco DM-400F microhardness tester with a diamond indenter. Each test was performed at 1 kgf for 15 s.

Measurements were taken starting 1 mm from the sample center and spaced 1 mm outward until the sample edge was reached. Five measurements were possible on each sample. Five more measurements were taken on the cross-sectional face in the direction perpendicular to the first set, halfway from the original sample's center. Vicker's hardness values were calculated according to the following equation:

$$H_V = 1.8544F / d_m^{\,2} \tag{3.1}$$

where H_V is the Vicker's hardness value in kgf, F is kilograms of force, and d_m is the mean diagonal of the impression in millimeters. The goal was to determine if temperature gradients during processing created a hardness gradient. No gradient was observed, and therefore reported hardness values are the average of all measurements taken on the sample. To further explore a potential hardness gradient, half of the samples were measured 10 times at the center and 10 times at the edge and a student's t-test was performed to determine any statistically significant difference between the hardness at the center and edge of the sample.

Hardness indentations were removed by grinding with 400 grit SiC paper. Samples were then polished using successively finer paper to 1200 grit followed by 1 and 0.3 μm alumina slurries. The final polishing step was to place each sample on a Buehler Vibromet 2 vibratory polisher with 0.05 μm alumina slurry for 24 h.

Porosity was measured optically using a Ziess Axiovert 200 MAT microscope with an MRc 5 camera. Images were taken at the center and edge of each sample at 200X (an area of approximately 0.125 mm^2). Porosity was then measured from the digital image using ImageJ software. The software was used to partition the image into light and dark areas using the auto-threshold routine. The fraction of dark areas on the

image was taken as the porosity area fraction. Error was estimated by imaging both low and high density samples at the edge and bulk at 100X (approximately 4 times the area of a 200X image) and comparing that value to 5 different images of the same area at 200X.

3.6: SEM and EBSD

All of the samples produced at varying ramp rates and from 400 to 1000°C with no dwell were characterized with EBSD. However, of the samples produced at varying temperature, dwell time, and pressure, those produced at 41.6 MPa for 1 and 2 min and at 79.6 MPa for 1 and 2 min were not characterized beyond what has already been listed. Those samples were excluded after it became evident that differences in the microstructure of samples with dwell times from 1 to 3 min were minimal. The samples that were characterized still allowed for comparison across the full range of temperature, dwell time, and pressure and therefore performing EBSD on the entire sample set was unnecessary.

Microstructural characterization was performed in a Leo 1430VP SEM with an EDAX/TSL Digiview III electron backscatter diffraction detector. The samples were tilted to 70° and an accelerating voltage of 25 kV was used. The SPS samples processed from 400 to 1000°C with no dwell had EBSD performed at the center and all other SPS samples had EBSD performed at the center and the edge. The scan area for the SPS samples was 150×150 μm with a step size of 0.3 μm. The CS samples had EBSD performed near the center of the sample and the scan area was 250×250 μm with a step size of 0.5 μm. Both scan parameter sets yielded 289,289 points per scan and imaged between 700-2000 grains and 5000-8000 grain boundaries. Once the orientation data

were collected using EBSD, the datasets were analyzed using the TexSem Labs OIM software version 5.3 [102]. Each dataset underwent two rounds of neighbor orientation correlation cleanup level 3 and a single iteration of grain dilation with the minimum grain size as 3 pixels. Neighbor orientation correlation level 3 will change the orientation of a single pixel to match that of its neighbors if at least 3 neighbors are of a different orientation [102]. Grain dilation will change the orientation of a pixel which is not part of a grain (determined by the minimum grain size value) to match that of the majority of its neighbors [102]. For grains which are next to pores, the grain dilation routine will expand the grain edge into the pore by one pixel width for each iteration [102]. Each dataset was then partitioned into a set where the minimum grain size was 3 pixels. The minimum misorientation between grains was 5°. The grain boundary character was analyzed as the length fraction of general, Σ1 (5-15°), Σ3, and Σ5-29 boundaries. The diameter of each grain is calculated by first finding the area of the grain, determined by the number of pixels in each grain and the pixel size, and then finding the diameter assuming that the area is circular [102]. The smallest grain diameter the can be resolved using 0.3 and 0.5 μm step sizes are 0.5 and 0.9 μm respectively [102]. The average grain size diameter was reported.

CHAPTER 4: RESULTS

In this chapter, the results of the experiments outlined previously are presented. A discussion of measurement error for each of the characterization techniques is given, followed by the complete characterization of the nickel powder. Results are then given for each of the material properties that were characterized. Results are separated by samples processed with SPS and samples made with conventional sintering (CS) techniques. This chapter will show the values in appropriate figures, but not explicitly call out each value unless appropriate. All values that result from the different characterization techniques are given in the Appendix.

4.1: Error and Repeatability

4.1.1: Measurement Error

This section summarizes the methods in which error was calculated for the different characterization methods. Exact machine error was often unavailable, so the error was estimated by comparing standards or by making assumptions as to the accuracy of the tool. The methods and results are given below.

For density measurements, the balance was certified to 1 mg and displayed to 0.1 mg. The balance was assumed to be accurate only to 1 mg and the rounding error could then be as great as 1 mg per measurement. The thermometer was graduated to 0.2°C but the water density table is only in increments of 0.5°C. The rounding error is then 0.5°C

or a full step in the density table. A density range was calculated using worst-case scenarios: the error is 0.02 g/cm^3. ASTM B 311, a standard for density measurements of sintered materials, states the repeatability index is 0.025 g/cm^3 (any repetition of measurements should not be suspect as long as the measurements fall into that range). To account for buoyancy of trapped air in the samples, 0.001 g/cm^3 should be added to each density calculation, but as the error was found to be an order of magnitude greater than 0.001 g/cm^3, this was ignored. Both the measurement and statistical errors in the density values are small enough that the error bars do not appear on figures.

The machine error for hardness measurements was estimated by comparing measurements on Rockwell hardness standards to tables of equivalent Vickers hardness values. The largest deviation of the measured Vickers hardness value from the tabulated value was approximately 10%. Further, the error in the optical measurement system was estimated. The maximum deviation in measurement, using a 20X objective lens, was found to be 2-3 μm. The total estimated hardness error is therefore approximately ±5 HV.

Porosity error was estimated by imaging both low and high density samples at the sample edge and near the center at 100X (approximately 4 times the area of a 200X image) and comparing that value to 5 different images of the same area at 200X. The maximum deviation of the 200X images from the 100X image was taken as the estimated porosity error. The errors were 2 and 6% for the low and high density samples respectively.

Error in the grain boundary character and average grain size with EBSD was estimated in the same way as the estimated porosity error. An area approximately three

times larger than the standard scan size was imaged on the 500°C, 61.9 MPa, 1 min (low density) and 650°C, 61.9 MPa, 3 min (high density) samples. The larger scans were partitioned into 5 different 150 x 150 μm areas (the size used for data collection). A partition was made in each corner and one in the center. The statistics of the large scan were assumed to be the standard and the maximum deviation of the smaller partitions was taken as the estimated error. The error in grain boundary character distribution is approximately 3% and the average grain size error is approximately 0.2 μm. Where applicable, plots will display the statistical error associated with the measurements.

4.1.2: Repeatability of the SPS Process

Multiple specimens were processed at certain SPS process conditions, as was shown in Table 3.1. Characterization was performed on the first specimen produced, and those results are reported. On the duplicate specimens, only density measurements were taken. An estimate of the repeatability of the SPS process can be made by comparing the densities of the duplicates. The maximum deviation of any individual specimen from the average of all the specimens processed with the same conditions is less than 4% of the theoretical density (e.g., with an average density of 88% theoretical, all samples were within 82-92% theoretical). The standard deviation of the averages is too low to be shown on any plots of density. This shows that the SPS process can consistently produce specimens with similar properties.

4.2: Characterization of the Initial Nickel Powder

The goal of the study was to understand how the microstructure of nickel is affected by SPS processing parameters and to compare SPS to conventional sintering. The nickel powder used in the study was characterized using SEM, EBSD, and a Horiba LA-950 Laser Scattering Particle Size Distribution Analyzer. The results from the particle size analyzer are shown in Figure 4.1. The median particle size was 19.3 μm. The particle size has a bimodal distribution with the strongest peak at 19 μm and a lower and broader peak at 80 μm. The reported particle size from the manufacturer (measured using sieves) is 8-15 μm. SEM images of the nickel powder are shown in Figure 4.2. Figure 4.2a shows that the particles are roughly the same size as reported by the manufacturer and generally uniform in size. The powder is generally spherical with irregular surface texture and sometimes sharp facets. The 80 μm peak is likely due to agglomeration of particles, seen in Figure 4.2b.

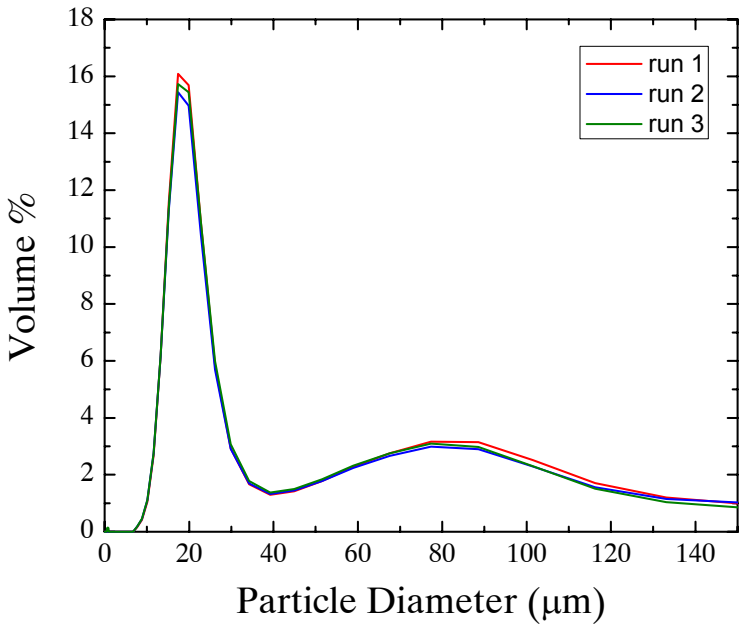

Figure 4.1. Particle size distribution of the nickel powder obtained using a Horiba LA-950 Laser Scattering Particle Size Distribution Analyzer. Three datasets were collected and are all in good agreement.

a) 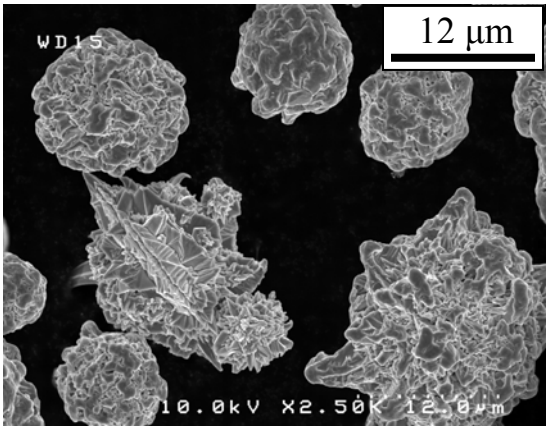

b) 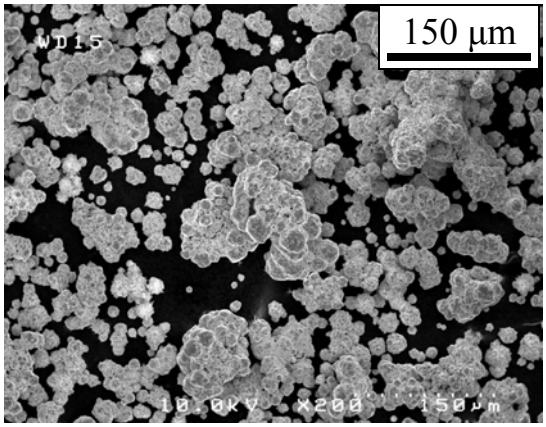

Figure 4.2. SEM images of the nickel powder used in all the experiments, a) shows an image taken at 2500X and b) at 200X.

Electron backscatter diffraction was also performed on the powders in order to determine grain size and grain boundary character. The grain size distribution in the powder is given in Figure 4.3. The grain size in the powder is very uniform, with all of the grains being less than 5 μm in diameter and about 85% being less than 2 μm in diameter. The average grain diameter is 1.3 μm. The grain size is also evident in Figure 4.4 which shows the orientation map of the nickel powder. The colors correspond to different orientations, but for the powder, the orientation is arbitrary as the powders did not have a meaningful orientation when mounted. No preferred grain orientation is observed in the powder. The grains are much smaller than the particles, and each particle contains many grains. Many of the grains are elongated, arranged radially from the center of the powder particle. Elongated grains do not constitute all the of powder particles, many grains are randomly oriented and roughly spherical.

The grain boundary character distribution of the powder shows that 34% of the boundaries are Σ3 boundaries and 55% of the boundaries are special boundaries (Σ1 to Σ29). For all the grain boundary character distribution results, only the Σ3 boundaries had an influence on the total special boundary fraction, and therefore only those two values will be reported. The boundaries are only counted between grains inside the powder particle, the outside edges, where contacts would occur after the powder had been pressed, are not counted.

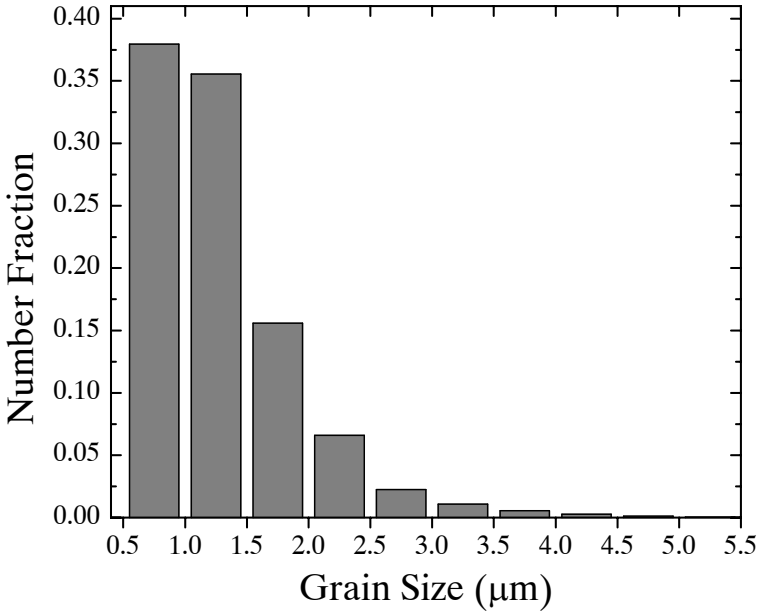

Figure 4.3. Grain size distribution of the as-received nickel powder. The distribution was obtained by performing EBSD on mounted and polished nickel powder.

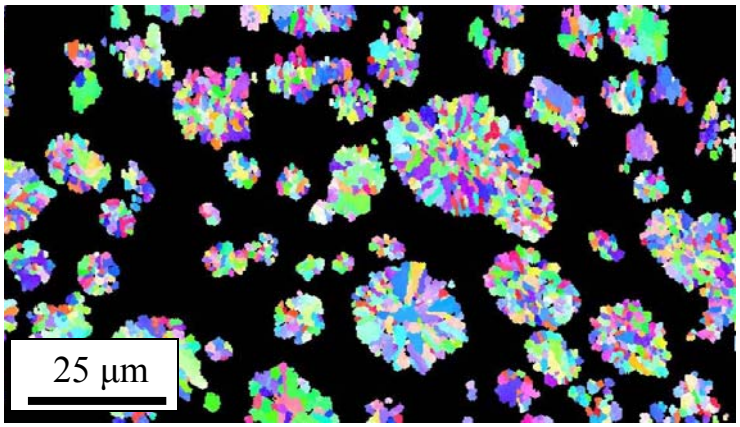

Figure 4.4. Orientation map showing grain size and shape in the as-received nickel powder. The map was obtained by performing EBSD on mounted and polished nickel powder. The colors correspond to different grain orientations.

4.3: Density of Sintered Nickel

4.3.1: Density of SPS Nickel

The effect of the SPS process parameters on the final density can be seen in Figures 4.5 to 4.7. The theoretical density of nickel is 8.9 g/cm^3; the densities ranged from 70 to 97% theoretical density. The steep slope in Figure 4.5 shows that temperature has a strong effect on the density of the SPS nickel samples. At a specified dwell time and pressure, the difference in relative density between samples processed at 500°C and 800°C is approximately 15% of the theoretical density. Dwell time also has an effect, with a trend towards higher densities at longer dwell times. Between 1 and 3 minutes of dwell time, the data are scattered, more so at lower temperatures. At all temperatures, the 10 min dwell results in higher density. The effect of pressure appears to be more significant than dwell time, but less so than temperature. In Figure 4.7, the sample sets are separated by temperature, with the 500°C (red) at the bottom, 650°C (blue) in the middle, and 800°C (green) at the top with no overlap. This indicates that temperature has a more significant effect than pressure. The effect of pressure appears to decrease with increasing temperature. At 500°C, the difference between 42 and 80 MPa is approximately 10% of the theoretical density, but at 800°C, the difference is approximately 8% of the theoretical density.

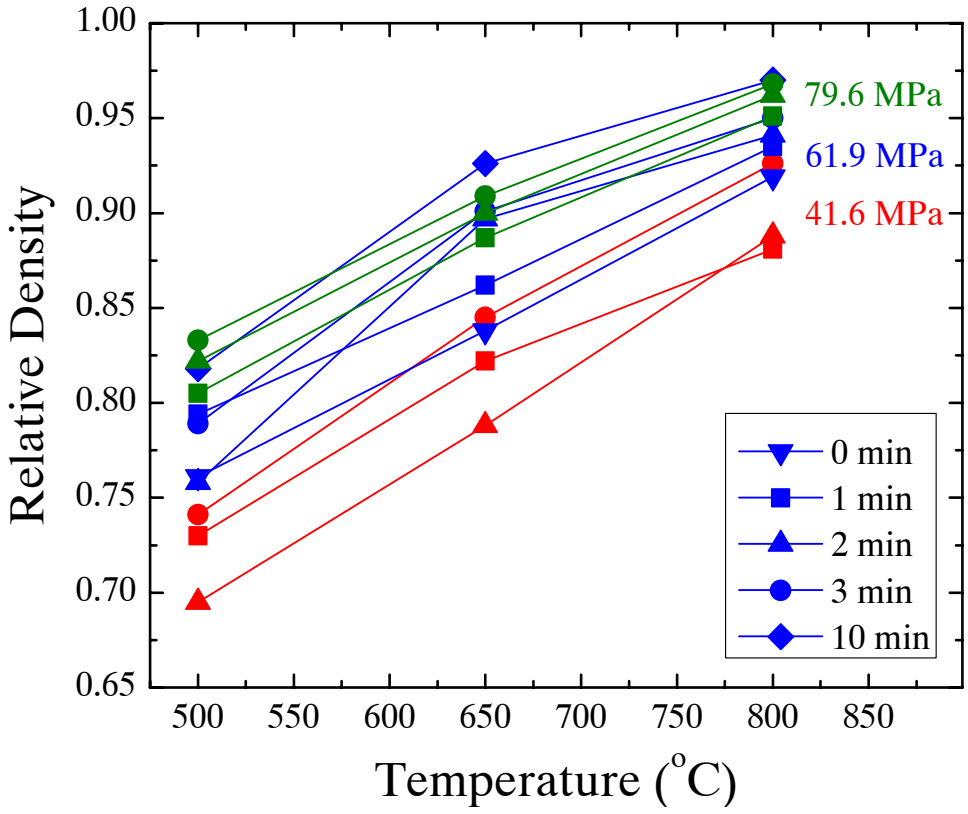

Figure 4.5. Density as a function of temperature for SPS processed nickel specimens. The lines link samples with the same pressure and dwell time across the temperature range. The colors represent the different applied pressures and the symbols the different dwell times.

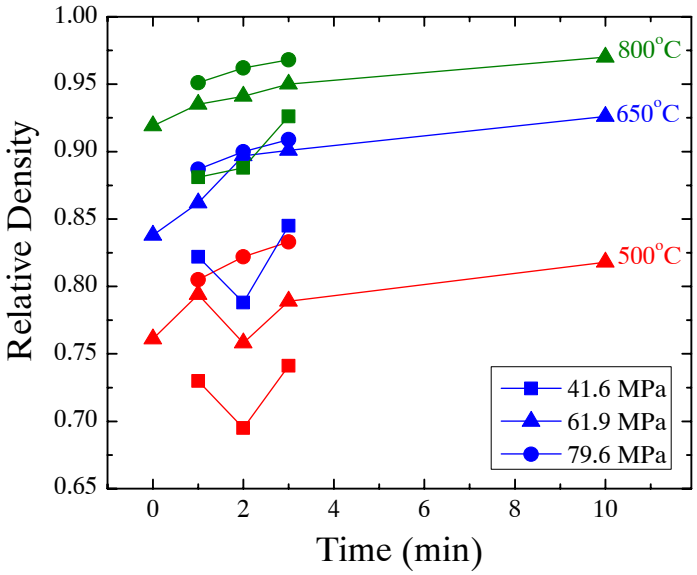

Figure 4.6. Density as a function of dwell time for SPS processed nickel specimens. The lines link samples with the same temperature and pressure. The colors represent the different temperatures and the symbols the different applied pressures.

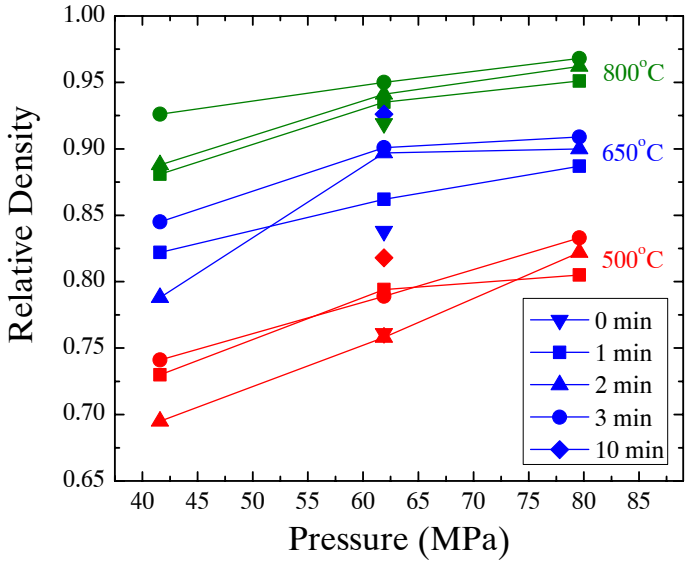

Figure 4.7. Density as a function of applied pressure for SPS processed nickel specimens. Lines connect samples processed at the same temperature and dwell time. The colors represent the different temperatures and the symbols the different dwell times.

The densities of samples with varying ramp rates are plotted in Figure 4.8. The difference in density between the samples with varying ramp rates is very small. The entire range of densities is between 94 and 97% theoretical density. No significant difference between ramp rate and resulting density is seen. The samples that were ramped and cooled at both 25 and 50°C/min are more dense than the samples that were ramped at that rate and allowed to cool quickly, but the difference is only about 1% of the theoretical density.

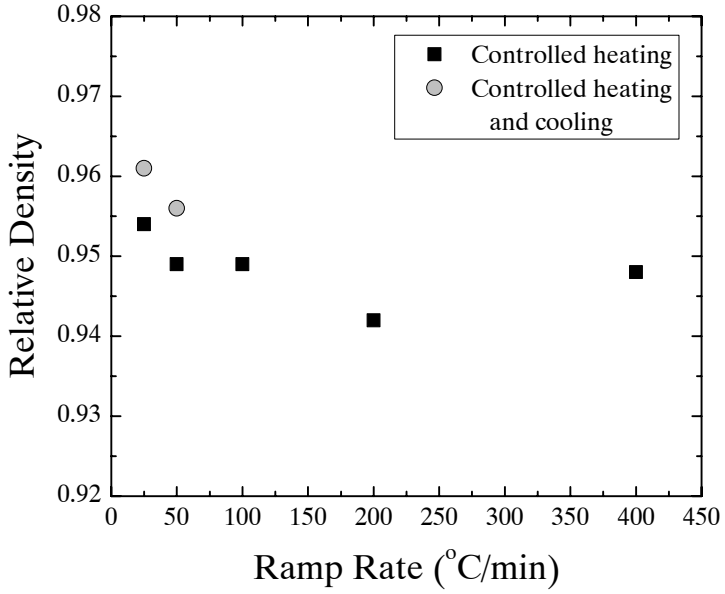

Figure 4.8. Density of SPS nickel samples processed at varying ramp rates. The black squares show samples that were cooled at the limits of the SPS machine and the gray dots are samples that were cooled at the same rate at which they were heated.

The densities of the samples that were ramped at 100°C/min to different final temperatures at 62 MPa with no dwell are plotted in Figure 4.9. The density of these samples ranges from approximately 72 to 97% theoretical density. The slope of density

as a function of temperature is roughly linear. The final temperature has a significant effect on the final density even when the samples are not held at peak temperature.

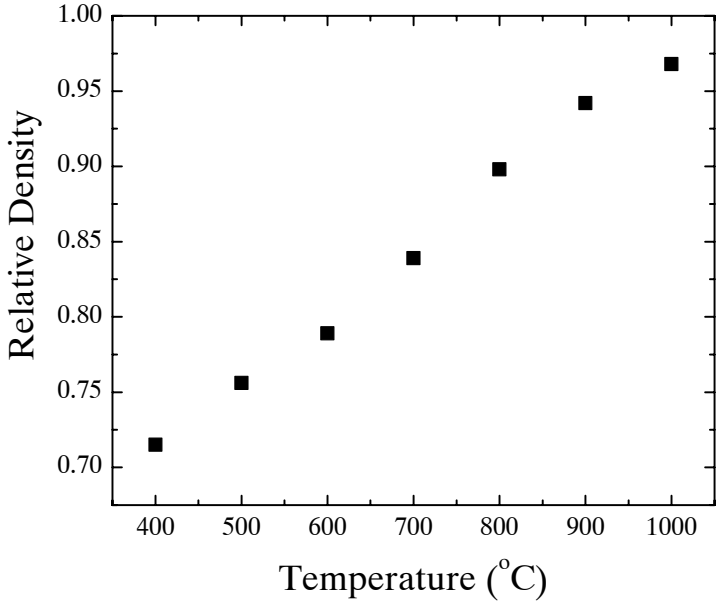

Figure 4.9. Density as a function of temperature of SPS nickel samples heated at 100°C/min, with an applied pressure of 62 MPa, and with no dwell.

4.3.2: Density of CS Nickel

The densities of the CS nickel samples as a function of temperature and dwell time are given in Figures 4.10-4.11. The density of the CS samples ranges from 76 to 90% of theoretical density. The effect of temperature is clearly demonstrated by a change in density of about 10% theoretical density from 900 to 1300°C. Density increases from no dwell to a dwell of 1 hour, and then decreases at a dwell of 2 hours. The increase in density with each step in temperature is 4-6% of the theoretical density.

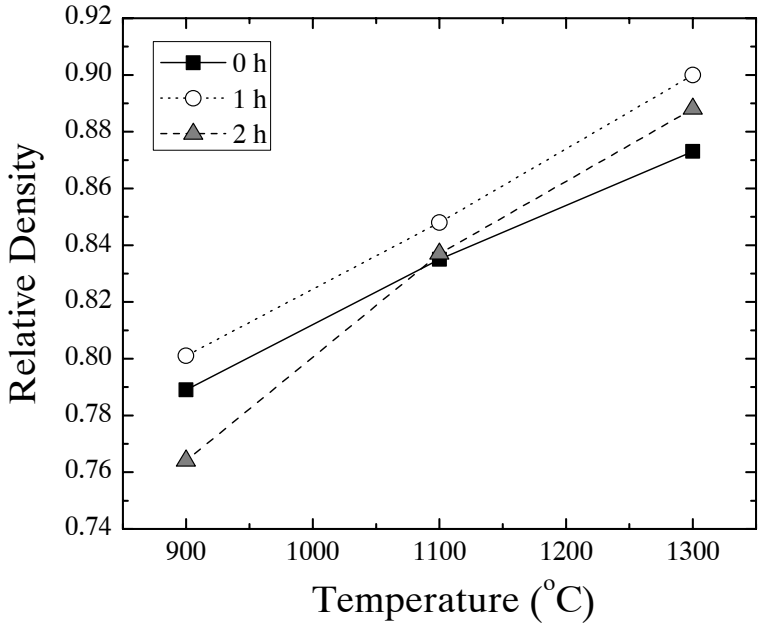

Figure 4.10. Density of CS nickel samples as a function of temperature. The symbols represent different dwell times connected by the lines.

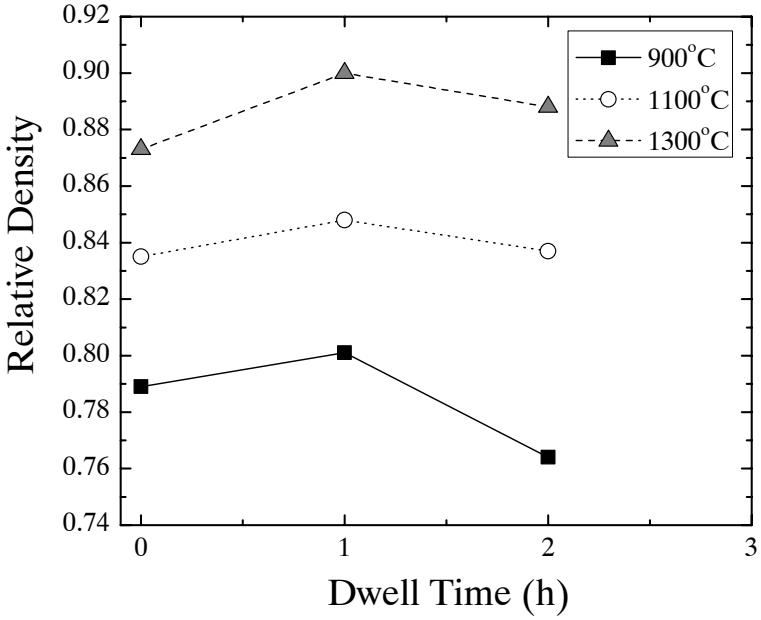

Figure 4.11. Density of CS samples as a function of dwell time. The symbols indicate different temperatures connected by the lines.

4.4: Hardness Results

4.4.1: Hardness of SPS Nickel Samples

Examples of hardness indentations are shown in Figure 4.12. The hardness of the SPS nickel samples as a function of relative density and as a function of both average grain size and relative density is shown in Figures 4.13 and 4.14. The hardness values ranged from 34 to 122 Hv. The standard deviation of hardness measurements was generally smaller than the machine error of 5 Hv. Of the samples that were indented 10 times at the center and edge, only three (500°C, 3 min, 62 MPa, 800°C, 1 min, 62 MPa, and 800°C, 3 min, 80 MPa) were statistically harder at the center than at the edge. The hardness as a function of density plot in Figure 4.13 shows that hardness scales linearly with density with the exception of the ramp rate samples whose values fall just above the upper right end of the line. The hardness of the SPS nickel samples processed from 400 to 1000°C with no dwell was not measured. No other property showed such a strong correlation with hardness. The separation by temperature, with the lowest temperature at the bottom and highest at the top, shows the significant effect that temperature has on density and hardness. In Figure 4.14, the plot of grain size, density and hardness, the hardness increases with both density and grain size.

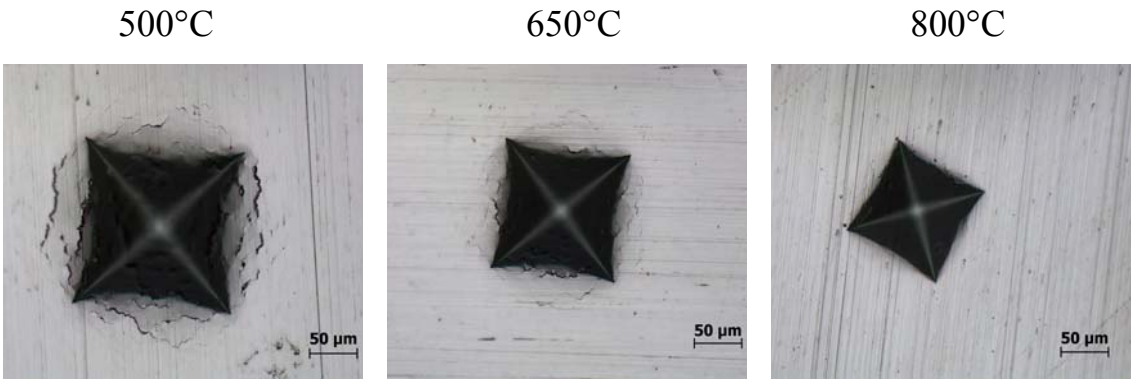

Figure 4.12. Optical images of hardness indentations of SPS nickel samples processed at 41.6 MPa, for 1 min, at three different temperatures. The samples were polished to 800 grit before the hardness testing.

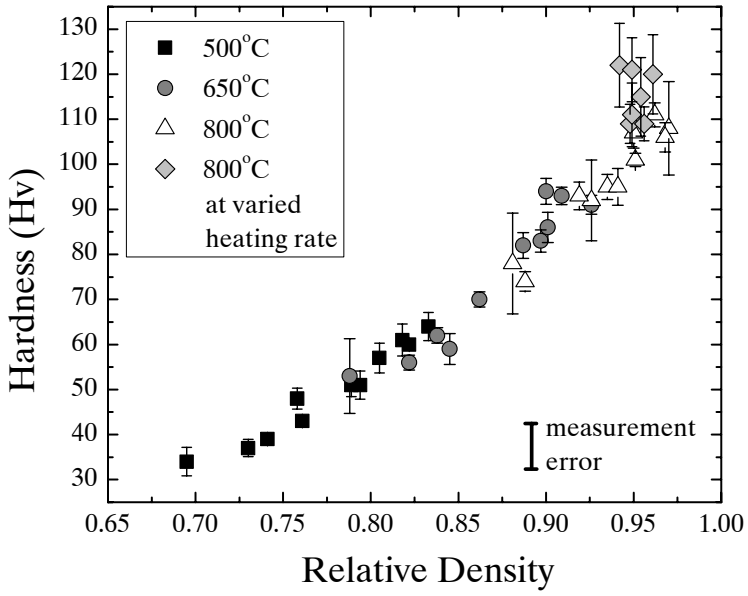

Figure 4.13. Hardness of all SPS nickel samples produced at varying temperature, dwell time, and applied pressure as a function of density. The symbols indicate the different processing temperatures and heating rates. The error bars represent the standard deviation of the hardness measurements.

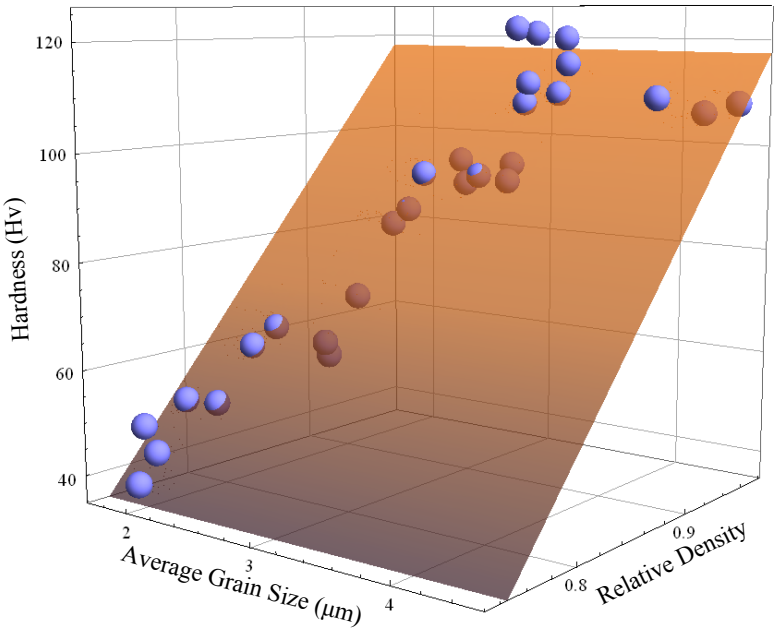

Figure 4.14. Hardness as a function of average grain size and relative density of SPS nickel. The dots are the actual values, and the shaded plane represents a fit of hardness to average grain size and relative density.

4.4.2: Hardness of CS Nickel Samples

The hardness of the CS nickel samples as a function of density and both grain size and density is shown in Figures 4.15 and 4.16. Hardness values for CS nickel range from 41 to 78 Hv. The standard deviation was larger than the machine error for about half of the samples suggesting non-uniformity of the microstructure. The hardness of the CS nickel scales linearly with density, with a very similar slope to that of the SPS nickel. Hardness of CS nickel also increases with both density and grain size as was seen with the SPS nickel.

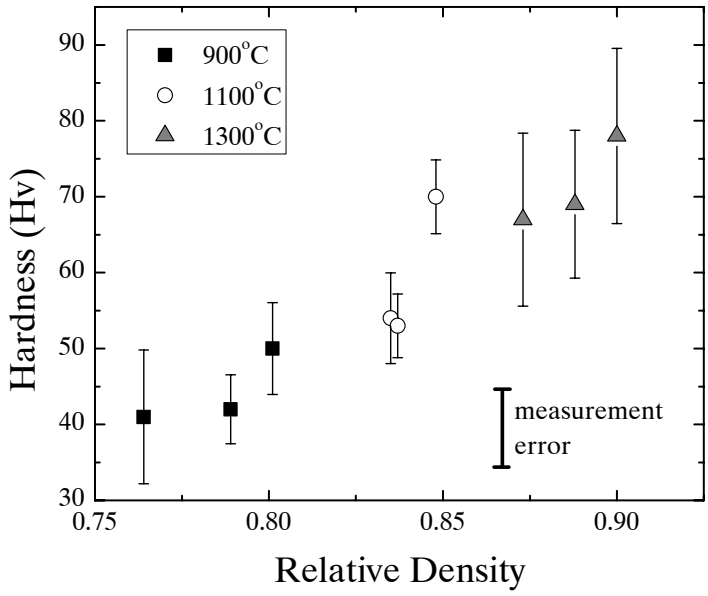

Figure 4.15. Hardness of all CS nickel samples as a function of density. The symbols correspond to the different temperatures. The error bars represent the standard deviation of the hardness measurements.

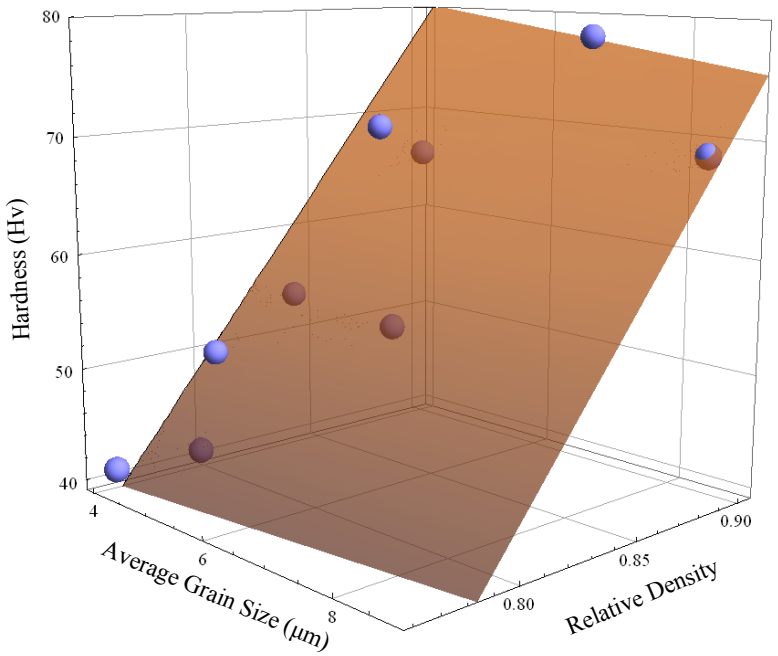

Figure 4.16. Hardness of all CS nickel samples as a function of average grain size and relative density. The dots are the actual values, and the shaded plane represents a fit of hardness to average grain size and relative density.

4.5: Porosity Results

4.5.1: Porosity of SPS Nickel

The porosity at the center and edge of the SPS samples produced at varying temperature, dwell time, and pressure is as a function of density in Figure 4.17. The porosity values range from 32% down to 4%. This range is nearly identical to what would be expected given the range of density values from 70 to 97% theoretical density. Both the center and edge values are generally above the values that would be expected for their corresponding density. The difference between porosity at the center of the sample and the edge ranges from 0 to 9% porosity with no obvious trend. The average of all the differences is 3%. Linear fits of the porosity at the center and edge, shown by the

lines in Figure 4.17, show that the samples do tend to show a greater difference in porosity at higher densities as seen by the slightly different slopes of the lines. This increasing difference in porosity with density was observed in optical micrographs. Figure 4.18 shows an optical micrograph of the cross section of the SPS nickel produced at 800°C, 61.9 MPa, for 3 min. The pores tend to be uniformly distributed over much of the sample, but are more concentrated towards the edge at approximately the mid point between the top and bottom edges. Nearly all of the SPS samples showed this localized concentration of porosity at the edge, which was more pronounced at higher densities.

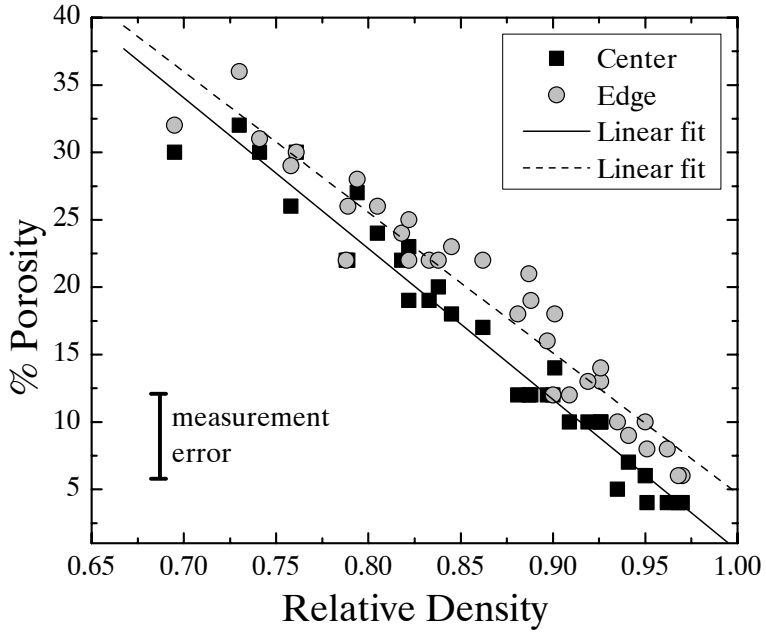

Figure 4.17. Porosity of all SPS nickel samples produced at varying temperature, dwell time, and applied pressure as a function of density. The black squares are the measurements taken at the center of the sample, and the gray dots are measurements taken at the edge of the sample. The lines represent linear fits of the porosity values at the center and the edge.

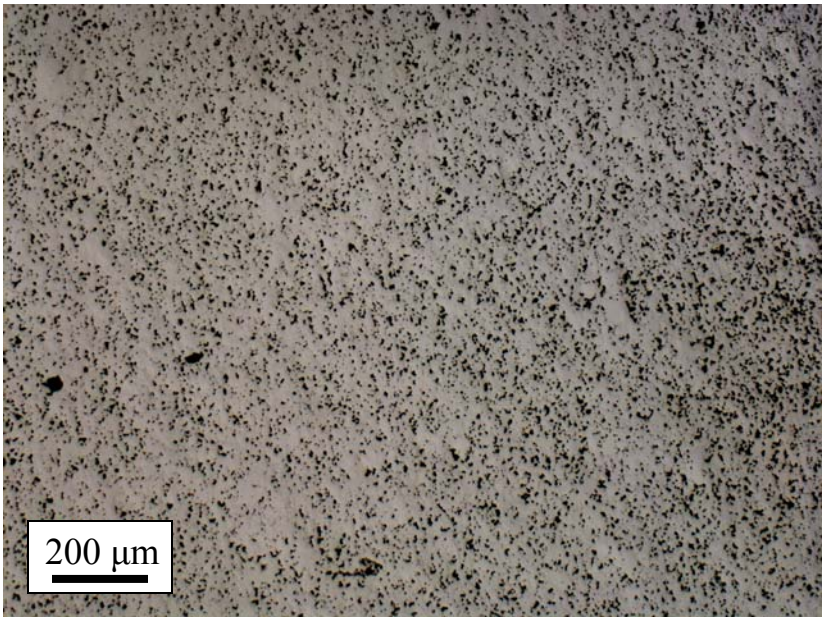

Figure 4.18. Optical micrograph of the cross section of the SPS nickel sample produced at 800°C for 3 min at 61.9 MPa. The micrograph shows the distribution of porosity across the sample. The right edge of the micrograph is the edge of the sample.

4.5.2: Porosity of CS Nickel

The porosity of the CS nickel as a function of density is shown in Figure 4.19. The porosity values range from 4 to 26%. There is no significant difference between the porosity at the center and edge of the CS nickel samples. With the exception of 3 outliers, the porosity scales with density.

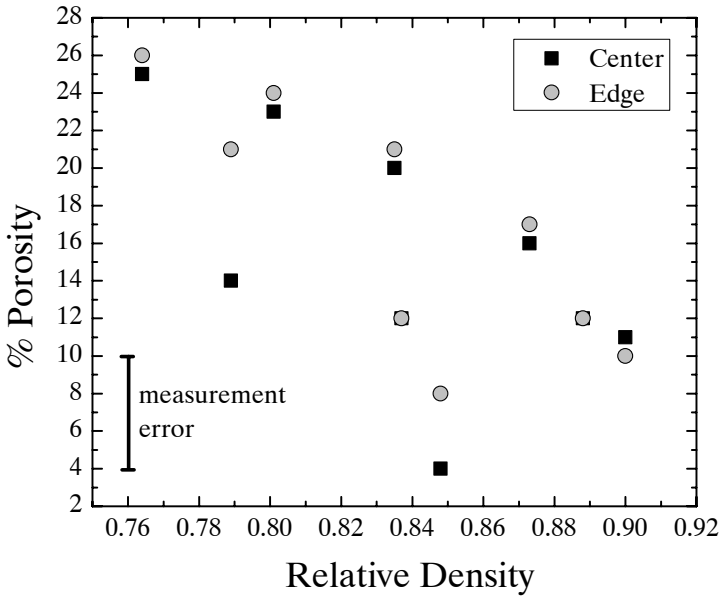

Figure 4.19. Porosity of all CS nickel samples as a function of density. The black squares correspond to measurements taken at the sample center and the gray dots to measurements at the sample edge.

4.6: Grain Size Results

4.6.1: Grain Size Results for SPS Nickel

The average grain sizes for the SPS samples produced at varying temperature, dwell time, and applied pressure as a function of density is shown in Figure 4.20. Average grain sizes range from about 1.6 μm to 4.8 μm. No significant difference is observed in the grain size at the center and edge of the sample; the average difference of all the samples is equal to the measurement error. Future references to grain size will refer to measurements at the center of the sample. Plots of average grain size as a function of temperature and dwell time are shown in Figures 4.21 and 4.22. Applied pressure did not show any correlation to average grain size and is not shown. Average grain sizes for samples processed at different ramp rates all had grain sizes near the value

expected given the temperature and dwell time, except for the sample that was heated at 400°C/min, where the average grain size was 4.1 μm. The average grain sizes for samples processed from 400 to 1000°C with no dwell are shown in Figure 4.23 as a function of temperature.

Grain size values range from 1.6 to 4.5 μm for all the SPS nickel samples. The standard deviation of the grain size distribution is typically as large as the average grain size. This is due to the wide distribution of grain sizes. Figure 4.24 shows the grain size distributions for the samples processed from 400 to 1000°C with no dwell. At a dwell time of zero, the average grain size increases linearly with temperature up to 900°C then shows a sharp increase at 1000°C. Average grain size also increases with dwell time, and the rate shows a temperature dependence. Grain growth (Figure 4.22) is roughly linear and increases with increasing temperature. With the exception of the sample processed at 400°C/min, the average grain size does not change with ramp rate.

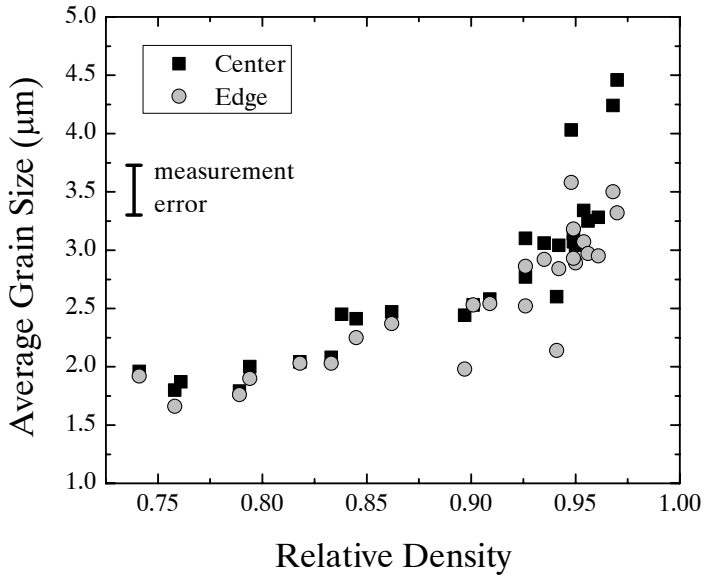

Figure 4.20. Average grain size as a function of density for all the SPS nickel samples. Black squares are measurements taken at the center of the sample and gray dots at the edge.

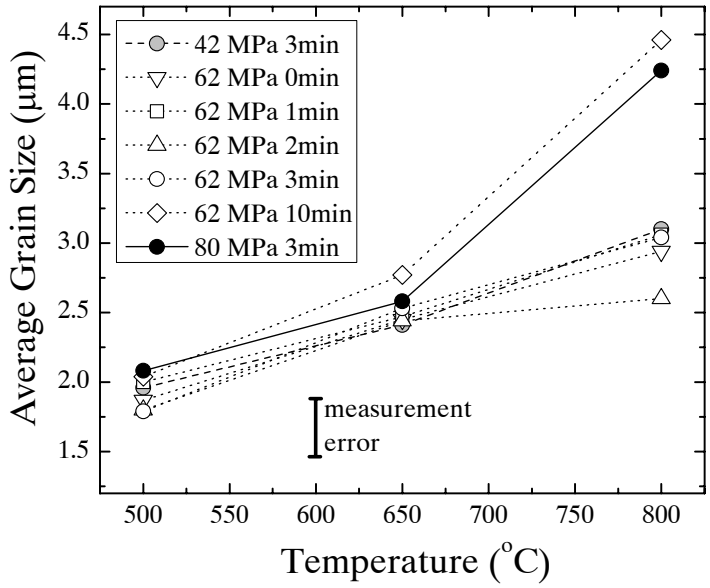

Figure 4.21. Plot of average grain size as a function of temperature for SPS nickel. Colors correspond to applied pressure and symbols to the dwell time. Lines connect samples processed at the same dwell time and applied pressure.

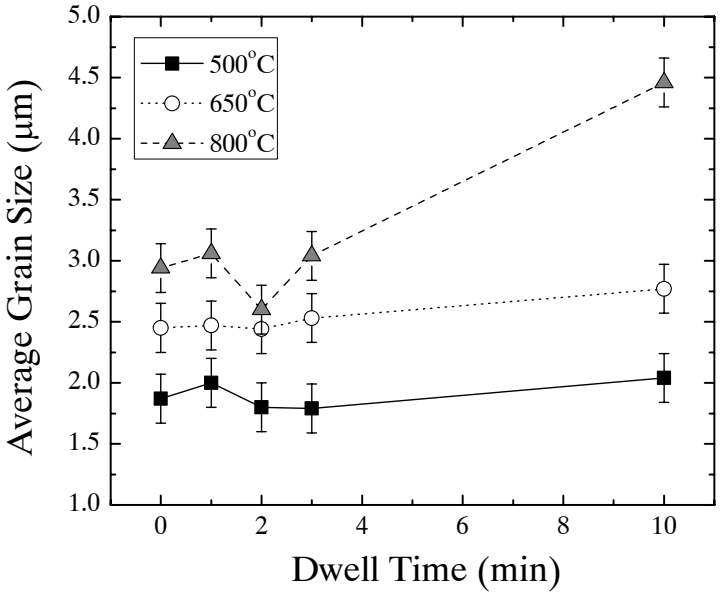

Figure 4.22. Plot of average grain size as a function of dwell time for SPS nickel samples processed at 61.9 MPa. The symbols represent the different temperatures. Lines connect samples processed at the same temperature.

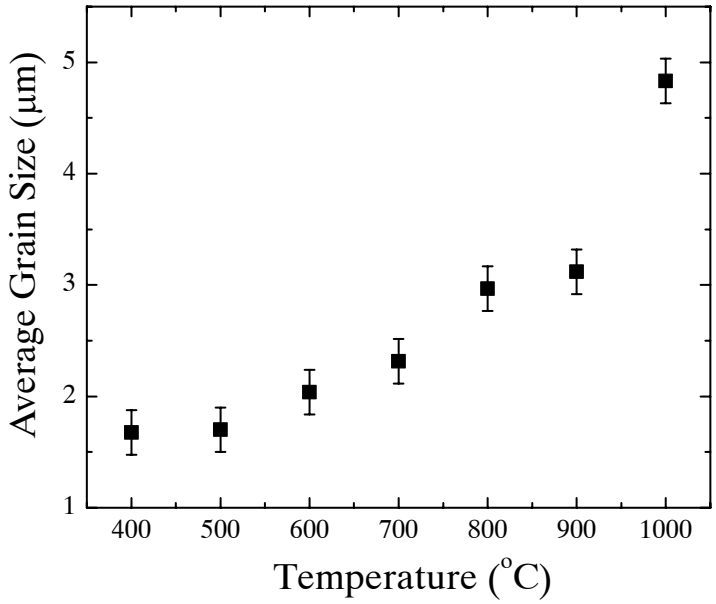

Figure 4.23. Average grain size of SPS nickel processed from 400 – 1000°C at 61.9 MPa with no dwell. The error bars represent the average grain size measurement error.

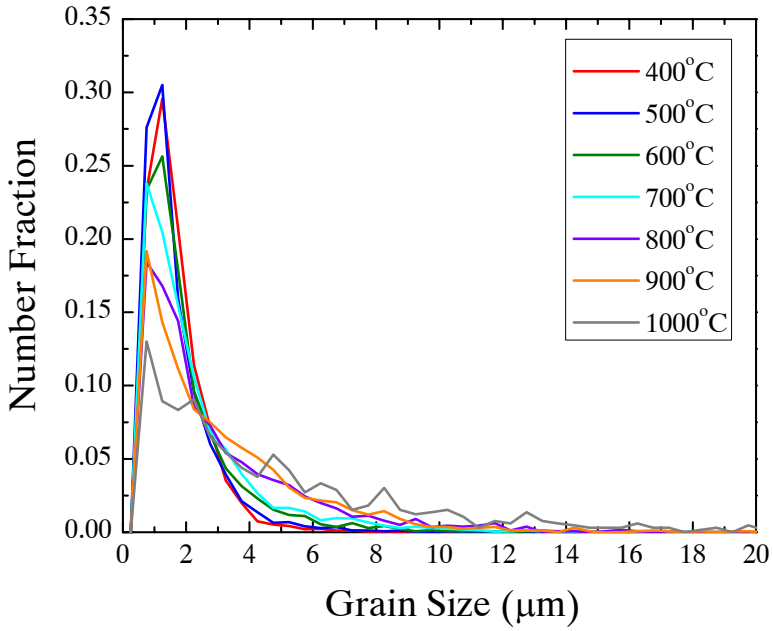

Figure 4.24. Grain size distribution for SPS nickel processed from 400 – 1000°C at 61.9 MPa with no dwell. Each line represents a different process temperature.

4.6.2: Grain Size Results for CS Nickel

The average grain size for CS nickel samples as a function of dwell time is shown in Figure 4.25. The grain size varies from 4.1 to 8.7 μm for the CS nickel samples. At 900°C, the average grain size is time independent, but the effect of time increases with increasing temperature. Further, with no dwell, the grain growth is essentially temperature independent but with increasing dwell time grain growth shows an increasing dependence on temperature

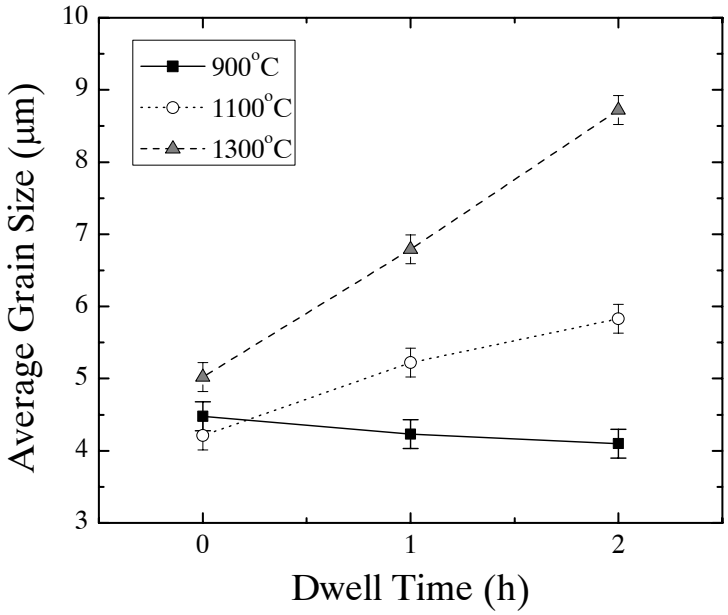

Figure 4.25. Average grain size for CS nickel shown as a function of dwell time. The symbols correspond to the temperatures. The error bars represent the average grain size measurement error.

4.7: Grain Boundary Character Results

4.7.1: Grain Boundary Character of SPS Nickel

Differences between the grain boundary character distribution at the center and edge of each sample were much less than the error in measurement and therefore are not given. The fractions of Σ1 and Σ5-29 boundaries were always below 12 and 16%, respectively and did not change significantly with any process condition. Therefore, figures will only show the Σ3 and total special fraction. Plots of the grain boundary fraction as a function of temperature and dwell time are shown in Figures 4.26 and 4.27. Figures 4.26 and 4.27 show the same data, but Figure 4.26 shows the effect of dwell time at constant temperature, and Figure 4.27 shows the effect of temperature at constant dwell time. The applied pressure did not have an effect on the grain boundary character. No temperature or time dependence on the fraction of Σ3 boundaries is observed at short processing times where the Σ3 fraction remains nearly constant and similar to the Σ3 fraction found in the initial nickel powder. When a dwell time of 10 min is reached, a strong temperature dependence is observed as seen in Figure 4.27. The Σ3 fraction increases from 30 to 45% from 500 to 800°C at 10 min.

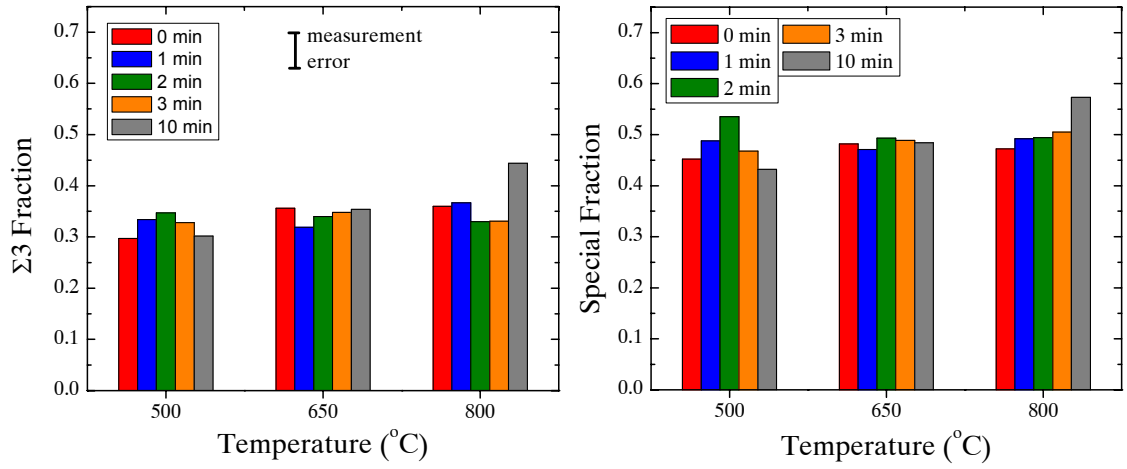

Figure 4.26. Fraction of Σ3 and special boundaries in SPS nickel as a function of dwell time at constant temperature. The colors correspond to the dwell time.

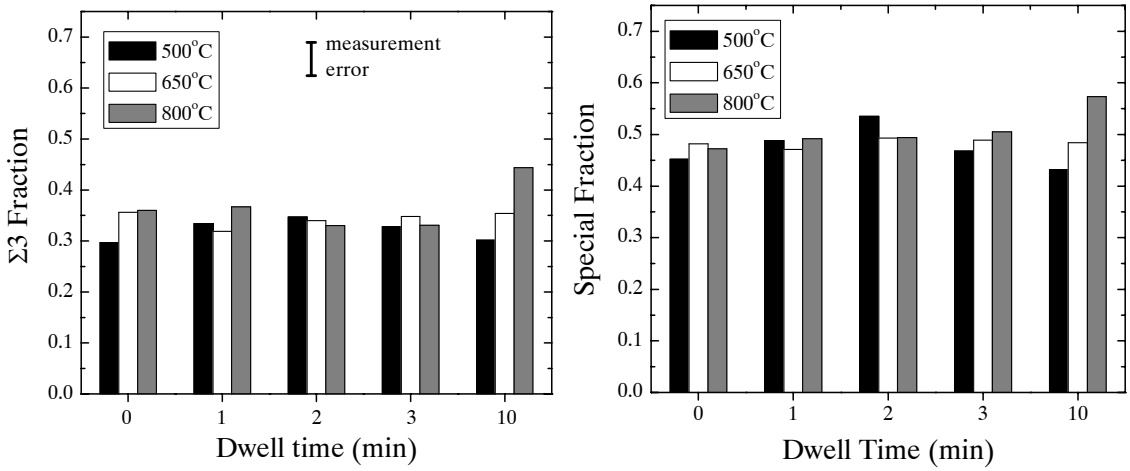

Figure 4.27. Fraction of Σ3 and special boundaries in SPS nickel as a function of temperature at constant dwell time. The colors correspond to the process temperatures.

The Σ3 and special fractions in samples produced at varying ramp rates showed no correlation between ramp rate and grain boundary character distribution. The Σ3 and special fractions of the samples processed at different ramp rates were nearly identical to those of the samples processed at the same temperature and pressure (800°C, 61.9 MPa)

for 1, 2, 3 min. No further discussion or analysis of these samples with respect to grain boundary character distribution will be presented.

The Σ3 and special fractions for the samples processed from 400 to 1000°C with no dwell are shown in Figure 4.28. The Σ3 and special fractions remain constant with temperature until 1000°C, where the Σ3 boundary fraction increases from 35 to 50% and the special fraction from approximately 53 to 60%. Below 1000°C, the values remain near those seen in the initial nickel powder.

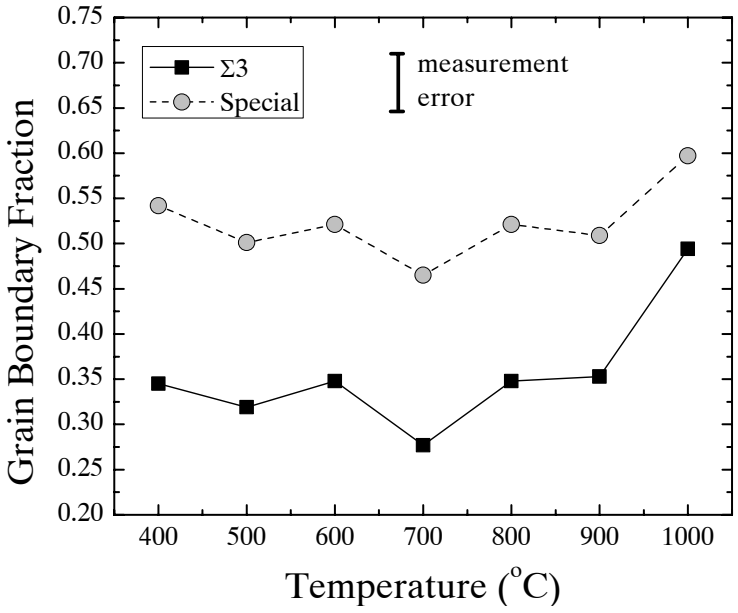

Figure 4.28. Grain boundary character distribution of SPS nickel samples processed from 400 to 1000°C at 61.9 MPa with no dwell. The black points are the Σ3 values and the gray points are the total special boundary fraction.

4.7.2: Grain Boundary Character of CS Nickel

The Σ3 and special fractions for the CS nickel samples are shown as a function of process parameters in Figures 4.29 and 4.30. Figure 4.29 shows the effect of dwell time

at constant temperature, and Figure 4.30 shows the same data, but as the effect of temperature at constant dwell time. The fraction of special boundaries varied from 45%, for both the 1100°C, no dwell and 900°C, 2 h dwell, to 59% for the 1300°C, 2 h dwell, and the fraction of twin boundaries varied from 33 to 49% respectively. No temperature dependence on the fraction of special boundaries is observed at no dwell or at a dwell of 1 h, but at a dwell time of 2 h the fraction of special boundaries increases with increasing temperature as seen in Figure 4.30. No consistent trend is observed in the total fraction of special boundaries with dwell time, but at 1300°C the fraction of special boundaries does increase with dwell time, mainly due to the increase of Σ3 boundaries, as seen in Figure 4.29. Figure 4.29 shows the Σ3 boundaries increase from approximately 40 to 50% at 1300°C from 0 to 2 h, which is a statistically significant increase. Figure 4.30 shows that at a dwell of 2 h, the Σ3 boundary fraction increases from 33 to 50% from 900 to 1300°C, which is also statistically significant.

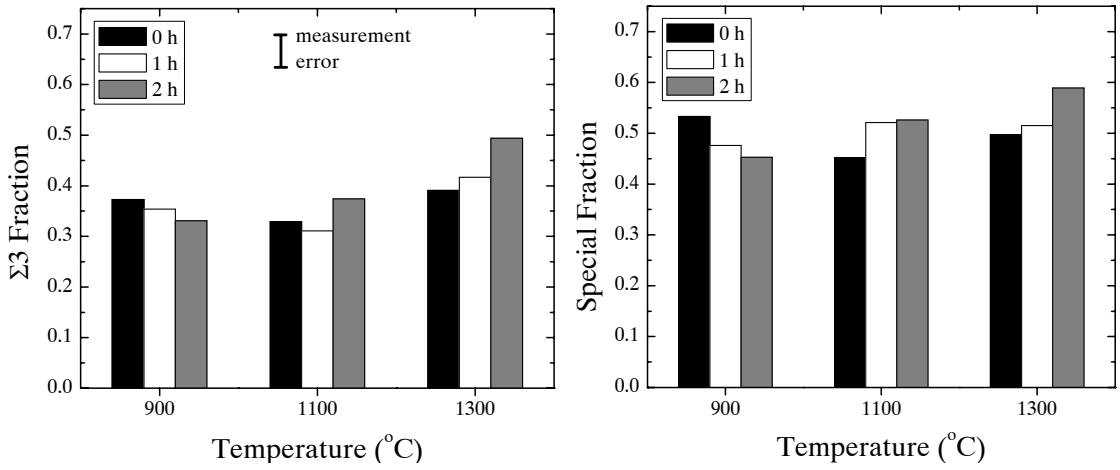

Figure 4.29. Fraction of Σ3 boundaries in CS nickel as a function of dwell time at constant temperature. The colors correspond to the dwell time.

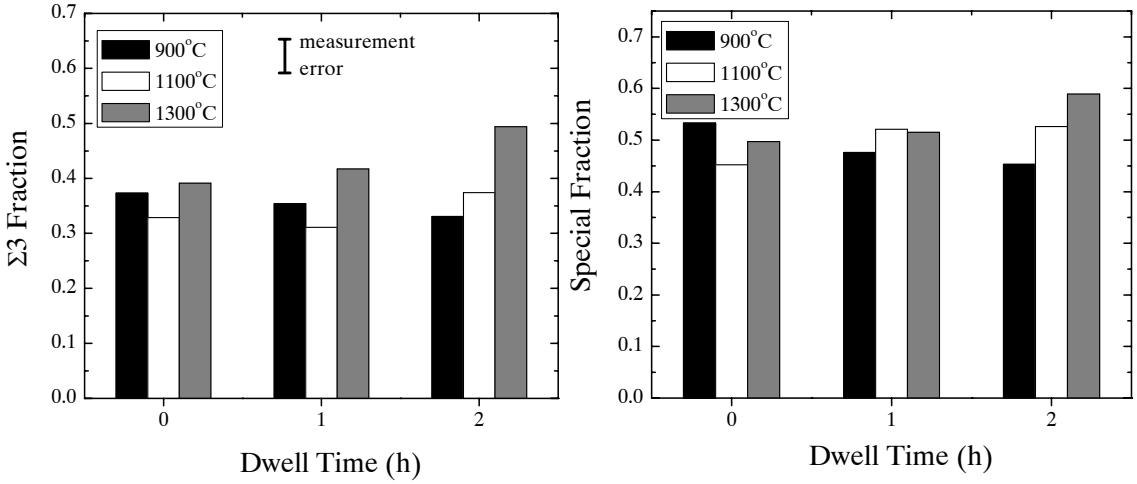

Figure 4.30. Fraction of Σ3 boundaries in CS nickel as a function of temperature at constant dwell time. The colors correspond to the temperature.

4.8: SEM of SPS Nickel Fracture Surfaces

Pieces of the SPS nickel specimens processed from 400 to 1000°C with no dwell were fractured in order to investigate the microstructure using SEM. Not all samples fractured using the method described in Section 3.4. The samples processed at 400 and 500°C did not deform and fractured easily. The sample processed at 600°C began to deform before ultimately fracturing and the deformation before fracture increased with the samples processed at 700 and 800°C. Significant deformation was induced in the sample processed at 800°C before it fractured. The sample processed at 900°C did not fracture, but continued to deform until it was ultimately of no use for investigating particle bonds. No attempt was made to fracture the sample processed at 1000°C.

Micrographs of the fracture surfaces of the samples processed from 400 to 800°C are shown in Figures 4.31-4.32. The fracture surface of the sample processed at 400°C does not show significant signs of necking, but still looks similar to a pressed, green-body pellet. As the temperature increases to 500 and 600°C, neck formation is more evident, and previous necks can be seen in Figure 4.32. The micrographs of the samples processed at 700 and 800°C look more like a true fracture surface, where the rough surfaces look to be caused by the tearing motion used during fracture, and do not resemble the rough surfaces of the initial powders.

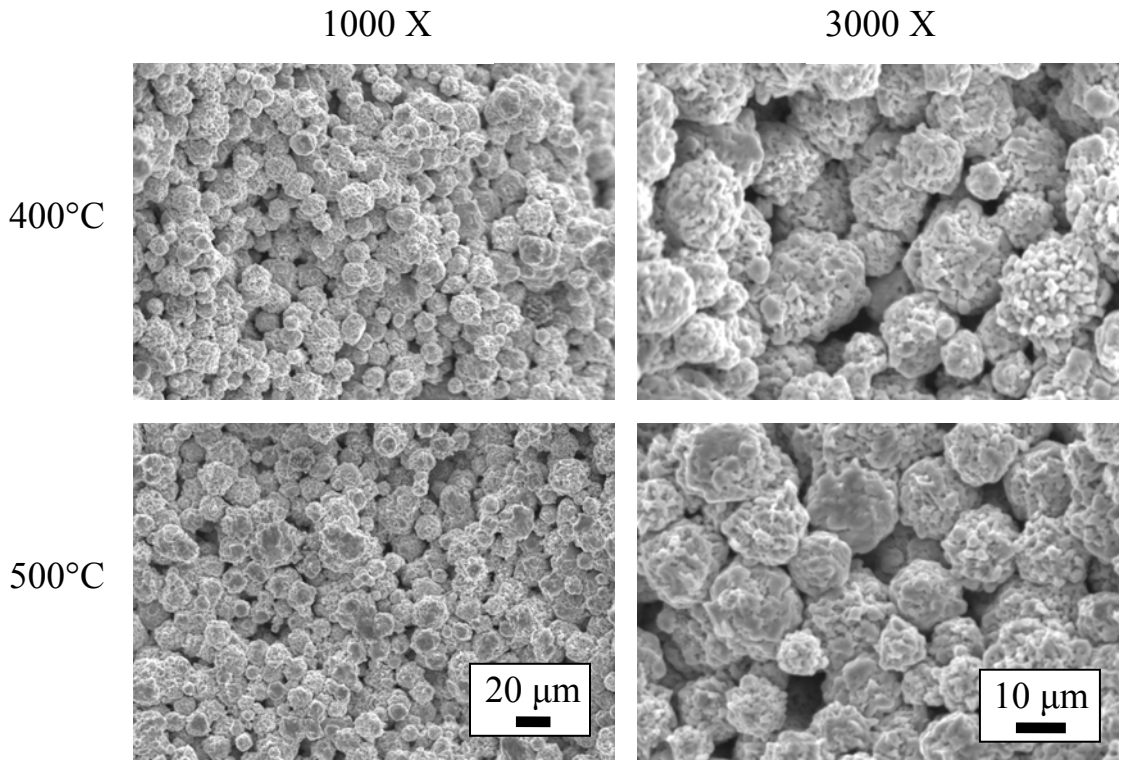

Figure 4.31. SEM images of the fracture surfaces of SPS nickel produced at 400 and 500°C at 61.9 MPa with no dwell. Two magnifications are shown for each specimen. The scale bar is the same at each magnification.

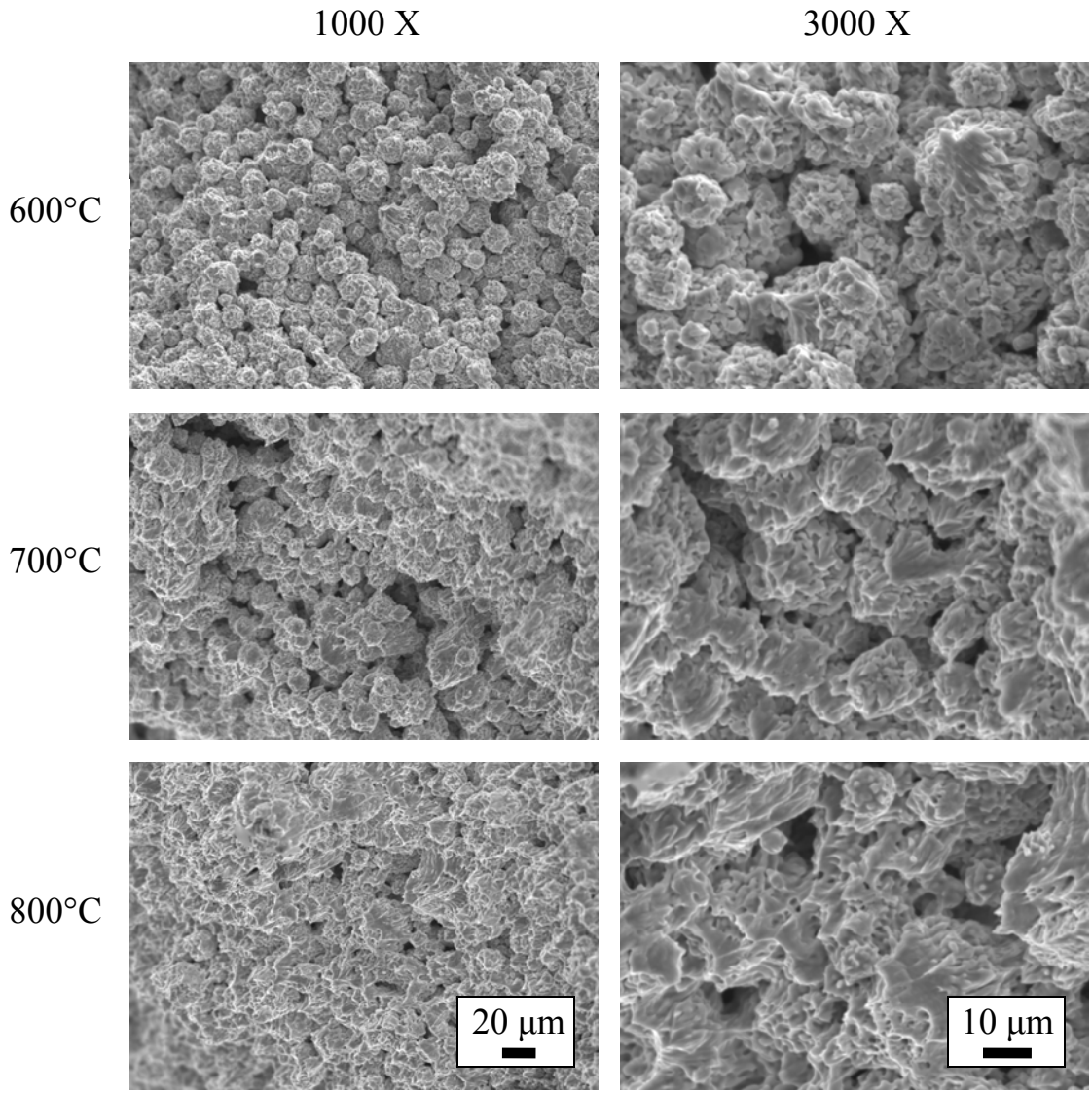

Figure 4.32. SEM images of the fracture surfaces of SPS nickel produced from 600 to 800°C at 61.9 MPa with no dwell. Two magnifications are shown for each specimen. The scale bar is the same at each magnification.

4.9: Microstructural Evolution

4.9.1: Microstructural Evolution of SPS Nickel

Characterization with EBSD allows for creation of orientation maps which visually show the grain size, grain orientation, and porosity. Orientation maps as a function of process conditions shows how the microstructure evolves from powder to a sintered structure. The orientation maps for the SPS nickel produced from 400 to 1000°C with no dwell are shown in Figure 4.33. The orientation maps for SPS nickel produced at varying temperature, dwell time, and applied pressure are shown in Figures 4.34 and 4.33. The orientation maps for the SPS nickel processed at varying ramp rates are not shown. In Figure 4.33, the effect of temperature on density is easily seen as the porosity decreases with increasing temperature. From 400 to 600°C, the microstructure becomes more dense, but also the grains grow within the powder particles. At 700°C, the microstructure changes from a collection of particles to a more uniform structure. At 1000°C, almost no porosity is visible and the grains have grown significantly.

In Figure 4.34, the effect of time on density and grain size is not apparent at 500 and 650°C. However, at 800°C the increasing dwell time leads to a significant increase in grain size and a decrease in porosity. The effect of pressure on the microstructure is apparent at all temperatures (Figure 4.35). At each temperature, the porosity decreases and grain size increases with increased applied pressure.

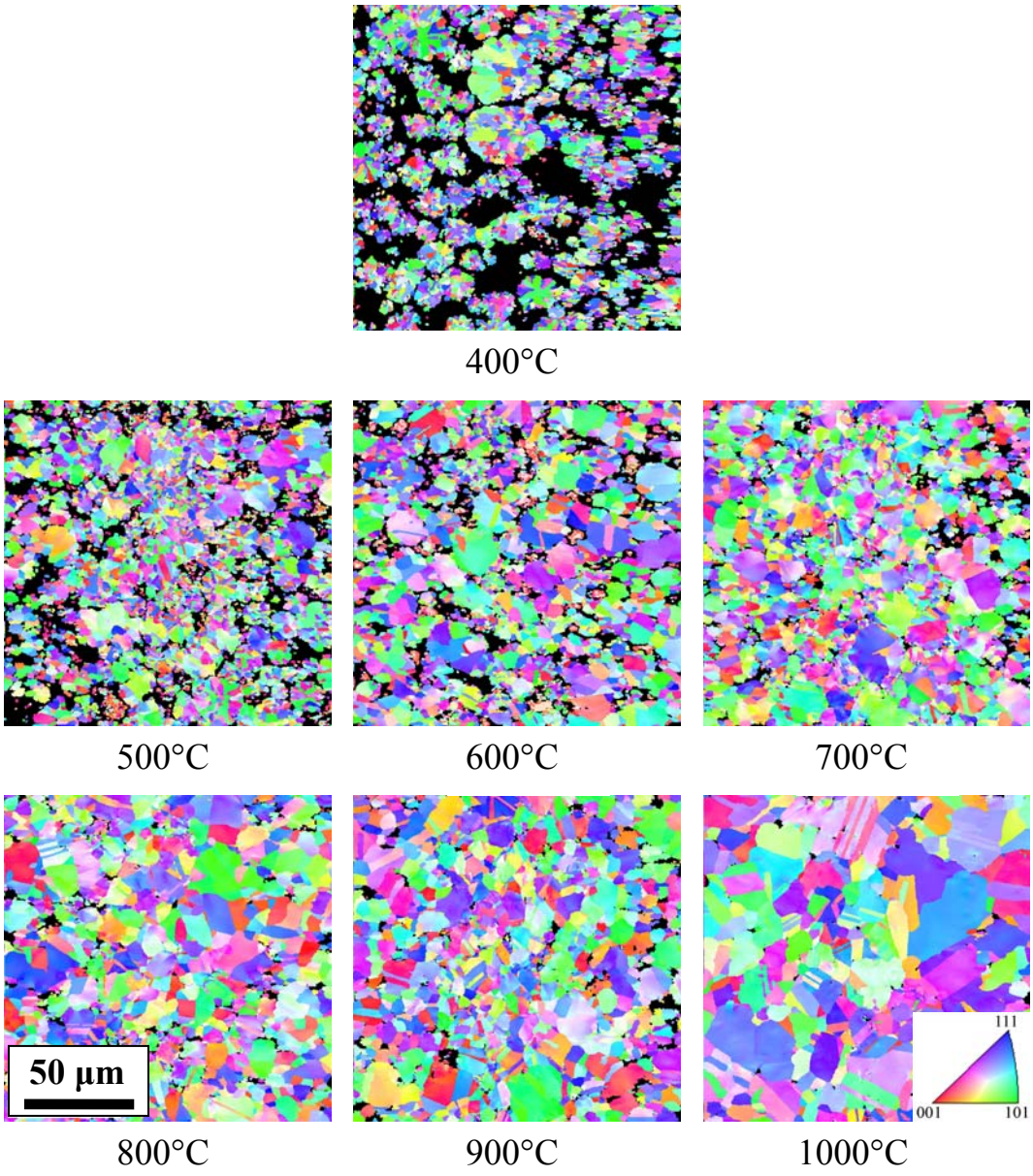

Figure 4.33. Orientation maps of SPS nickel processed from 400 to 1000°C at 61.9 MPa with no dwell. The scale bar is the same for all the figures. Black areas are pores. The colors correspond to particular orientations according to the legend.

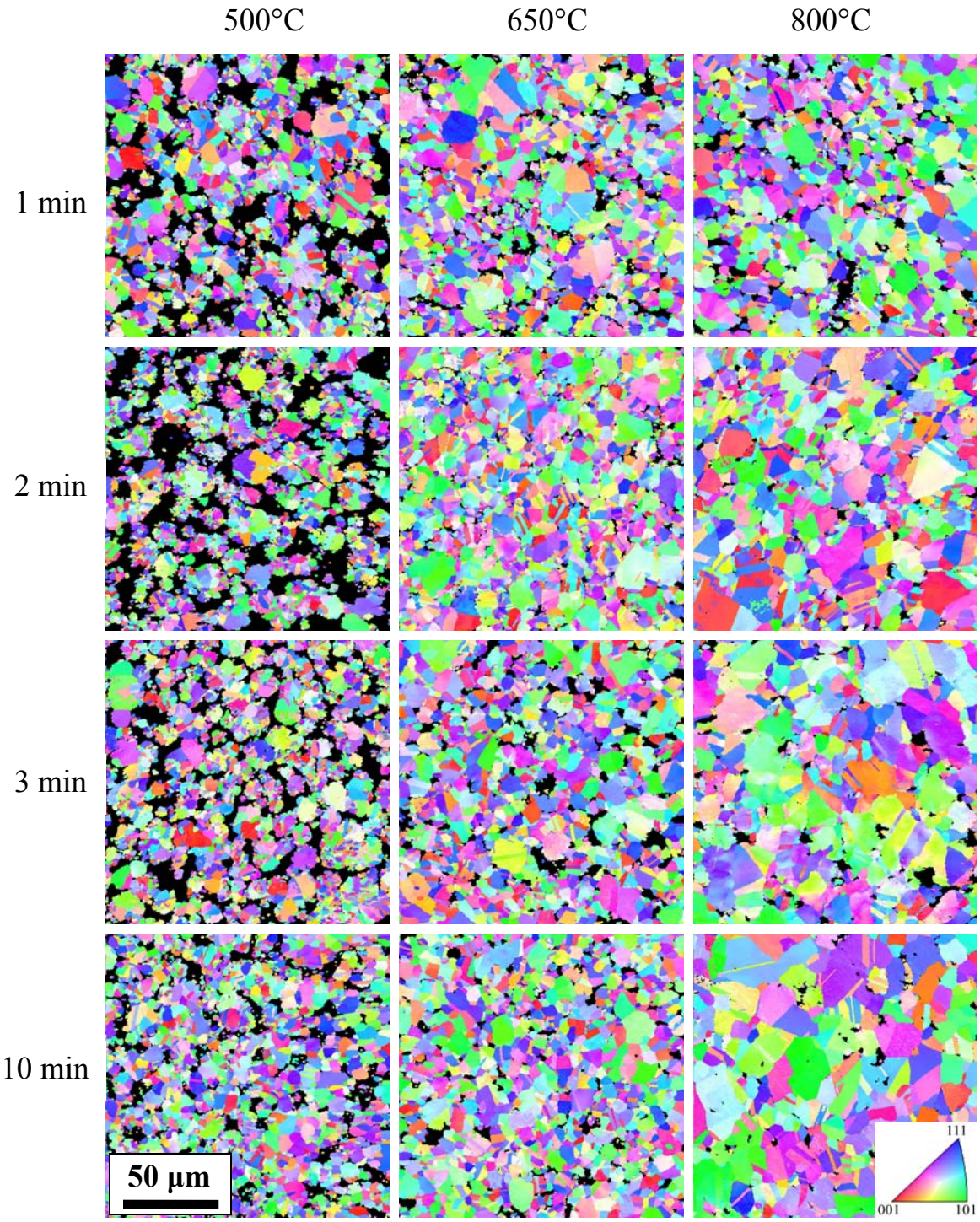

Figure 4.34. Orientation maps of SPS nickel processed from 500 to 800°C at 61.9 MPa with dwell times of 1 to 10 min. The scale bar is the same for all the figures. Black areas are pores. The colors correspond to particular orientations according to the legend.

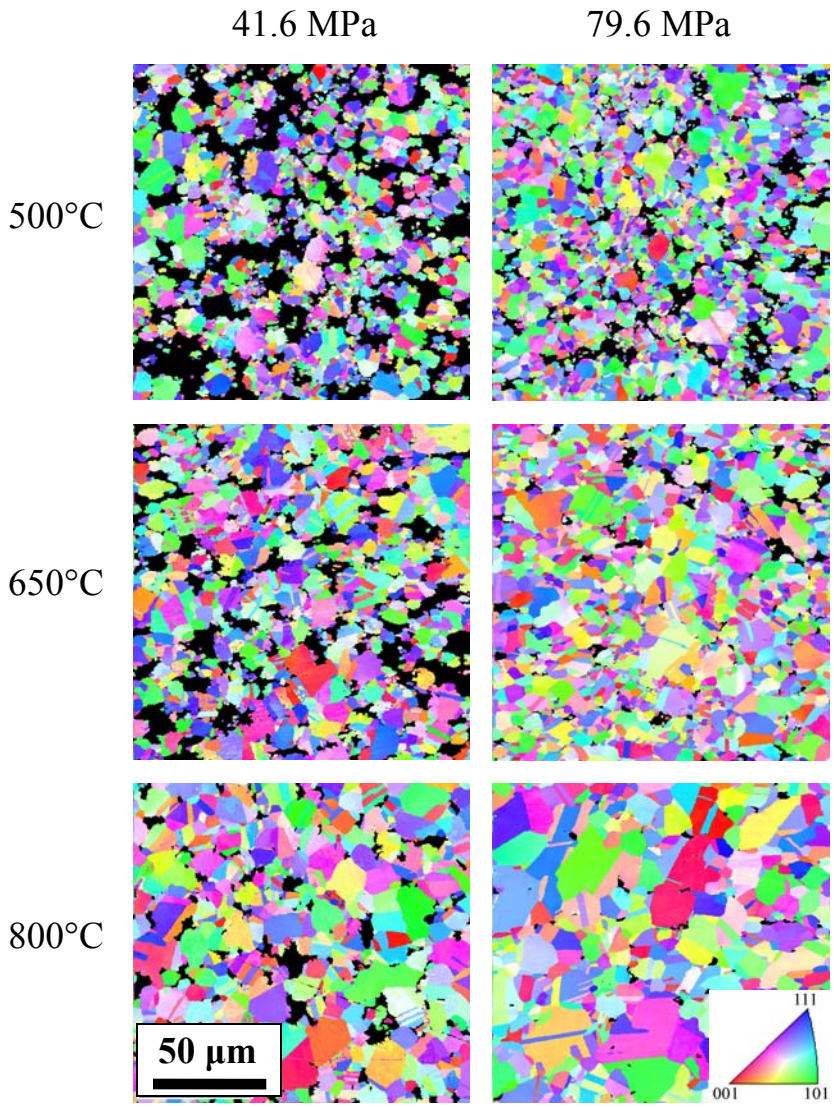

Figure 4.35. Orientation maps of SPS nickel processed from 500 to 800°C for 3 min at 41.6 and 79.6 MPa. The scale bar is the same for all the figures. Black areas are pores. The colors correspond to particular orientations according to the legend.

4.9.2: Microstructural Evolution of CS Nickel

The orientation maps for the CS nickel are shown in Figure 4.36 At 900°C there is no obvious change in microstructure as the dwell time increases, but at 1100 and 1300°C, the grains become noticeably larger with increasing dwell time and the porosity

appears to change from many smaller pores to fewer large pores. Porosity is also mainly located on the grain boundaries for all process conditions, except at 1300°C, 2 h where pores are also found inside grains.

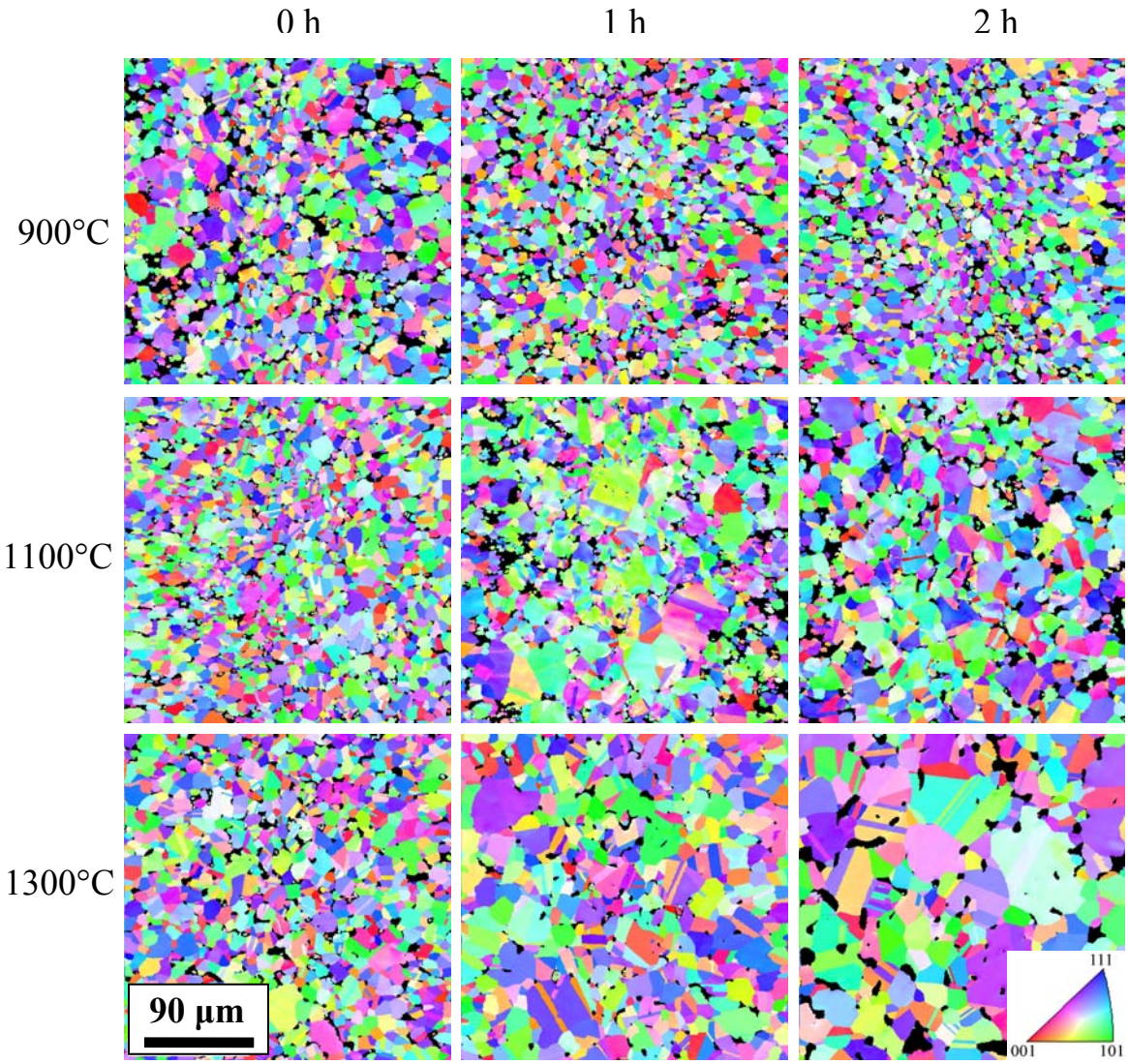

Figure 4.36. Orientation maps of CS nickel. The scale bar is the same in all figures. Black areas are pores. The colors correspond to particular orientations according to the legend.

CHAPTER 5: DISCUSSION

5.1: Density and Densification

In this section the density and densification of SPS and CS nickel will be compared. A discussion of the effects of the different SPS and CS process parameters on final density will also be presented. Using the displacement data collected during SPS processing, the densification during the SPS process can be analyzed.

The first comparison that can be made between SPS and CS nickel is in the range of final density. Figure 5.1 shows the density of SPS nickel samples processed from 400 to 1000°C with no dwell, along with the CS samples processed for 1 h, as a function of temperature. The effect of temperature on density of both SPS and CS nickel is apparent. However, the SPS process allows for a much wider range of densities at temperatures that are nominally below those required for CS processing. With SPS, the same density can be achieved at 800°C, with no dwell time, that is achieved after an hour at 1300°C for conventional processing.

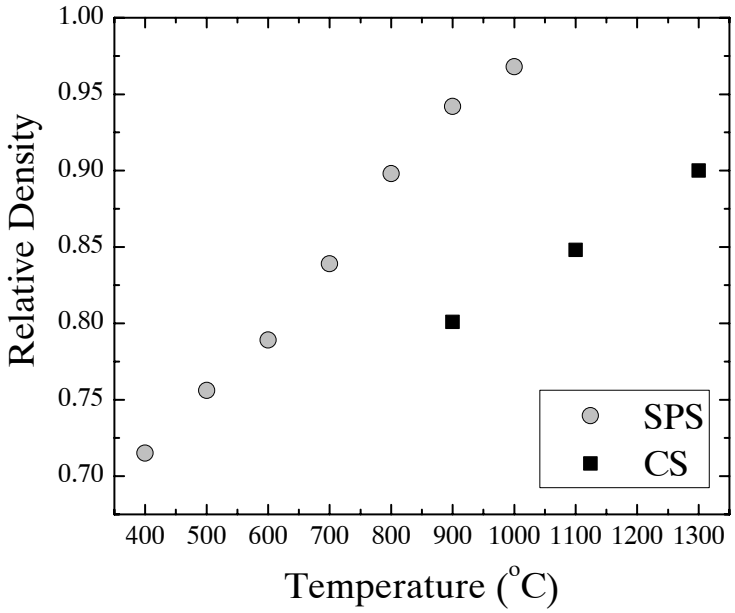

Figure 5.1. Comparison of density achieved during SPS and CS processing of nickel as a function of temperature. The SPS samples were processed with no dwell at 61.9 MPa, and the CS samples were sintered for 1 h.

The results of the different process parameters on the density of SPS nickel are shown in Figures 4.5 - 4.9. The effect of temperature on final density is stronger than any of the other process parameters. Increasing the temperature from 400 to 1000°C increases the final density from 72 – 97% theoretical. Increasing the dwell time from 0 to 10 min increases the density by only approximately 5% of the theoretical density at any temperature. The effect of pressure decreases with temperature, with an increase of approximately 10% at 500°C and 5% at 800°C. Different ramp rates do not appear to have an effect on the final density of SPS nickel.

During SPS processing, the machine continually records the position of the rams. That data can be converted into an instantaneous density to see how densification

proceeds during processing. In order to convert the data, the green-body density of a nickel pellet was determined. Five grams of nickel powder was manually pressed in the graphite die to 41.6 MPa for 2 min. The height of the green-body pellet and punches was measured and the height of the pellet was found to be 8.99 mm. Using the die geometry to calculate the volume of the green-body pellet, the green body density was found to be 55% theoretical density. For comparison, the smallest density that resulted from any SPS process condition was 70% theoretical density (400°C, 61.9 MPa, no dwell). Using the die geometry, and green body density, the displacement data was converted to instantaneous density. The instantaneous density as a function of time during SPS processing was plotted for the samples processed at 650°C, 61.9 MPa for 0 and 10 min in Figure 5.2. As the density was taken from the displacement data, the figures represent both the displacement and densification rates.

There are several points to note on Figure 5.2. There is no displacement up to approximately 1 min, at which point there is a sudden increase. Heating during SPS started from 0°C and so some time was required before the set point reaches a temperature high enough for the machine to begin a current flow. The punches heat very quickly during SPS and the thermal expansion is likely responsible for the discontinuities during the heating phase. Once the set temperature was reached, the displacement rate levels off to a value much slower that during the heating phase. This implies that the densification rate during the dwell phase is much slower than during the heating phase. This effect has been observed in the literature [37, 94], but is also evident from the comparison of density as a function of temperature and dwell time discussed previously. It is interesting to note that, after reaching the peak temperature, the displacement rate of

sample processed with no dwell is approximately the same as the sample that was held for 10 min at peak temperature. This is not expected, as the sample that was not held at temperature is cooling during this period. This phenomenon can be explained when the thermal expansion of the punches is considered. The punches cool very quickly once the current is shut off, and the shrinkage of the punches may offset the decreased densification during cooling. Both curves show a sudden drop in displacement towards the end of the process which corresponds to the decrease in pressure from 61.9 MPa, to the minimum of 41.6 MPa before the machine is shut off and the sample removed.

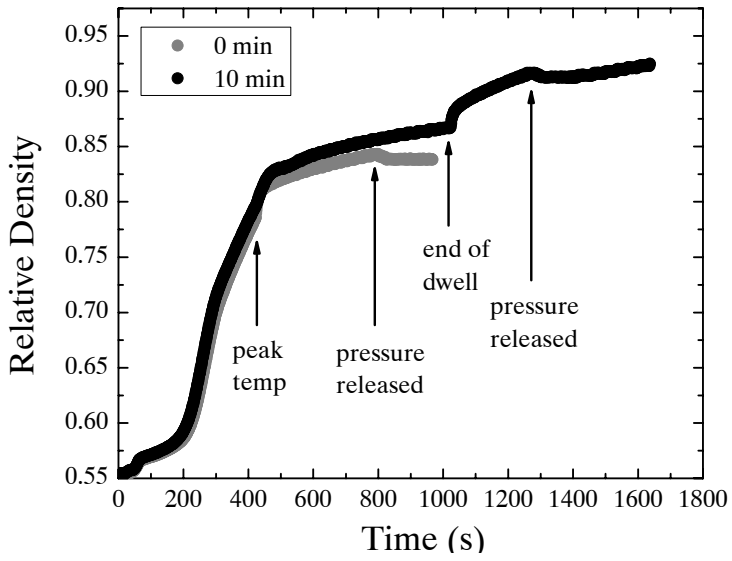

Figure 5.2. Instantaneous density during SPS processing of nickel. Samples were processed at 650°C for 0 and 10 min at 61.9 MPa. The different colors indicate the different dwell times.

The instantaneous density as a function of time for the samples processed at different ramp rates, up to the end of the dwell period, is shown in Figure 5.3. Each of these

samples ultimately reached a similar final density, but the densification rates were very different. The densification rate increased with the heating rate. However, the densification rate once the peak temperature was reached is nearly identical for the all the specimens, which is to be expected. A section of the curves is plotted in Figure 5.4 as density as a function of temperature. This shows that densification during SPS is thermally activated, and that densification of nickel begins at approximately 300°C. A similar result was also observed in SPS nickel nanopowder which began to densify at 230°C [12]. This is a very different result from the reported behavior of CS nickel [41]. In CS nickel, densification does not begin until around 600°C, when volume diffusion becomes dominant over surface diffusion [41]. However, with applied pressure, densification can begin by particle rearrangement and plastic flow [56, 57, 67].

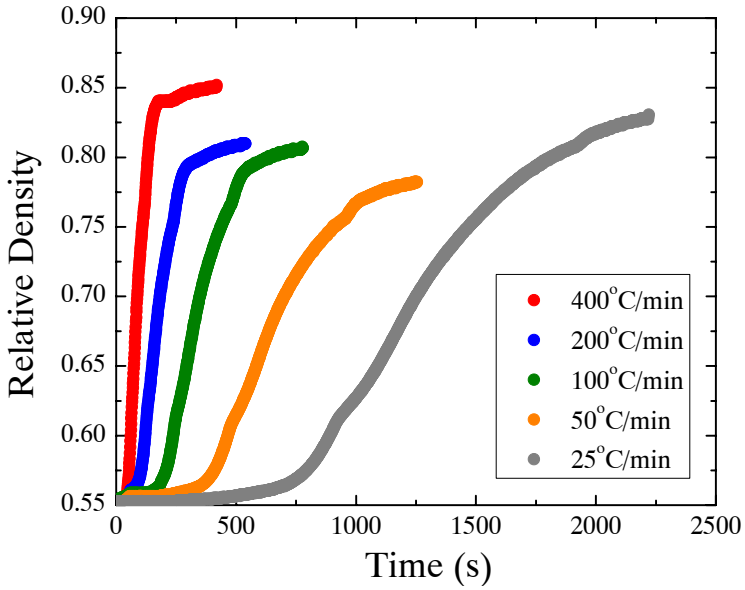

Figure 5.3. Instantaneous density during the heating and dwell phase of SPS nickel processed at different ramp rates to 800°C at 61.9 MPa. The different colors indicate the different ramp rates.

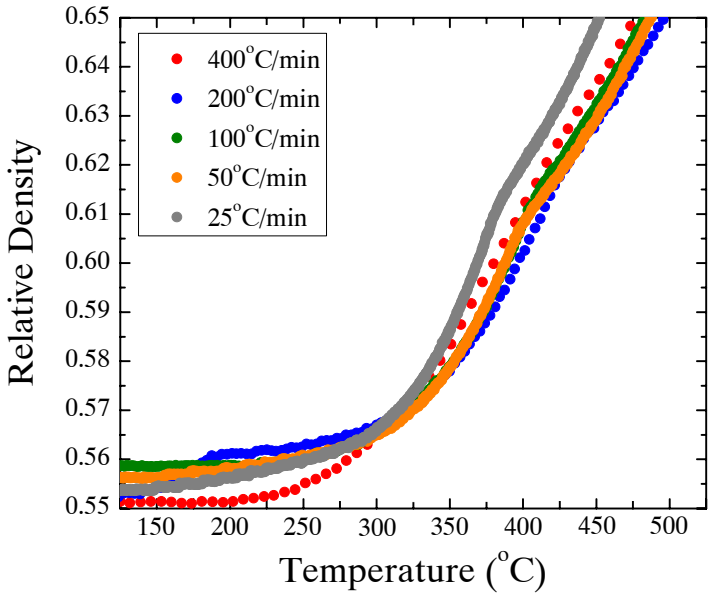

Figure 5.4. Instantaneous density as a function of temperature for the SPS nickel samples processed at different ramp rates to 800°C at 61.9 MPa. The different colors indicate the ramp rates.

The densification rate during heating appears to be constant, regardless of the final temperature, for the same heating rate. This can be seen by comparing the similar slopes of the lines in Figure 5.2 with the 100°C/min line in Figure 5.3, and also by the linear trend of density with temperature in Figure 4.9 where the heating rate was constant. A linear approximation of the densification curves for heating rates of 100°C/min (Figures 5.2 and 5.3) results in a value for the densification rate of 0.07-0.1% theoretical density per second (or 4-6% theoretical density per min). This value is much larger than the apparent densification rate during the heating phase for CS nickel. Given the heating rate of CS nickel, 5°C/min, and the final density of the specimens processed with no dwell, a rough approximation of the rate can be made. This approximation may be higher than the actual value, since the samples where in the furnace during heating and cooling,

and so the final density reflects more than just the heating phase. The green-body density of each CS nickel sample was measured before it was sintered, and the average was 71% theoretical density. The apparent densification rate is approximately 3.4% theoretical density per hour. This rate is much slower than the densification rate observed during processing with SPS.

Densification during the dwell in CS nickel is not significant. The density increases up to 1 h, but decreases at 2 h. Since the CS nickel was processed in Ar, the pores could contain trapped gas which prevents further densification. It is also possible that a gas is formed during processing; CO_2 can form as the oxygen released from the breakdown of NiO reacts with carbon present in the nickel [41]. However, the density change from 0 to 2 h is too small to draw any conclusions. Therefore, it is also difficult to draw any meaningful comparisons between the densification rate during the dwell phase of CS and SPS nickel beyond a qualitative comparison that densification during the dwell phase of SPS processing is greater than that during CS processing.

The consolidation of the powders into a sintered microstructure is also strongly temperature dependent. The difference in densification rates during heating and dwell can be observed in the microstructures of the final specimens. Densification during SPS appears to begin around 300°C, however the microstructure still resembles that of a powder until around 700°C (Figures 4.31 and 4.32). The samples processed at 500°C show clear particle boundaries under all conditions except at 10 min or at 71.6 MPa. However, even at those two conditions some previous particle boundaries are visible as defined by the pores. Alternatively, at 700°C with no dwell, or 650°C with a 2 min

dwell, the microstructures no longer resemble a powder compact except for the residual porosity.

5.2: Hardness

The plots of hardness as a function of grain size and density in Figures 4.13 and 4.15 show that, regardless of the processing method (SPS or CS), the hardness appears to increase with increasing grain size. Typically, hardness will increase with decreasing grain size [97]. The trend of increasing hardness with grain size can be explained by examining the effect of density on hardness. All of the points of hardness, grain size, and density, fall roughly on a line. As the density increases, so does the hardness and the grain size.

The effect of density on hardness was shown in Figures 4.12 and 4.14. The points are grouped by temperature showing the effect that temperature has on density, and, as a result, hardness. The hardness of both the SPS and CS samples as a function of density was found to be linear with the same slope and intercept. This is shown in Figure 5.5. Both processes result in samples that fall on the same hardness as a function of density line. A comparison can be made between the sintered nickel samples and foams as the porosity remaining in both the SPS and CS samples can simply be viewed as a particular foam-cell morphology. Hardness measurements are often used as an indication of the mechanical properties of a material [97]. It has been shown that the yield and compressive strength and elastic moduli of foams increase linearly with the relative density of the foam [103]. The force required to crush the cells in brittle foams using an indenter also increases linearly with relative hardness [103]. Hardness has also been

shown to increase with the packing-density of porous materials [93, 104], and increase linearly with density in thin films [105, 106]. No other mechanical testing was performed on any of the samples produced for this study, but it is reasonable to assume that other mechanical properties, like yield strength and fracture toughness, are also strongly dependent on density. It is also likely that, were samples to be produced at near theoretical density with a wider range of grain sizes, a dependence on grain size would be observed, as is seen in fully dense SPS processed copper, steel, and tantalum [3, 17, 37].

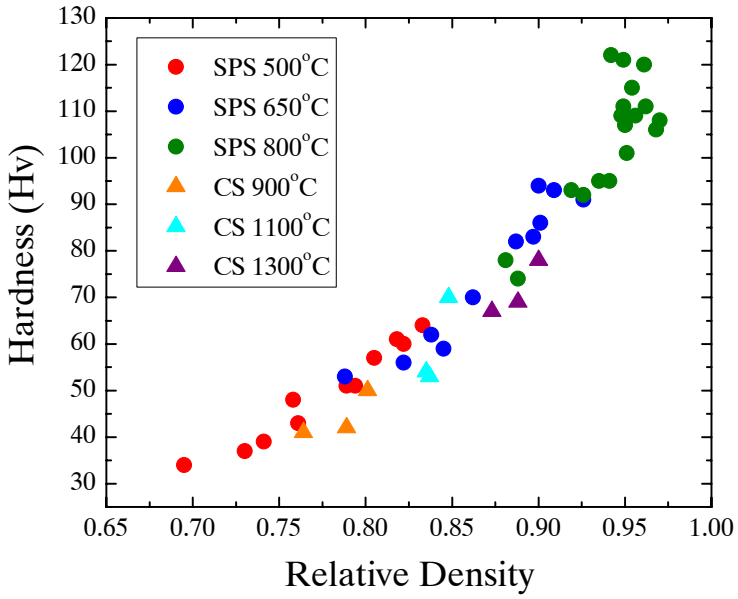

Figure 5.5. Hardness as a function of density for both the SPS and CS nickel samples. The colors indicate the different temperatures, and the symbols the different process techniques. The errors bars, shown in Figures 4.12 and 4.14, were not reproduced here.

5.3: Evidence of Temperature Gradients

The SPS process can create temperature gradients due to the fact that heat is produced by an applied current [21, 76, 78, 80, 81]. For conductive samples, the current

passes through the center of the sample, creating a radial temperature gradient with the hottest part of the sample in the center [21, 76, 78, 80, 81]. If the SPS process does create a radial temperature gradient during processing, then the porosity at the edge of the sample is expected to be higher because densification would be slower in the cooler region. A two-tailed, paired, student's t-test was done on the SPS porosity results which showed that the porosity at the center of the sample is statistically lower than at the edge with 99% confidence. Figure 4.16 has been recreated with the 95% confidence bands as shown in Figure 5.6.

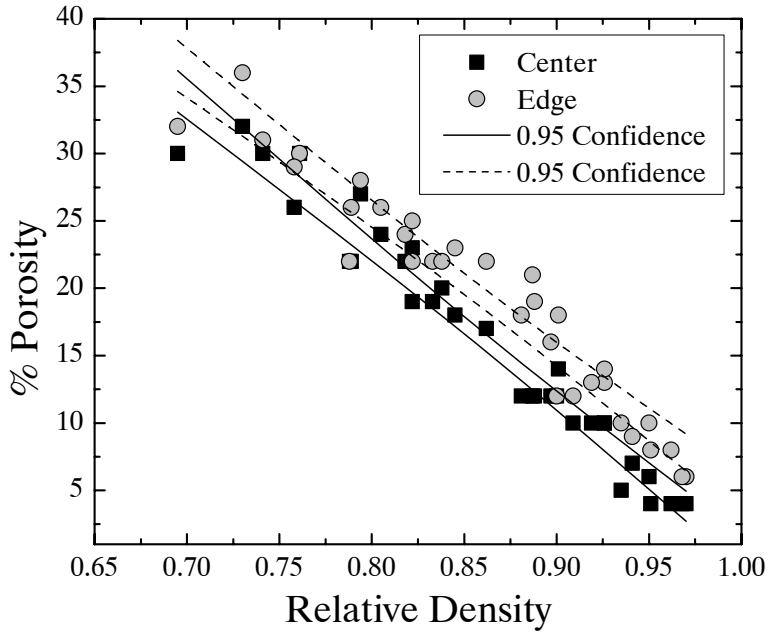

Figure 5.6. Porosity of all SPS nickel samples as a function of relative density. The black squares correspond to the measurements taken at the center, the gray dots to measurements taken at the edge of the samples, and the lines represent the 95% confidence bands for each sample set.

The linear fit lines in Figure 4.16 also indicate that the difference in porosity at the center and edge increases with increasing density. This can also be observed in Figure 5.6 by the overlap of the confidence bands at low density, and separation of the bands at high density. An increasing difference in porosity with density, which is primarily determined by temperature, indicates that temperature gradients increase with increasing temperature. This has also been found in SPS modeling studies [21, 76, 78, 80, 81]. Studies have shown that the difference between the center and the edge of the sample, and by extension the temperature of the sample and the measured temperature, increases with increasing temperature [21, 76, 78, 80, 81].

The total porosity fraction is expected to be one minus the fraction of theoretical density. Ideally, the porosity at the center would be lower than the total porosity, and the edge would be higher, but the porosity at both the center and edge is consistently higher than would be expected. This could mean that the measurement technique gives values that are uniformly higher than the true value, in addition to the estimated measurement error which shifts both curves upward. The optical micrograph in Figure 4.17 shows that porosity at the edge is primarily found in a small region at the approximate center of the sample height. The punches have been found to be the hottest part of die during SPS processing [21, 76, 78, 80, 81]. If the current flow also creates a radial temperature distribution, then the coolest part of the sample would be at the edge and approximately at the center, furthest away from the punches. Unfortunately, the error in the measurement of porosity is so large that is impossible to make any firm conclusions about porosity and temperature gradients.

Other evidence for temperature gradients can be inferred from the results of hardness and grain size. Of the samples that where the hardness was compared at the center and the edge, 3 showed that the hardness is statistically higher at the center, indicating that the center is more dense. The grain sizes at the center and the edge, shown in Figure 4.19, show an increasing separation towards higher densities, with the center of the samples having larger grains. It is very likely that the SPS process does produce temperature gradients in nickel. It is possible that with a larger different die geometry the gradients could shown more conclusively. Regardless, the temperature gradients can result in samples that have non-uniform properties, as was observed in ceramics [30, 76, 79].

5.4: Grain Growth During SPS

Spark plasma sintering is typically reported to produce dense structures with little grain growth [2, 3, 5, 12, 17, 18, 23, 29, 35, 37-40, 82, 93, 94]. Observation of the orientation maps in Figures 4.32 to 4.34 indicate that grain growth does occur during SPS. The grains in the initial nickel powder are small, and many grains are found inside each particle (Figure 4.4). However, even at the lowest process temperature, 400°C, some larger grains appear (Figure 4.32). While the microstructure still resembles a powder compact up to 700°C, the average grain size increases from that in the powder, 1.3 μm, to 1.8 at 400 and 500°C and 2 μm at 600°C. The grain growth inside the powder particles can also be seen in Figure 4.33 for the samples processed at 500°C. Powder boundaries are clearly visible up to 10 min, but the number of grains inside each particle has decreased significantly by the time the compact consolidates. At 600°C (Figure

4.32), many of the powders contain only one grain, or grain with twin boundaries. Figure 4.33 shows that for 650 and 800°C, many of the grains in the consolidated microstructures appear to be roughly the same size and shape as the powder particles. The average grain size does not accurately reflect this observation. A large enough number of small grains, perhaps many of them formed by twinning, keep the average grain size values small.

Grain growth has been shown to occur, but nothing yet has been said about the rate of grain growth. Calculating the grain growth exponent from Equation 2.8 can provide insight into the kinetics of grain growth during SPS. However, calculating the grain growth exponent proved very difficult. If the final grain size is much larger than the initial grain size, then Equation 2.8 can be reduced to [96, 98, 107, 108]:

$$G^g = Kt \tag{5.1}$$

Taking the natural log of both sides, and moving the exponent to the right-hand side results in [96]:

$$\ln G = \frac{1}{g}\ln t + \frac{1}{g}\ln K \tag{5.2}$$

By creating a log-log plot of grain size as a function of time, the grain growth exponent can be determined from the slope. Figure 5.7 shows the log-log plot of grain size as a function of time and the linear fit parameters. The corresponding values for *g* were found to be 27, 9.2, and 2.6 for 500, 650, and 800°C respectively.

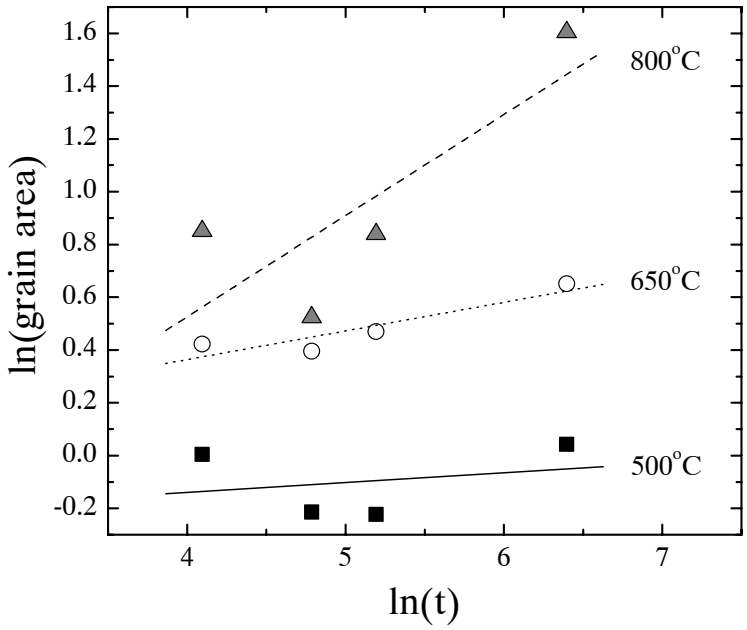

Figure 5.7. Log-log plot of average grain size as a function of time for SPS nickel processed at three different temperatures and 61.9 MPa. The symbols correspond to the different temperatures and the lines are linear fits.

A value of 2.6 for the grain growth exponent at 800°C may be realistic, as it is between the value for normal grain growth ($g = 2$) and grain growth in competition with densification ($g = 3$) [47, 49, 53, 56, 108]. The value at 800°C implies that the grain growth rate, determined by Equation 2.8, may actually be accelerated during SPS when compared to traditional sintering. Accelerated grain growth above a threshold temperature was found in copper [37]. The values of g at 500 and 650°C are too large to have much meaning.

Regardless, this method of finding g is only good as a first approximation for systems where grain growth is limited [98, 107, 108]. When the final grain size is not much larger than the initial grain size, the approximation in Equation 5.1 is not valid, and

a different approach must be employed [98, 108]. In order to determine the grain growth exponent, plots must be made where the grain size, raised to the exponent *g*, is plotted as function of time [98]. The intercept of a line fit to the data will equal the initial grain size, also raised to the exponent *g*, when the exact value of *g* is used [98]. Unfortunately, no value of *g* was found to precisely meet this criterion. The value of *g* that best meets the criterion is approximately 1. While the first approximation gave grain growth exponents that were large, a more careful analysis shows that grain growth of nickel during SPS is essentially linear with time at all temperatures. If the grain growth exponents are near unity, as indicated by the analysis outlined by Mistler, then grain growth rates during SPS are accelerated [98]. Some insight into the grain growth rates during SPS can be gained by comparing the grain growth as a function of time for SPS and CS nickel.

Grain growth rate approximations in SPS and CS nickel were found by fitting linear equations to the data for average grain size as a function of time. Figures 4.21 and 4.24 are recreated here as Figures 5.8 and 5.9 with the linear fit equations. A time of minutes was used for both the SPS and CS nickel for comparison. The CS data at 900°C was ignored because the slope appears to be negative, but the average grain size values cannot be differentiated due to the measurement error. While the actual grain size in CS nickel tends to be larger than in SPS nickel, the rate of grain growth in SPS nickel is higher than the rate in CS nickel. The rates of grain growth in CS nickel at 1100 and 1300°C are very close to the rates in SPS nickel at 500 and 650°C. It appears that the SPS process both enhances densification and grain growth. However, densification

during SPS occurs rapidly enough that fully dense specimens can be produced without a significant increase in grain size.

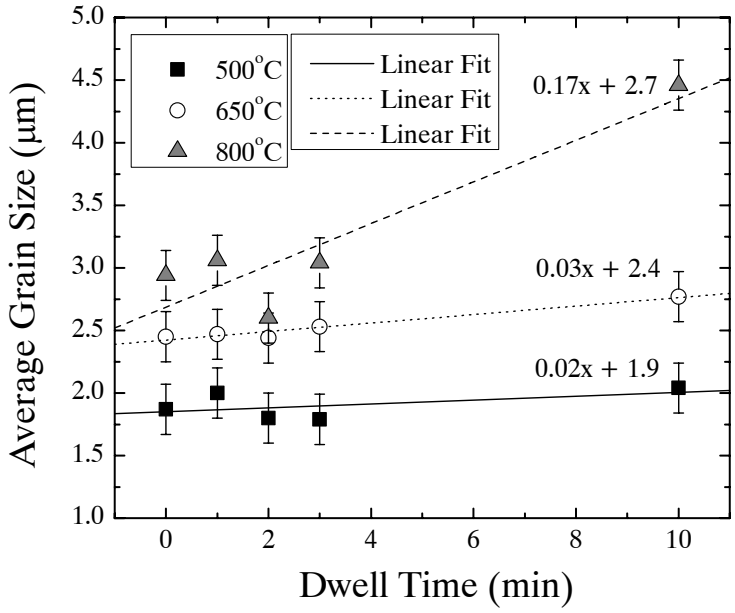

Figure 5.8. Grain size as a function of time for SPS nickel processed at three different temperatures and 61.9 MPa. The lines represent the linear fits to the grain size data.

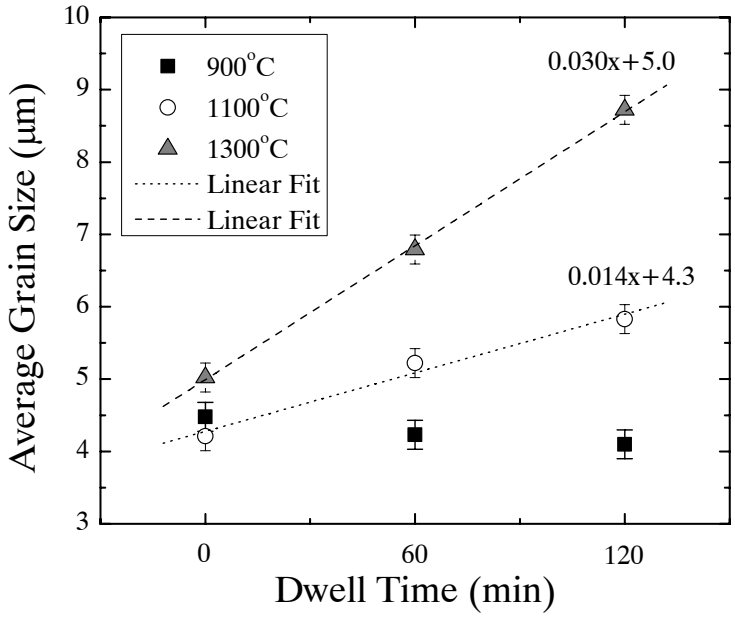

Figure 5.9. Grain size as a function of time for CS nickel. The lines represent the linear fit to the grain size data.

5.5: Grain Boundary Character Distribution

The grain boundary character distribution in SPS nickel does not change much with process conditions. In the powder, the Σ3 fraction was 34% and the special fraction was 55%. For SPS nickel, the Σ3 fraction remained near that value at all process conditions except at 800°C for 10 min and at 1000°C where the Σ3 fraction increased to around 50% in both cases. At 10 min, a temperature dependence is observed, with increasing Σ3 boundaries with increasing temperature. In SPS, 10 min may be long enough to be considered an annealing process. During annealing in nickel, the grain boundary energy is lowered by the formation of Σ3 boundaries [46, 47, 49, 54, 58]. The special fraction also remained near the powder value, though slightly lower possibly due to the creation of new general boundaries as particles are brought into contact, for all

process conditions except those that increased the Σ3 fraction. The special fraction appears to be primarily dependent on the fraction of Σ3 boundaries, as the special fraction is consistently higher by 15-20%. This is expected in nickel, as the Σ3 boundaries lower the grain boundary energy, but the other CSL boundaries do not have a significant effect on the grain boundary energy and are found in quantities to be expected from a collection of random misorientations [58].

In the CS nickel samples, similar trends were observed. The Σ3 boundary fraction remained near that of the initial powder except at 1300°C where the Σ3 fraction ranged from 40 to 50%. At a dwell time of 2 h, a temperature dependence was observed with increasing Σ3 fraction with increasing temperature. The Σ3 fraction increased from approximately 35 to 50% from 900 to 1300°C. This result is very different from a similar study performed on CS nickel [43]. For CS nickel processed at the same temperatures for 1 h, the Σ3 fraction was observed to increase from 15 to 43% [43]. No information on the starting characteristics of the nickel powder used in that study is given, so it is difficult to make a comparison. However, the final fraction of Σ3 boundaries in the study is in the same range as that observed in the CS nickel. In annealing studies, the fraction of Σ3 boundaries is found increase to around 40% and remain stable beyond that point [47, 49, 54]. The Σ3 fraction in the nickel powder began in that range, and so perhaps it is not surprising that the fraction does not change dramatically during either SPS or CS processing. It is possible that an initial powder with a lower Σ3 fraction, or a single-crystal powder may have produced very different results.

5.6: Evaluation of Sintering Mechanisms During SPS

This section will analyze some of the potential mechanisms that may be present during SPS [15, 84, 85, 88]. For CS processing of nickel, densification occurs by volume diffusion [41, 42, 55]. Attempts are made to calculate the activation energy of sintering by two different methods to determine the sintering mechanism in SPS. Plastic flow is analyzed, potential deformation mechanisms are identified, and the SPS data is fit to a hot-press model.

5.6.1: Activation Energy of Sintering

Although the experiments were not specifically designed to calculate the activation energy of sintering, the data do lend themselves to such analysis. Several different methods of calculating the activation energy of sintering exist [61, 63-65, 109-111], and two were used to calculate the apparent activation energy for spark plasma sintering of nickel [110, 111]. The first method calculates an activation energy from densification data obtained during processing at different ramp rates according to the equation:

$$\ln\left(T\frac{dT}{dt}\frac{d\rho_s}{dT}\right) = -\frac{Q}{RT} + \ln\left[f\left(\rho_s\right)\right] + \ln A - n\ln d \qquad (5.3)$$

where dT/dt is the heating rate, A is a material constant, and d is the size of the particles in the sintered compact [111]. Assuming that the particle size is only a function of density, then at a specific density the activation energy can be calculated from the slope of the line $\ln(T\,dT/dt\,d\rho_s/dT)$ as a function of $1/T$, where the slope is equal to $-Q/R$ [111]. The instantaneous density is plotted as a function of temperature during the heating phase for different ramp rates and the temperature and the slope of the curve at specific

densities are used to create the Arrhenius plot [111]. The displacement data was converted to instantaneous density by normalizing the data to the initial displacement and calculating a volumetric density from the die geometry and instantaneous powder compact height. The relative density is plotted as a function of temperature for the different ramp rates in Figure 5.10. As the 400, 200, 100, and 50°C/min datasets are essentially indistinguishable, only the 25 and 200°C/min were used in the calculation. Densities of 0.60, 0.65, and 0.70 theoretical were used, and the Arrhenius plot of these data is shown in Figure 5.11.

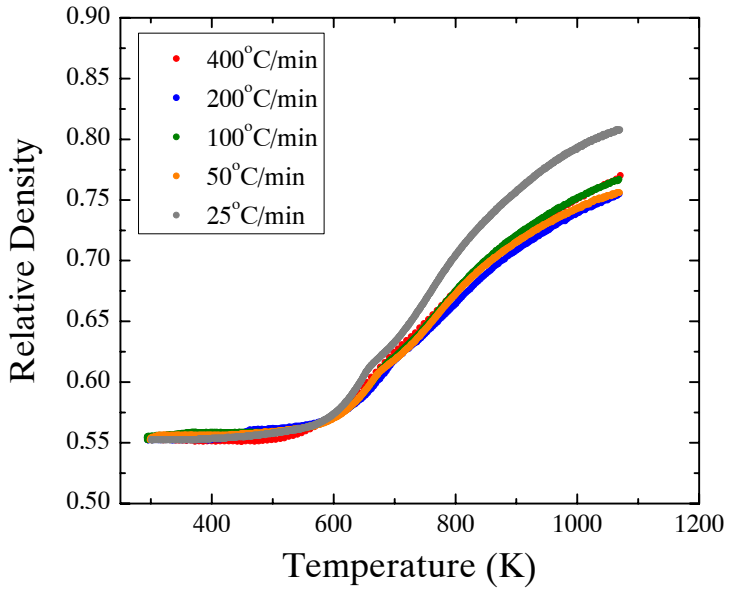

Figure 5.10. Plot of relative density as a function of temperature for SPS nickel processed at varying ramp rates to 800°C at 61.9 MPa. Only the data up to the dwell period is shown. Colors represent the different ramp rates.

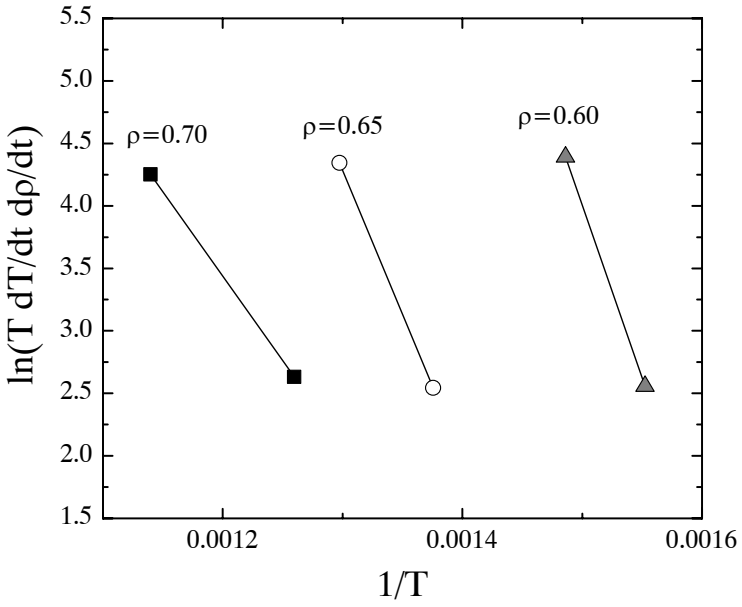

Figure 5.11. Arrhenius plot used to calculate the apparent activation energy of sintering for SPS nickel samples processed at varying ramp rates. Three curves are shown for specific densities from which the apparent activation energy was calculated.

The apparent activation energies of sintering, calculated using data from SPS nickel processed with different ramp rates, were found to be 230, 190, and 110 kJ/mol at densities of 0.6, 0.65, and 0.7 theoretical density. The apparent activation energy changes with density, which was also observed in CS processed alumina using this same method [111]. The authors suggested that at low density, densification only occurs by volume diffusion and that as the density increases, the other diffusion mechanisms, especially grain boundary diffusion, play a larger role in densification and their contribution is reflected by the decrease in activation energy [111].

The second method used to calculate the apparent activation energy of sintering was outlined by Parvatheeswara Rao *et al.* according to the equation:

$$\frac{1}{t} = K_0 e^{\frac{-Q}{RT}} \tag{5.4}$$

where K_0 is the rate constant [110]. The sintering time at specific densities is used to create a plot of ln(*1/t*) as a function of *1/T* from which the slope is used to calculate the activation energy [110]. As seen in Figure 4.6, the overlap of the isotherms as a function of time is very minimal, and where overlap is present, the data show a high degree of scatter. Therefore, the displacement data, converted into instantaneous density, was used for the calculations. The strong effect of temperature on density made it difficult to make meaningful comparisons for specific densities at all three temperatures. Activation energy calculations were made at densities of 0.80, 0.85, and 0.86 from the samples processed at 61.9 MPa for 10 min. It was impossible to use the same densities that were used for the first calculation. A plot of ln(*1/t*) as a function of *1/T* is shown in Figure 5.12. The activation energies were found to be 160, 150, and 140 kJ/mol at densities of 0.80, 0.85, and 0.86 theoretical density, respectively.

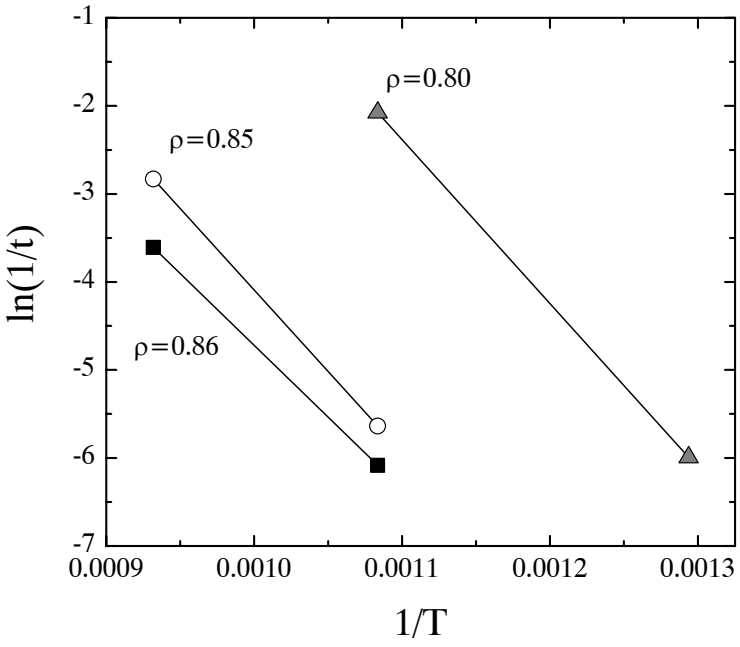

Figure 5.12. Arrhenius plot used to calculate the apparent activation energy of sintering for SPS nickel samples processed at 61.9 MPa for 10 min. Three curves are shown for specific densities from which the apparent activation energy was calculated.

The two different methods of calculating the apparent activation energy of sintering gave results in the range of the activation energies for diffusional processes, given in Table 2.3. The energies calculated from the ramp rate data range from 110 to 230 kJ/mol, and the energies calculated from the dwell time required to reach a common density ranged from 140 to 160 kJ/mol. The lowest of the values obtained from the ramp rate data is consistent with the activation energy for grain boundary diffusion while the highest approaches the value of volume diffusion [42, 55-57]. The mean of all the data falls near the value for surface diffusion. In CS nickel, surface diffusion is dominant at temperatures below 600°C, but does not lead to densification [41]. Volume diffusion, which becomes dominant above 600°C, is the mechanism by which CS nickel is reported

to densify [41]. The sintering mechanism of SPS nickel nanopowder was found to be grain boundary diffusion [12], and therefore it is possible that larger nickel powder sinters by the same mechanism, but is less likely.

The methods for calculating the apparent activation energy require many assumptions. The green body density is calculated geometrically assuming a consistent starting compact height and exact powder measurements. The methods employed also are attempting to calculate a value during intermediate stage sintering, which is the least understood and most difficult to model [56, 57, 67]. The activation energies do fall in the range of diffusional processes, however, given the potential inaccuracies in methods used to calculate the activation energy, no attempt to identify a specific mechanism will be made.

5.6.2: Plastic Flow

For pressure-assisted sintering, plastic flow is commonly the mechanism whereby initial densification occurs [56, 57]. Plastic flow will occur when the stress is above the yield strength [56, 57, 89, 97]. However, the yield strength of nickel changes with temperature, as is shown in Figure 5.13 from a National Bureau of Standards report on high-purity annealed nickel [112].

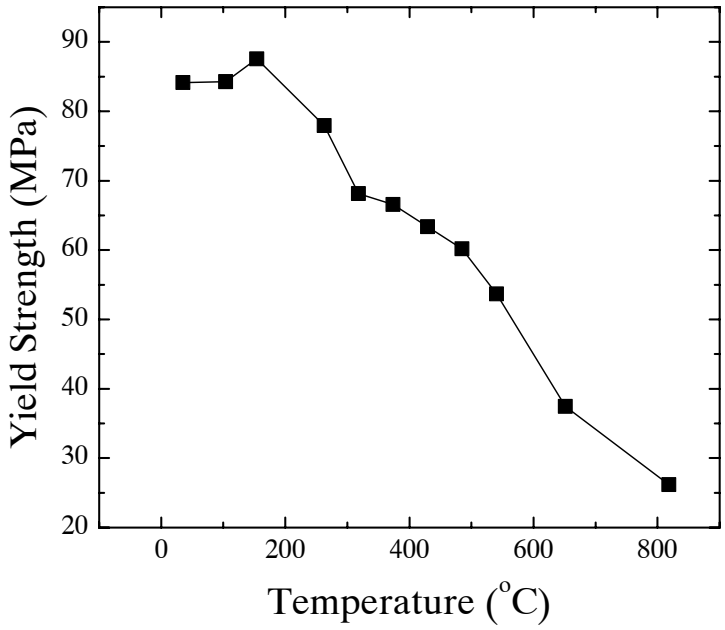

Figure 5.13. Yield strength of high-purity annealed nickel as a function of temperature, adapted from a report by the National Bureau of Standards [112]. The yield strength decreases with increasing temperature.

From the data in Figure 5.13, plastic flow is expected to occur at pressures above approximately 60 MPa at 500°C, above 38 MPa at 650°C, and above 27 MPa at 800°C. When the pressure enhancement due to smaller areas at particle contacts is also considered, then plastic flow is likely to occur at all temperatures in this study for pressures of 61.9 MPa and above, as well as all pressures in the study for temperatures above approximately 600°C.

Using Equations 2.11 and 2.12 for pressure-assisted sintering, the final density attainable by plastic flow can be easily estimated. Equation 2.11 should be valid for densities below 0.9, and Equation 2.12 for densities above 0.9. Using a green density of 0.55 and the yield strength extracted from Figure 5.13 for each temperature, the estimated

densities due to plastic flow were calculated. When the results from Equation 2.11 were greater than or equal to 0.9, Equation 2.12 was used in its place. The results of these calculations are given in Table 5.1, and for comparison, the highest densities attained during SPS processing.

Table 5.1. Estimates of the final density due to plastic flow for SPS nickel calculated from Equations 2.11 and 2.12. Estimates are compared to the highest density obtained during SPS of nickel. Process conditions with no data for calculations are left blank.

	Pressure (MPa)					
Temp	41.6		61.9		71.6	
(°C)	PF	SPS	PF	SPS	PF	SPS
400			0.79	0.715		
500	0.75	0.741	0.81	0.818	0.86	0.833
600			0.86	0.789		
650	0.82	0.845	0.90	0.926	0.96	0.909
700			0.95	0.839		
800	0.89	0.926	0.96	0.970	0.99	0.968
900				0.942		
1000				0.968		

*where PF is the estimate for plastic flow (Equations 2.11, 2.12) and SPS is the experimental result

By comparing the results for estimated density due to plastic flow and the actual densities obtained during SPS, it appears that nearly all the densification during SPS of nickel can be attributed to plastic flow. In many cases, the results of the density estimates for plastic flow exceeded that attained during actual processing. Plastic flow is reported to be a process which enhances pressure-assisted sintering initially, but decreases as

dislocations are annealed out of the structure, and as the particle contacts increase in size [56, 57]. If plastic flow were to be dominant throughout the SPS process, then it could be expected that the powder particles would deform in the direction of applied pressure, however, as the micrographs in Figures 4.32 to 4.34 show, the apparent particle boundaries remain roughly circular and the grains equiaxed regardless of time temperature, or pressure. Plastic flow may not be responsible for all of the densification observed during SPS.

5.6.3: Deformation Mechanism Map

The deformation mechanism maps, first shown in Figure 2.3, should give some insight into the densification mechanism during SPS as it is a pressure-assisted process and the deformation mechanisms may be active during processing [85, 88]. The map is plotted as shear strength as a function of temperature. The ratio of radial pressure to axial pressure, which German terms an "effective shear," is approximately 0.3 for the pressures used in this study [57]. That ratio means that the SPS process parameters will fall approximately along a line at 10 MPa on Figure 2.3. Figure 5.14 shows the maps with the region that applies to the SPS process conditions highlighted.

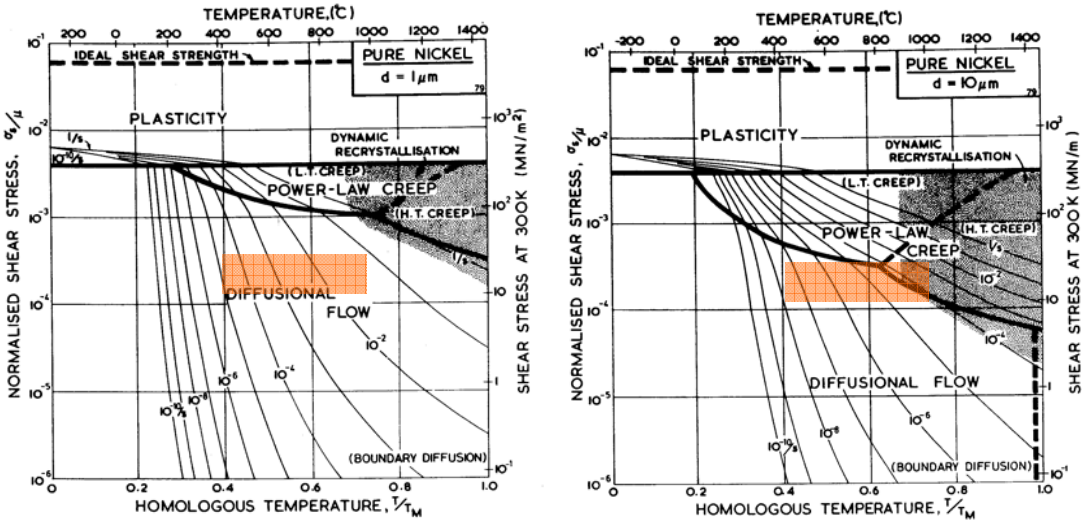

Figure 5.14. Deformation mechanism maps for nickel with grain sizes of 1 and 10 μm [89]. Images taken from the online version of the Frost and Ashby text, available at: http://engineering.dartmouth.edu/defmech/. The highlighted areas show the regions that correspond to the range of SPS process conditions used in this study.

With 1 μm grains, regardless of the temperature, the expected deformation mechanism is diffusional flow by grain boundary diffusion. However, for grains at 10 μm, the process conditions could also allow for power law creep. Volume diffusion, which is dominant during conventional sintering of nickel [41], may not be dominant during SPS as the deformation mechanism map indicates that the primary diffusional process is grain boundary diffusion [89]. Judging by only the average grain size, the map for 1 μm grains would apply. However, the grains sizes in SPS do have wide distributions with many process conditions producing samples that do have grains of 10 μm or larger. Therefore power law creep may play a significant role during SPS, as has also been postulated in the literature [84, 85, 88]. In modeling of SPS processed

aluminum, power-law creep was the dominant mechanism for densities up to 90% with grain sizes above 1 μm [84].

Most of the samples processed with SPS had similar microstructures. However, the sample processed at 1000°C did not follow the trend for grain size, fraction of Σ3 boundaries, or show similar appearance to other samples by viewing the inverse pole figure. The differences may be due to a change in mechanism around 1000°C. As the deformation mechanism map for 10 μm grains shows, the sample processed at 1000°C should be dominated by power law creep. This potential change in mechanism could explain the changes in microstructure observed at 1000°C.

5.6.4: Hot Press Modeling

As the SPS process is similar to hot pressing, and to potentially determine the mechanisms of sintering and grain growth during SPS, the data was fit to the hot press model in Equation 2.16. Hot press models have been applied to SPS to create densification maps [113, 114]. Unfortunately, many models use different terminology than that used in this study. In this study, a grain is defined as a particular crystallographic orientation [1], and many grains can be seen in the polycrystalline nickel powder (Figure 4.4). However, in the sintering and hot-press models, this definition of a grain is often called a crystallite and the powder particles are referred to as grains [60, 61, 64, 67]. For the modeling done in this study, the crystallographic definition of a grain was used, and the differences between grains and particles at the different modeling stages can be seen in Figure 4.34. Both the polycrystalline powder and the nature of the SPS process make modeling a complex task. Despite the complexity inherent to this SPS

study, a fit of the densification data to a hot-press model may provide insight into the differences between hot-pressing and spark plasma sintering.

Assuming that the pores are spherical, Equation 2.16 becomes:

$$\frac{1}{\rho}\frac{d\rho_s}{dt} = \frac{HD\left(\frac{1}{\rho(t)}\right)^q}{G(t)^g kT} P_A{}^q \tag{5.5}$$

where ρ_s is the fractional density, t is time, H is a collection of constants relating to the deformation mechanism, D is the diffusivity coefficient determined by the dominant mechanism, G is the grain size, k is Boltzmann's constant, T is temperature, P_A is the applied pressure, q is the pressure exponent, and g is the grain growth exponent [67]. The displacement data during the dwell, converted to instantaneous density, from the samples processed at 61.9 MPa for 10 min, during the dwell, were fit to the model and the exponents q and g were calculated. The data during the dwell was used because grain size data during the heating phase is unavailable. The left hand term in equation 5.5 was found by multiplying the inverse of the density by the instantaneous change in density at each point during the dwell. The instantaneous density was calculated by finding the slope of the secant line that intersected the density curve 3 s before and 3 s after the point in question. The time dependent grain size term in Equation 5.5 was the same as was used to determine the apparent grain growth rate determined previously. To use the grain size data in this manner assumes that the grains did not grow after the end of the dwell period. This is reasonable to assume as the cooling rate in SPS is very fast. The fit of linear equations to the grain size data was shown in Figure 5.8. To find the time dependent equation for density on the right-hand side, a linear equation was fit to the instantaneous density data, shown in Figure 5.15. The density data for the period after

the rate had stabilized from the heating phase was used. Finally, the coefficient *HD* and exponents *q* and *g* were found by using the FindFit routine in Mathematica version 7 at each temperature. The results for *HD*, *q*, and *g* are given in Table 5.2.

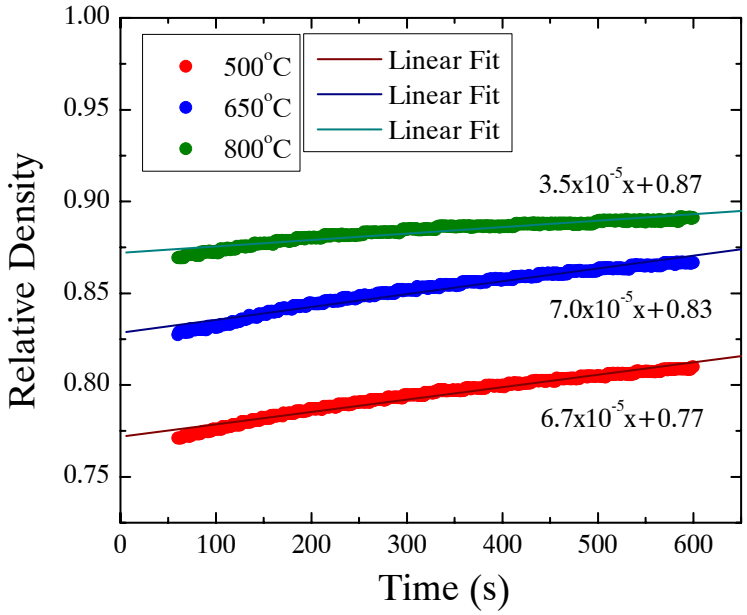

Figure 5.15. Density as a function of time during the dwell period of SPS nickel processed at three different temperatures at 61.9 MPa for 10 min. The data during the transition from the heating phase to the dwell phase, where the densification rate changed, was excluded.

Table 5.2. Results for *HD*, *q*, and *g* from the fit to the hot-pressing model in Equation 5.5.

Temp (°C)	HD	q	g
500	2.1	1.1	-0.6
650	2.1	1.1	-0.1
800	2.1	1.1	0.1

The value for *HD* does not change with temperature, which means that either the diffusivity constant does not change with temperature, or that the constant *H* changes to counteract a change in *D*. However, since neither *q* nor *g* change significantly with temperature, it is likely that *D* does not change, which implies that the dominant mechanism is the same at all three temperatures. The value for *q* is 1.1 regardless of temperature. The value for *g* does increase slightly with temperature, but is always near zero. According to Table 2.2, values for *q* and *g* of 0 and 1, respectively, means that densification is primarily controlled by viscous flow [67]. Viscous flow is more common in materials with glassy phases than in metals [56, 64]. Both viscous flow and plastic flow are the deformation of a material under stress at high temperature, the first due to a decrease in viscosity and the other to a decrease in yield strength [56, 64]. As has already been shown, plastic flow may be responsible for a considerable portion of densification. However, the values of the exponents that result from this hot press model should distinguish between viscous and plastic flow (Table 2.2) [67]. The pressure exponent is not high enough to indicate that plastic flow is dominant [67]. For the model to indicate that diffusional processes are dominant, a significant change in grain size must be present. The model only has two terms to account for densification, pressure and grain growth. As grain growth is small, an increase in the densification rate may lead to an increase in the resultant pressure exponent, which would indicate plastic flow. The density data during the dwell was used where the densification rate is much slower than during the dwell. It is possible that, had the model been used to fit the data during the ramp rate (making assumptions for temperature and grain size), the result might have indicated plastic flow.

Given that the change in grain size during SPS of nickel is very small, it is not surprising that the model does not indicate that diffusional processes are dominant. Rahaman indicates that the hot press model has difficulty when more than one mechanism is operating [67], and Olevsky *et al.* state that hot press models cannot accurately explain how densification is enhanced during SPS, nor provide new insight into the dominant mechanism [84, 85, 88]. Therefore, it is likely that different models must be developed and applied to SPS [84, 85, 88].

5.6.5: Discussion of the Sintering Mechanism of Nickel in SPS

The hot press model resulted in a grain growth exponent that was very near zero, implying that diffusion is not dominant. Rather, the hot press model indicates that viscous flow is dominant during SPS of nickel. Yet, the activation energy and probable location of the process conditions on a deformation mechanism map indicate that diffusional processes are in fact dominant [57, 89]. Further, estimates of the contribution due to plastic flow indicate that densification could be entirely attributed to that process. The seemingly conflicting results are likely indicative of the inadequacy of the existing sintering models to completely explain SPS. Multiple mechanisms can be active during SPS, and all the mechanisms may contribute to densification [15, 41, 56, 57, 84, 85, 88]. Densification of nickel during SPS likely has contributions from plastic flow, diffusional processes, and power law creep, along with mechanisms inherent to sintering with an electric field such as electromigration.

CHAPTER 6: CONCLUSIONS

A study of the microstructural evolution of nickel during spark plasma sintering was presented to better understand the effects of SPS process parameters on microstructure. A comparison was made to the microstructure of conventionally sintered nickel. Specimens of nickel were produced at varying temperature, dwell time, applied pressure, and ramp rate using SPS, and at varying temperature and dwell time for conventional sintering. The properties and microstructure were investigated to determine the density, hardness, porosity, grain size, and grain boundary character for specimens using both processing techniques. The microstructural evolution was found to be very different during SPS and CS processing. The data from the SPS processing was used to calculate the activation energy of sintering and the data was fit to a hot-press model to try and determine the dominant mechanism of densification of SPS nickel. The following are the key results of this study:

- Nickel specimens were produced using SPS from 70 -97% theoretical density. Nickel specimens produced by SPS reach higher densities at lower temperatures and in shorter time than specimens produced by CS techniques.
- Temperature is the most important SPS process parameter in determining the final density of SPS nickel. The rate of densification during heating is dramatically greater than the rate during the isothermal dwell of SPS processing.

- The hardness of SPS and CS specimens is linearly related to the final density and not to the grain size. This relationship is consistent with properties observed in foams.
- Some evidence of radial temperature gradients was observed in the SPS specimens. In a few samples the hardness was statistically higher at the center of the sample, and the porosity was found to be statistically lower at the center than at the edge.
- The average grain size is roughly linear with time and temperature at temperatures below 1000°C. The grain growth rates in SPS nickel were higher than those in CS nickel. Grain growth occurs in the powders first, but little occurs after densification below 1000°C, consistent with results from studies on pure copper.
- The grain boundary character was stable at all CS processing conditions, remaining near the values found in the original powder, except at the highest temperatures and longest dwell times, where an increase in the Σ3 and special fraction was observed.
- Several mechanisms may be responsible for intermediate stage densification during SPS. Values of the activation energy of sintering were lower than expected for volume diffusion, the dominant mechanism in CS processing, but still in the range of diffusion processes. Plastic flow is also expected to have a strong contribution to the final density. At 1000°C, there is a possible change in mechanism from diffusional processes to power law creep, which could explain the differences observed the microstructure at that temperature. However, no conclusions can be made about specific mechanisms.
- A hot-press model, which was used to determine the densification mechanism, gave results inconsistent with traditional metal densification mechanisms. The current hot-press models are likely inadequate for modeling SPS.

REFERENCES

1. Callister, W.D., *Materials Science and Engineering: An Introduction*. 6 ed. 2003, Hoboken: John Wiley & Sons.

2. Anderson, K.R., et al., *Surface oxide debonding in field assisted powder sintering.* Materials Science & Engineering A, 1999. **270**(2): p. 278-282.

3. Angerer, P., et al., *Texture and structure evolution of tantalum powder samples during spark-plasma-sintering (SPS) and conventional hot-pressing.* International Journal of Refractory Metals and Hard Materials, 2007. **25**(4): p. 280-285.

4. Boesel, R.W., M.I. Jacobson, and I.S. Yoshioka, *Spark Sintering Tames Exotic P/M Materials.* Materials Engineering, 1969. **70**(4): p. 32-35.

5. Chae, J.H., et al., *Microstructural evolution of Al2O3-SiC nanocomposites during spark plasma sintering.* Journal of Alloys and Compounds, 2006. **413**(1-2): p. 259-264.

6. Choi, P.P., et al., *Al-La-Ni-Fe bulk metallic glasses produced by mechanical alloying and spark-plasma sintering.* Materials Science and Engineering A, 2007. **449-451**: p. 1119-1122.

7. Feng, K., et al., *Intensified sintering of iron powders under the action of an electric field: Effect of technologic parameter on sintering densification.* Journal of Materials Processing Technology, 2008. **208**(1-3): p. 264-269.

8. Friedman, J.R., et al., *Modified interfacial reactions in Ag-Zn multilayers under the influence of high DC currents.* Intermetallics, 2004. **12**(6): p. 589-597.

9. Goetzel, C.G. and V.S. De Marchi, *Electrically Activated Pressure Sintering (Spark Sintering) of Titanium Powders.* Powder Metallurgy International, 1971. **3**(2): p. 80-87.

10. Groza, J.R., *Field-Activated Sintering*, in *ASM Handbook*. 1998, ASM International. p. 583-589.

11. Hulbert, D.M., et al., *Experiments and modeling of spark plasma sintered, functionally graded boron carbide–aluminum composites.* Materials Science and Engineering A, 2008. **488**: p. 333-338.

12. Kodash, V.Y., et al., *Field-assisted sintering of Ni nanopowders.* Materials Science and Engineering A, 2004(385): p. 367-371.

13. Kubota, M. and B.P. Wynne, *Electron backscattering diffraction analysis of mechanically milled and spark plasma sintered pure aluminium.* Scripta Materialia, 2007. **57**(8): p. 719-722.

14. Locci, A.M., et al., *Mechanical and electric current activation of solid–solid reactions for the synthesis of fully dense advanced materials.* Chemical Engineering Science, 2007. **62**: p. 4885-4890.

15. Munir, Z.A. and U. Anselmi-Tamburini, *The effect of electric field and pressure on the synthesis and consolidation of materials: A review of the spark plasma sintering method.* Journal of Materials Science, 2006. **41**: p. 763-777.

16. Newman, D.C., *Novel uses of electric fields and electric currents in powder metal (P/M) processing.* Materials Science and Engineering A, 2000. **287**(2): p. 198-204.

17. Ni, H.W., et al., *Preparaion of Nanocrystalline 430L Stainless Steel by HEBM and SPS.* Journal of Iron and Steel Research, 2008. **15**(4): p. 73-76.

18. Nygren, M. and Z. Shen, *On the preparation of bio-, nano- and structural ceramics and composites by spark plasma sintering.* Solid State Sciences, 2003. **5**: p. 125-131.

19. Orrù, R., et al., *Consolidation/synthesis of materials by electric current activated/assisted sintering.* Materials Science and Engineering: R: Reports, 2009. **63**(4-6): p. 127-287.

20. Raichenko, A.I., et al., *Electric Discharge Sintering of Binary Powder Mixtures.* Soviet Powder Metallurgy and Metal Ceramics, 1976. **15**(8): p. 602-606.

21. Räthel, J., M. Herrmann, and W. Beckert, *Temperature distribution for electrically conductive and non-conductive materials during Field Assisted Sintering (FAST).* Journal of the European Ceramic Society, 2009. **29**: p. 1419-1425.

22. Roy, D., et al., *Microstructure and mechanical properties of mechanically alloyed and spark plasma sintered amorphous-nanocrystalline Al65Cu20Ti15 intermetallic matrix composite reinforced with TiO2 nanoparticles.* Intermetallics, 2007. **15**: p. 1595-1605.

23. Sakamoto, T., *Sintering Behavior of Mo Powder Compact Applied SPS Spark Plasma Sintering Method.* Journal of the Japan Society of Powder Metallurgy, 1997. **44**(9): p. 845-850.

24. Sasaki, T.T., et al., *Bulk nanocrystalline Al85Ni10La5 alloy fabricated by spark plasma sintering of atomized amorphous powders.* Materials Science & Engineering A, 2007.

25. Schneider, J.A., et al., *Mechanisms of plasma assisted sintering in the Si3N4 ceramic system.* Materials Letters, 1995. **25**(3-4): p. 101-104.

26. Shen, Z. and M. Nygren, *Microstructural Prototyping of Ceramics by Kinetic Engineering: Applications of Spark Plasma Sintering.* The Chemical Record, 2005. **5**(3): p. 173-184.

27. Song, X., X. Liu, and J. Zhang, *Neck Formation and Self-Adjusting Mechanism of Neck Growth of Conducting Powders in Spark Plasma Sintering.* Journal of the American Ceramics Society, 2006. **82**(2): p. 494-500.

28. Tokita, M., *Development of Large-Size Ceramic/Metal Bulk FGM Fabricated by Spark Plasma Sintering.* Materials Science Forum, 1999. **308-311**: p. 83-88.

29. Trunec, M., K. Maca, and Z. Shen, *Warm pressing of zirconia nanoparticles by the spark plasma sintering technique.* Scripta Materialia, 2008. **59**(1): p. 23-26.

30. Vanmeensel, K., et al., *Field assisted sintering of electro-conductive ZrO2-based composites.* Journal of the European Ceramic Society, 2007. **27**(2-3): p. 979-985.

31. Wang, S.W., et al., *Effect of plasma activated sintering (PAS) parameters on densification of copper powder.* Materials Research Bulletin, 2000. **35**: p. 619-628.

32. Wang, Y.H., et al., *Microstructures and mechanical properties of Ti-45Al-8.5Nb-(W,B,Y) alloy by SPS-HIP route.* Materials Science and Engineering: A, 2008. **489**(1-2): p. 55-61.

33. Wu, W.W., et al., *Synthesis and microstructural features of ZrB2–SiC-based composites by reactive spark plasma sintering and reactive hot pressing.* Scripta Materialia, 2007. **57**: p. 317-320.

34. Xie, G., et al., *Reduction mechanism of surface oxide films and characterization of formations on pulse electric-current sintered Al–Mg alloy powders.* Applied Surface Science, 2005. **241**: p. 102-106.

35. Yoo, S.H., et al., *Consolidation and High Strain Rate Mechanical Behavior of Nanocrystalline Tantalum Powder.* NanoStructured Materials, 1999. **12**: p. 23-28.

36. Yun, K.S., J.H. Lee, and C.W. Won, *Effect of current application methods on the preparation of Fe–Al intermetallic compounds by field-activated combustion synthesis.* Materials Research Bulletin, 2000. **35**: p. 1709-1716.

37. Zhang, Z.H., et al., *Microstructure characteristic, mechanical properties and sintering mechanism of nanocrystalline copper obtained by SPS process.* Materials Science and Engineering: A, 2009. **523**(1-2): p. 134-138.

38. Zhang, Z.H., et al., *Microstructural characteristics of large-scale ultrafine-grained copper.* Materials Characterization, 2008. **59**(3): p. 329-333.

39. Zhang, Z.-H., et al., *Ultrafine-grained copper prepared by spark plasma sintering process.* Materials Science and Engineering: A, 2008. **476**(1-2): p. 201-205.

40. Zhaohui, Z., et al., *Sintering mechanism of large-scale ultrafine-grained copper prepared by SPS method.* Materials Letters, 2008. **62**(24): p. 3987-3990.

41. *Sintering of Nickel and Nickel Alloys*, in *ASM Handbook*, ASM International. p. 501-504.

42. Ashby, M.F., *A First Report on Sintering Diagrams.* Acta Metallurgica, 1974. **22**(3): p. 275-289.

43. Bhattacharjee, P.P., S.K. Sinha, and A. Upadhyaya, *Effect of sintering temperature on grain boundary character distribution in pure nickel.* Scripta Materialia, 2007. **56**: p. 13-16.

44. Blakely, J.M. and H. Mykura, *Surface Self Diffusion Measurements on Nickel by the Mass Transfer Method.* Acta Metallurgica, 1961. **9**(1): p. 23-31.

45. Chang, H. and I. Baker, *Isothermal annealing of cold-rolled high-purity nickel.* Materials Science and Engineering: A, 2008. **476**(1-2): p. 46-59.

46. Fullman, R.L. and J.C. Fisher, *Formation of Annealing Twins During Grain Growth.* Journal of Applied Physics, 1951. **22**(11): p. 1350-1355.

47. Furley, J. and V. Randle, *Mesotexture in Annealed Nickel.* Materials Science and Technology, 1991. **7**(1): p. 12-19.

48. Hirano, K., et al., *Diffusion in Cobalt-Nickel Alloys.* Journal of Applied Physics, 1962. **33**(10): p. 3049-3054.

49. Horton, D., C.B. Thomson, and V. Randle, *Aspects of twinning and grain growth in high purity and commercially pure nickel.* Materials Science and Engineering A, 1995. **203**(1-2): p. 408-414.

50. Iordache, M.C., et al., *Grain Growth Kinetics in Nanostructured Nickel.* NanoStructured Materials, 1999. **11**(8): p. 1343-1349.

51. Jernot, J.P., et al., *Sintering Diagrams for Cobalt, Nickel and Iron.* Materials Research Bulletin, 1982. **17**: p. 815-822.

52. Mankins, W.L. and S. Lamb, *Nickel and Nickel Alloys*, in *ASM Handbok*, ASM International. p. 428-445.

53. Randle, V. and D. Horton, *Grain Growth Phenomena in Nickel.* Scripta Metallurgica et Materialia, 1994. **31**(7): p. 891-895.

54. Randle, V., P.R. Rios, and Y. Hu, *Grain growth and twinning in nickel.* Scripta Materialia, 2008. **58**(2): p. 130-133.

55. Swinkels, F.B. and M.F. Ashby, *A Second Report on Sintering Diagrams.* Acta Metallurgica, 1981. **29**: p. 259-281.

56. German, R.M., *Sintering Theory and Practice*. 1 ed. 1996, New York: John Wiley & Sons.

57. German, R.M., *Powder Metallurgy & Particulate Materials Processing*. 1 ed. 2005, Princeton: Metal Powder Industries Federation.

58. Randle, V., *The Role of the Coincident Site Lattice in Grain Boundary Engineering*. 1st ed. 1996, London: The Institute of Materials.

59. Burke, J.E. *A History of the Development of a Science of Sintering*. in *86th Meeting of the American Ceramics Society*. 1984. Pittsburg, PA.

60. Coble, R.L., *Sintering Crystalline Solids. I. Intermediate and Final State Diffusion Models.* Journal of Applied Physics, 1961. **32**(5): p. 787-791.

61. Coble, R.L., *Sintering Crystalline Solids. II. Experimental Test of Diffusion Models in Powder Compacts.* Journal of Applied Physics, 1961. **32**(5): p. 793-799.

62. Herring, C., *Effect of Change of Scale on Sintering Phenomena.* Journal of Applied Physics, 1950. **21**: p. 301-303.

63. Johnson, D.L., *New Method of Obtaining Volume, Grain Boundary, and Surface Diffusion Coefficients from Sintering Data.* Journal of Applied Physics, 1969. **40**(1): p. 192-200.

64. Kingery, W.D. and M. Berg, *Study of the Initial Stages of Sintering Solids by Viscous Flow, Evaporation-Condensation, and Self-Diffusion.* Journal of Applied Physics, 1955. **26**(10): p. 1205-1212.

65. Kuczynski, G.C., *Self-Diffusion in Sintering of Metallic Particles.* Transactions of the American Institute of Mining and Metallurgical Engineers, 1948. **185**: p. 169-178.

66. Kuczynski, G.C., *Measurement of Self-Diffusion of Silver Without Radioactive Tracers.* Journal of Applied Physics, 1950. **21**: p. 632-635.

67. Rahaman, M.N., *Ceramic Processing and Sintering*. 1995, New York: Marcel Dekker, Inc.

68. Omori, M., *Sintering, consolidation, reaction and crystal growth by the spark plasma system (SPS).* Materials Science and Engineering A, 2000. **287**(2): p. 183-188.

69. Cremer, G.D., *Powder Metallurgy*, U.S.P. Office, Editor. 1944, Hardy Metallurgical Company: United States of America.

70. Taylor, G.F., *Apparatus for Making Hard Metal Compactions*, U.S.P. Office, Editor. 1933, General Electric: United States of America.

71. Taylor, G.F., *Welding Process*, U.S.P. Office, Editor. 1933, General Electric Co.: United States of America.

72. Inoue, K., *Method of Electrically Sintering Discrete Bodies*, U.S.P. Office, Editor. 1967: United States of America.

73. Kiyoshi, I. and S. Shinroku, *Electrical Sintering Under Liquid Pressure*, U.S.P. Office, Editor. 1972, Lockheed Martin Corp.: United States of America.

74. Hulbert, D.M., et al., *The absence of plasma in "spark plasma sintering".* Journal of Applied Physics, 2008. **104**(033305): p. 1-7.

75. Lenel, F.V., *Resistance Sintering Under Pressure.* Transactions AIME, 1955. **203**: p. 158-167.

76. Anselmi-Tamburini, U., et al., *Fundamental investigations on the spark plasma sintering/synthesis process II. Modeling of current and temperature distributions.* Materials Science and Engineering A, 2005. **394**: p. 139-148.

77. Carney, C.M. and T.I. Mah, *Current Isolation in Spark Plasma Sintering of Conductive and Nonconductive Ceramics.* J. Am. Ceram. Soc., 2008. **91**(10): p. 3448-3450.

78. Vanmeensel, K., et al., *Modelling of the temperature distribution during field assisted sintering.* Acta Materialia, 2005. **53**: p. 4379-4388.

79. Vanmeensel, K., et al., *The influence of percolation during pulsed electric current sintering of ZrO2-TiN powder compacts with varying TiN content.* Acta Materialia, 2007. **55**(5): p. 1801-1811.

80. Zavaliangos, A., et al., *Temperature evolution during field activated sintering.* Materials Science & Engineering A, 2004. **379**: p. 218-228.

81. Tiwari, D., B. Basu, and K. Biswas, *Simulation of thermal and electric field evolution during spark plasma sintering.* Ceramics International, 2009. **35**: p. 699-708.

82. Dobedoe, R.S., G.D. West, and M.H. Lewis, *Spark plasma sintering of ceramics: understanding temperature distribution enables more realistic comparison with conventional processing.* Advances in Applied Ceramics, 2005. **104**(3): p. 110-116.

83. Kim, H.-t., M. Kawahara, and M. Tokita, *Specimen Temperature and Sinterability of Ni Powder by Spark Plasma Sintering.* Journal of the Japan Society of Powder and Powder Metallurgy, 2000. **47**(8): p. 887-891.

84. Olevsky, E.A. and L. Froyen, *Impact of Thermal Diffusion on Densification During SPS.* J. Am. Ceram. Soc., 2009. **92**(S1): p. S122-S132.

85. Olevsky, E.A., S. Kandukuri, and L. Froyen, *Consolidation enhancement in spark-plasma sintering: Impact of high heating rates.* Journal of Applied Physics, 2007. **102**(11): p. 114913.

86. Anselmi-Tamburini, U., J.E. Garay, and Z.A. Munir, *Fundamental investigations on the spark plasma sintering/synthesis process III. Current effect on reactivity.* Materials Science and Engineering A, 2005. **407**: p. 24-30.

87. Chen, W., et al., *Fundamental investigations on the spark plasma sintering/synthesis process I. Effect of dc pulsing on reactivity.* Materials Science and Engineering A, 2005. **394**: p. 132-138.

88. Olevsky, E. and L. Froyen, *Constitutive modeling of spark-plasma sintering of conductive materials.* Scripta Materialia, 2006. **55**(12): p. 1175-1178.

89. Frost, H.J. and M.F. Ashby, *Deformation-Mechanism Maps: The Plasticity and Creep of Metals and Ceramics*. 1982: Pergamon Press.

90. Shewmon, P., *Diffusion in Solids*. 2nd ed. 1989, Warrendale, PA: The Minerals, Metals & Materials Society. 246.

91. Davies, T.J. and S.T.S. Al-Hassani, *Preforming of metal powder components by direct electrical discharge*, in *Inter-American Conference on Materials Technology*. 1980: San Francisco, CA.

92. Kim, D.K., H.-R. Pak, and K. Okazaki, *Electrodischarge compaction of nickel powders.* Materials Science and Engineering: A, 1988. **104**: p. 191-200.

93. Kim, Y., *Consolidation behavior and hardness of P/M molybdenum.* Powder Technology, 2008. **186**: p. 213-217.

94. Srivatsan, T.S., et al., *The microstructure and hardness of molybdenum powders consolidated by plasma pressure compaction.* Powder Technology, 2001. **114**(1-3): p. 136-144.

95. Arsentyeva, I.P., et al., *The Influence of the Dimension Factor on the Consolidation Process of Highly Disperse Nickel Powders.* Science of Sintering, 1997. **29**(1): p. 3-15.

96. Panigrahi, B.B., *Sintering and grain growth kinetics of ball milled nanocrystalline nickel powder.* Materials Science and Engineering: A, 2007. **460-461**: p. 7-13.

97. Bowman, K., *Mechanical Behavior of Materials*. Vol. 1. 2004, Hoboken: John Wiley & Sons.

98. Mistler, R.E., *Comments on the Paper "Grain Growth during Sintering of Tungsten.* Journal of Applied Physics, 1968. **39**: p. 4875-4876.

99. Randle, V., *The coincidence site lattice and the `sigma enigma'.* Materials Characterization, 2001. **47**(5): p. 411-416.

100. King, A.H. and S. Shekar, *What does it mean to be special? The significance and application of the Brandon criterion.* Journal of Materials Science, 2006.

101. Hull, D. and D.J. Bacon, *Introduction to Dislocations*. 4 ed. 2001, Burlington: Elsevier.

102. TSL, *Orientation Imaging Microscopy Analysis*. 2009, EDAX: Mahwah, NJ.

103. Gibson, L.J. and M.F. Ashby, *Cellular Solids: Structure and Properties*. 1st ed. 1988, Elmsford: Pergamon Press Inc.

104. Cariou, S., F.-J. Ulm, and L. Dormieux, *Hardness-packing density scaling relations for cohesive-frictional porous materials.* Journal of the Mechanics and Physics of Solids, 2008. **56**(3): p. 924-952.

105. Rebholz, C., et al., *Correlation of elastic modulus, hardness and density for sputtered TiAlBN thin films.* Thin Solid Films, 2006. **514**(1-2): p. 81-86.

106. Wang, H.L., C.H. Lin, and M.H. Hon, *The dependence of hardness on the density of amorphous alumina thin films by PECVD.* Thin Solid Films, 1997. **310**(1-2): p. 260-264.

107. Kothari, N.C., *Grain Growth during Sintering of Tungsten.* Journal of Applied Physics, 1967. **38**: p. 2395-2396.

108. Vandermeer, R.A. and H. Hu, *On the Grain Growth Exponent of Pure Iron.* Acta Metallurgica Materialia, 1994. **42**(9): p. 3071-3075.

109. Kwon, O.H. and G.L. Messing, *Kinetic Analysis of Solution-Precipitation During Liquid-Phase Sintering of Alumina.* Journal of the American Ceramics Society, 1990. **73**(2): p. 275-281.

110. Parvatheeswara Rao, B., P.S.V. Subba Rao, and K.H. Rao, *Densification, Grain Growth and Microstructure of Ni-Zn Ferrites.* Journal de Physique, 1997. **7**: p. 241-242.

111. Shao, W.Q., et al., *Apparent activation energy for densification of α-Al2O3 powder at constant heating-rate sintering.* Bulletin of Materials Science, 2008. **31**(6): p. 903-906.

112. Jenkins, W.D. and T.G. Digges, *Effect of Temperature on the Tensile Properties of High-Purity Nickel.* Journal of Research of the National Bureau of Standards, 1952. **48**(4): p. 313-321.

113. Chaim, R., *Densification mechanisms in spark plasma sintering of nanocrystalline ceramics.* Materials Science and Engineering: A, 2007. **443**(1-2): p. 25-32.

114. Chaim, R. and M. Margulis, *Densification maps for spark plasma sintering of nanocrystalline MgO ceramics.* Materials Science and Engineering: A, 2005. **407**(1-2): p. 180-187.

APPENDIX

Table A1. Density, hardness, and porosity results for CS processed nickel.

Temp	Dwell	Density		Hardness		Porosity (%)	
(°C)	(h)	% Theoret.	s.d.	(Hv)	s.d.	Center	Edge
900	0	0.789	0.0053	42	4.55	14	21
	1	0.801	0.0027	50	6.06	23	24
	2	0.764	0.0022	41	8.80	25	26
1100	0	0.835	0.0103	54	5.96	20	21
	1	0.848	0.0033	70	4.87	4	8
	2	0.837	0.0074	53	4.20	12	12
1300	0	0.873	0.0381	67	11.39	16	17
	1	0.900	0.0020	78	11.54	11	10
	2	0.888	0.0009	69	9.74	12	12

Table A2. Grain boundary character and grain size results for CS processed nickel.

Temp	Dwell	Grain Boundaries					Grain Size	
(°C)	(h)	Σ1	Σ3	Σ5-29	Special	General	(μm)	s.d
900	0	0.076	0.373	0.084	0.533	0.467	4.48	3.204
	1	0.027	0.354	0.095	0.476	0.524	4.23	2.551
	2	0.025	0.331	0.097	0.453	0.547	4.10	2.596
1100	0	0.032	0.329	0.091	0.452	0.548	4.21	2.665
	1	0.146	0.311	0.064	0.521	0.479	5.22	4.154
	2	0.085	0.374	0.067	0.526	0.474	5.83	4.380
1300	0	0.023	0.391	0.083	0.497	0.503	5.02	3.234
	1	0.023	0.417	0.075	0.515	0.485	6.79	5.032
	2	0.029	0.494	0.066	0.589	0.411	8.72	7.474

Table A3. Density, hardness and porosity results for SPS processed nickel.

Ramp Rate (°C/min)	Pressure (MPa)	Temp (°C)	Dwell (min)	Density % Theoret.	s.d.	Hardness (Hv)	s.d.	Porosity (%) Center	Edge
400	61.9	800	5	0.948	0.0013	109	4.33		
200	61.9	800	5	0.942	0.0010	122	9.32		
100	41.6	500	1	0.730	0.0018	37	1.91	32	36
			2	0.695	0.0018	34	3.17	30	32
			3	0.741	0.0009	39	1.27	30	31
		800	1	0.881	0.0005	78	11.17	12	18
			2	0.888	0.0037	74	2.19	12	19
			3	0.926	0.0024	92	8.99	10	14
	61.9	400	0	0.715	0.0477				
		500	0	0.761	0.0009	43	0.92	30	30
			1	0.794	0.0015	51	3.14	27	28
			2	0.758	0.0011	48	2.32	26	29
			3	0.789	0.0010	51	2.58	22	26
			10	0.818	0.0012	61	3.57	22	24
		600	0	0.789	0.0038				
		700	0	0.839	0.0005				
		800	0	0.919	0.0009	93	3.06	10	13
			1	0.935	0.0010	95	2.79	5	10
			2	0.941	0.0012	95	4.08	7	9
			3	0.950	0.0011	107	3.37	6	10
			5	0.949	0.0006	111	7.07		
			10	0.970	0.0021	108	10.38	4	6
		900	0	0.942	0.0010				
		1000	0	0.968	0.0006				
	79.6	500	1	0.805	0.0019	57	3.28	24	26
			2	0.822	0.0011	60	1.15	19	22
			3	0.833	0.0004	64	3.12	19	22
		800	1	0.951	0.0024	101	1.48	4	8
			2	0.962	0.0003	111	2.67	4	8
			3	0.968	0.0009	106	3.28	4	6
92.9	41.6	650	1	0.822	0.0034	56	1.66	23	25
			2	0.788	0.0018	53	8.26	22	22
			3	0.845	0.0015	59	3.41	18	23
	61.9	650	0	0.838	0.0004	62	1.73	20	22
			1	0.862	0.0008	70	1.69	17	22
			2	0.897	0.0004	83	2.48	12	16
			3	0.901	0.0017	86	3.37	14	18
			10	0.926	0.0021	91	2.11	10	13
	79.6	650	1	0.887	0.0021	82	2.86	12	21
			2	0.900	0.0020	94	2.89	12	12
			3	0.909	0.0045	93	1.95	10	12
50	61.9	800	5	0.949	0.0009	121	7.12		
25	61.9	800	5	0.954	0.0010	115	8.73		
50-50	61.9	800	5	0.956	0.0005	109	3.78		
25-25	61.9	800	5	0.961	0.0010	120	8.80		

Table A4. Grain size results for SPS processed nickel.

Ramp Rate (°C/min)	Pressure (MPa)	Temp (°C)	Dwell (min)	Grain Size (μm) Center	s.d	Edge	s.d.
400	61.9	800	5	4.03	10.888	3.58	8.108
200	61.9	800	5	3.04	2.295	2.84	2.039
100	41.6	500	1				
			2				
			3	1.96	1.509	1.92	1.413
		800	1				
			2				
			3	3.10	2.990	2.86	2.616
	61.9	400	0	1.68	0.916		
		500	0	1.87	1.293		
			1	2.00	1.563	1.90	1.463
			2	1.80	1.237	1.66	1.191
			3	1.79	1.257	1.76	1.348
			10	2.04	1.477	2.03	1.502
		600	0	2.04	1.653		
		700	0	2.32	1.996		
		800	0	2.94	2.195		
			1	3.06	2.462	2.92	2.324
			2	2.60	2.612	2.14	2.089
			3	3.04	3.516	2.89	2.779
			5	3.07	2.248	3.18	2.454
			10	4.46	4.155	3.32	2.749
		900	0	3.12	2.616		
		1000	0	4.83	4.453		
	79.6	500	1				
			2				
			3	2.08	1.537	2.03	1.525
		800	1				
			2				
			3	4.24	3.673	3.50	2.797
92.9	41.6	650	1				
			2				
			3	2.41	2.047	2.25	1.936
	61.9	650	0	2.45	1.708		
			1	2.47	1.988	2.37	1.870
			2	2.44	2.040	1.98	1.844
			3	2.53	2.152	2.53	2.160
			10	2.77	2.027	2.52	1.959
	79.6	650	1				
			2				
			3	2.58	1.965	2.54	1.971
50	61.9	800	5	3.14	2.408	2.93	2.089
25	61.9	800	5	3.34	2.507	3.07	2.316
50-50	61.9	800	5	3.25	2.628	2.97	2.212
25-25	61.9	800	5	3.28	2.590	2.95	2.418

Table A5. Grain boundary character results for SPS processed nickel.

Ramp Rate	Pressure	Temp	Dwell	Grain Boundaries				
(°C/min)	(MPa)	(°C)	(min)	Σ1	Σ3	Σ5-29	Special	General
400	61.9	800	5	0.035	0.393	0.081	0.509	0.491
200	61.9	800	5	0.02	0.378	0.085	0.483	0.517
100	41.6	500	1					
			2					
			3	0.054	0.314	0.131	0.499	0.501
		800	1					
			2					
			3	0.059	0.397	0.11	0.566	0.434
	61.9	400	0	0.038	0.345	0.159	0.542	0.458
		500	0	0.032	0.297	0.123	0.452	0.548
			1	0.038	0.334	0.116	0.488	0.512
			2	0.065	0.347	0.123	0.535	0.465
			3	0.033	0.328	0.107	0.468	0.532
			10	0.034	0.302	0.096	0.432	0.568
		600	0	0.047	0.348	0.126	0.521	0.479
		700	0	0.118	0.277	0.07	0.465	0.535
		800	0	0.033	0.36	0.079	0.472	0.528
			1	0.053	0.367	0.072	0.492	0.508
			2	0.035	0.330	0.129	0.494	0.506
			3	0.075	0.331	0.099	0.505	0.495
			5	0.025	0.363	0.083	0.471	0.529
			10	0.061	0.444	0.068	0.573	0.427
		900	0	0.083	0.353	0.073	0.509	0.491
		1000	0	0.035	0.494	0.068	0.597	0.403
	79.6	500	1					
			2					
			3	0.036	0.297	0.09	0.423	0.577
		800	1					
			2					
			3	0.021	0.437	0.076	0.534	0.466
92.9	41.6	650	1					
			2					
			3	0.077	0.346	0.109	0.532	0.468
	61.9	650	0	0.030	0.356	0.096	0.482	0.518
			1	0.066	0.319	0.086	0.471	0.529
			2	0.060	0.340	0.093	0.493	0.507
			3	0.046	0.348	0.095	0.489	0.511
			10	0.041	0.354	0.089	0.484	0.516
	79.6	650	1					
			2					
			3	0.022	0.374	0.082	0.478	0.522
50	61.9	800	5	0.021	0.344	0.092	0.457	0.543
25	61.9	800	5	0.029	0.363	0.079	0.471	0.529
50-50	61.9	800	5	0.022	0.375	0.084	0.481	0.519
25-25	61.9	800	5	0.022	0.379	0.082	0.483	0.517